MESOMETEOROLOGICAL MODELLING AND TRAJECTORY STUDIES DURING AN AIR POLLUTION EPISODE IN THE LOWER FRASER VALLEY, BRITISH COLUMBIA, CANADA

By

Yuelong Miao

B. Sc. (Atmospheric Physics) Nanjing University, P.R. China, 1984

A THESIS SUBMITTED IN PARTIAL FULFILLMENT OF

THE REQUIREMENTS FOR THE DEGREE OF

MASTER OF SCIENCE

in

THE FACULTY OF GRADUATE STUDIES

ATMOSPHERIC SCIENCE PROGRAMME, DEPARTMENT OF GEOGRAPHY

We accept this thesis as conforming

to the required standard

THE UNIVERSITY OF BRITISH COLUMBIA

August 1993

In presenting this thesis in partial fulfilment of the requirements for an advanced degree at the University of British Columbia, I agree that the Library shall make it freely available for reference and study. I further agree that permission for extensive copying of this thesis for scholarly purposes may be granted by the head of my department or by his or her representatives. It is understood that copying or publication of this thesis for financial gain shall not be allowed without my written permission.

(Signature) _____

Department of GEOGRAPHY

The University of British Columbia
Vancouver, Canada

Date August 6, 1993

Abstract

The Lower Fraser Valley, straddling the USA-Canada border in western North America, often experiences episodes of elevated tropospheric ozone in summertime. The meteorology governing those episode days is characterized by a stagnant high pressure system, light wind, strong insolation and the occurrence of sea breezes.

To shed some light on the mesometeorology of ozone episodes in the LFV, this study employed the Regional Atmospheric Modelling System from Colorado State University, a nonhydrostatic, three-dimensional mesoscale modelling system to simulate the detailed structure of air flows over the valley for one specific episode day. Significant code modifications have been made to enhance the model's ability to represent surface energy fluxes and predict surface temperatures in the surface of complex terrain and land-use patterns. Evaluation of the model performance was made against an extensive set of observations on the episode day. Pollutant transport on the modelling day was explored with a Lagrangian particle dispersion model. Specifically, forward trajectories were calculated for particles released at various locations in the Lower Fraser Valley and at different times.

A systematic qualitative and quantitative model evaluation with the statistical method of Willmott showed that the model could adequately simulate the observed sea breeze and other interactive terrain-induced flows such as slope wind and channel flow. Trajectory studies indicated that pollutant recirculations occurred largely from sources originating in the northwest part of the valley where most emission sources are located, and ended in a region where the highest ozone concentrations were observed. Recirculations were due to pollutants traveling with the interactive flows of sea breeze and upslope winds,

and later being captured and directed back to the valley by the downslope winds. Particles released in other part of the valley all travelled outside the valley, having a minimal contribution to the episode buildup.

Table of Contents

List of Tables

List of Figures

Acknowledgements

My deepest gratitude goes to my supervisor, Prof. Douw Steyn, for the most valuable study opportunity he provided me, and for his consistent support in both academic and financial affairs. His timely advice, criticism and encouragement have been the important forces to push me one step further. His friendly enthusiasm and open-minded attitude have influenced me greatly. Thanks also to the other members of my committee, Profs. Tim Oke and Ian McKendry, for their constructive comments and guidance in the course of the thesis research. My modelling work is much improved, thanks in no small measure to Prof. Oke's suggestion of a updated energy balance scheme.

I am very grateful to my senior colleagues Drs. Peter Jackson and Xiaoming Cai for their help with the RAMS model. I could not have operated such a comprehensive model system without their assistance. I would also like to thank Dr. Mike Moran in Atmospheric Environment Service of Canada for his generous supply of the RAMS compatible particle model and for his hands-on help with its operation. Dr. Sue Grimmond at University of Indiana, USA and Dr. Jingming Chen at Remote Sensing Center, Canada were indispensible for their help in constructing the energy balance scheme.

My colleague Ms. Natalie Suzuki, carefully read through the entire thesis draft and made important suggestions. I will remember many other students at the Department of Geography for their warmness and friendship.

This thesis is dedicated to my beloved family in China, my wife Shuzhen Xu and my daughter Ling Miao who will be three years old by July 25. My deepest feeling to them and my gratitude to their understanding are beyond description.

Chapter 1

Introduction

1.1 Introduction

The Lower Fraser Valley (LFV) region along the British Columbia-Washington coast, extends from the Strait of Georgia in the west to the Fraser canyon in the east. The valley is bounded by the Coast Mountains to the north and the Cascade Range to the southeast (Fig. 1.1). The most densely populated and industrialized area of the LFV lies in the Greater Vancouver area with a population of approximately 1.5 million. While Vancouver enjoys a world-wide reputation as a beautiful harbour city, it is not without an air pollution problem. Data obtained from the Greater Vancouver Regional District (GVRD) air quality monitoring network have revealed some startling facts. The Maximum Acceptable hourly average ozone [1] concentration (82 ppb) was exceeded an average of 160 times a year during the 1980s. Over the same period, the Maximum Tolerable hourly ozone concentration (153 ppb) was exceeded an average of four times per year. Ozone episodes are particularly frequent in summer when the synoptic weather pattern is stagnant and insolation is strong. As an extreme example, from August 1 to September 30, 1988, four ozone episodes were observed. On 27 consecutive days, high ozone values were reported with a maximum ozone concentration of over 200 ppb occurring on Sept. 3, 1988. Clearly Vancouver and the surrounding LFV are subject to ozone episodes. This is somewhat surprising since Vancouver is considerably less industrialized and has

[1] Unless otherwise noted, the word "ozone" will be used herein to refer strictly to the ozone in the troposphere as opposed to ozone in the ozone layer of the stratosphere. Excessive ozone in the lower atmosphere can harm human and plant health and many building materials.

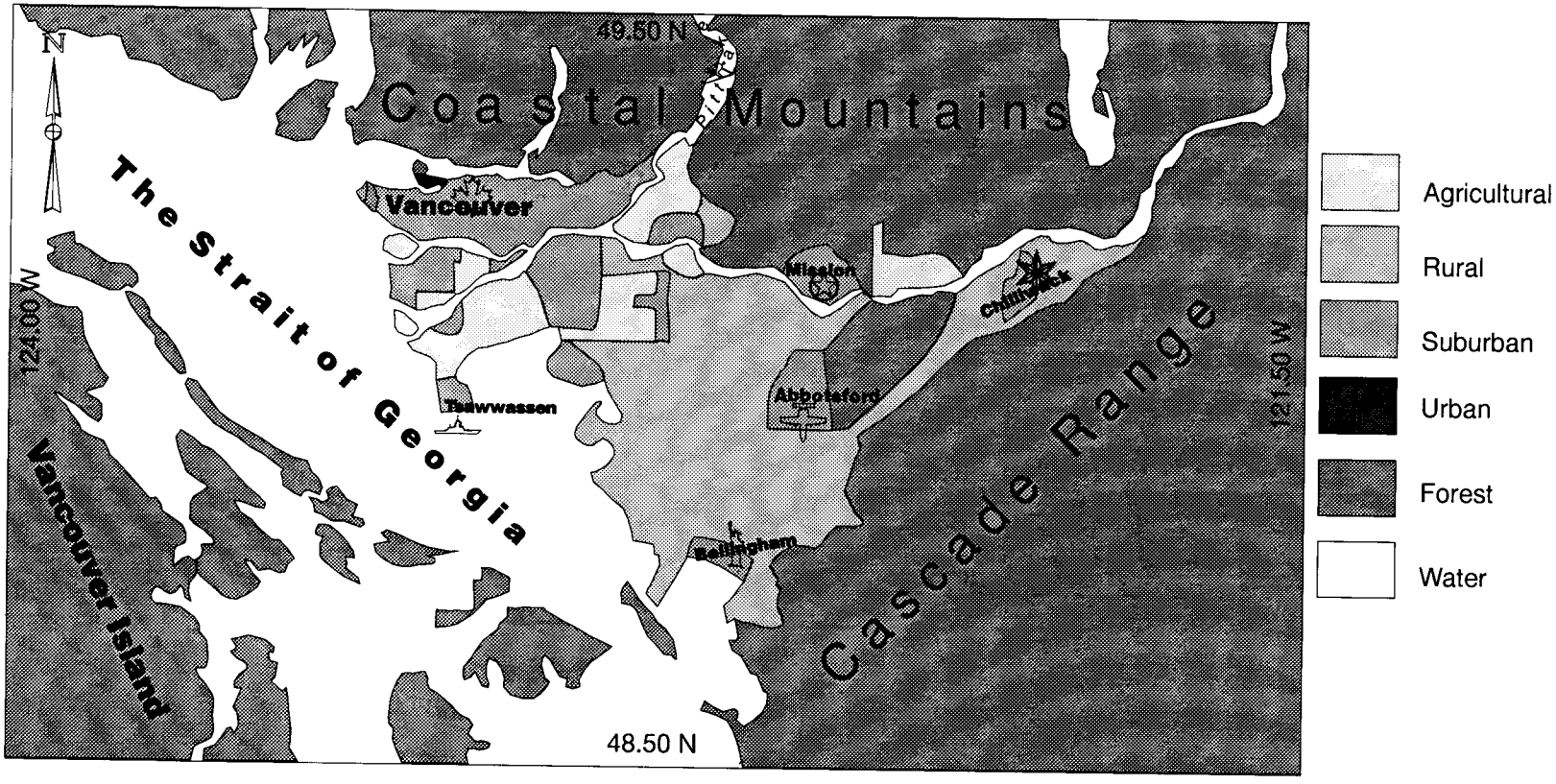

Figure 1.1: Location and Land-use maps of the Lower Fraser Valley and the surrounding area. Inner labels are the corresponding latitude or longitude values for the boundaries. Symbols beside location names are for future use of identification.

a significantly smaller population than other large mid-latitude coastal cities, such as Los Angeles, Athens and Tokyo, which are known to experience ozone episodes. It is generally recognized that it is the particular combination of emissions, topography and meteorology in the LFV that exacerbates the air pollution problem (Steyn et al., 1992; Concord, 1982; Concord, 1985).

The major source of ozone precursors is motor vehicles which contribute over two-thirds of the total (Steyn et al., 1992), and most of these emissions occur in the densely populated western portions of the LFV. These emissions, when exposed to strong solar radiation, will produce ozone through a series of photochemical reactions (Güsten, 1986). When these conditions coincide with meteorological conditions which restrict ventilation, ozone will accumulate. Such conditions usually occur in summer. The stagnant and weak Pacific high-pressure system, characterized by low wind speeds, clear skies and subsidence inversions, caps the valley while the valley walls act as barriers to further block ventilation in the valley. Thermally-induced winds exacerbate the poor ventilation problem through pollutant recirculation. Figure 1.2 schematically depicts such a closed atmospheric circulation system under the influence of a stagnant high-pressure system. This pattern has been suggested by meteorologists since the early 1970's (Hay and Oke, 1976), but the detailed meteorological influence on the pollutant transport has yet to be explored.

To help understand the air pollution problem in the LFV, it is necessary to introduce some concepts of air pollution, particularly regarding the impact of meteorology in a coastal area such as Vancouver.

1.1.1 Air Pollution and Mesoscale Meteorology

Air pollution spans a wide range of scales from local scales as exemplified by stack plumes to continental and global scales as exemplified by the multi-country radionuclide

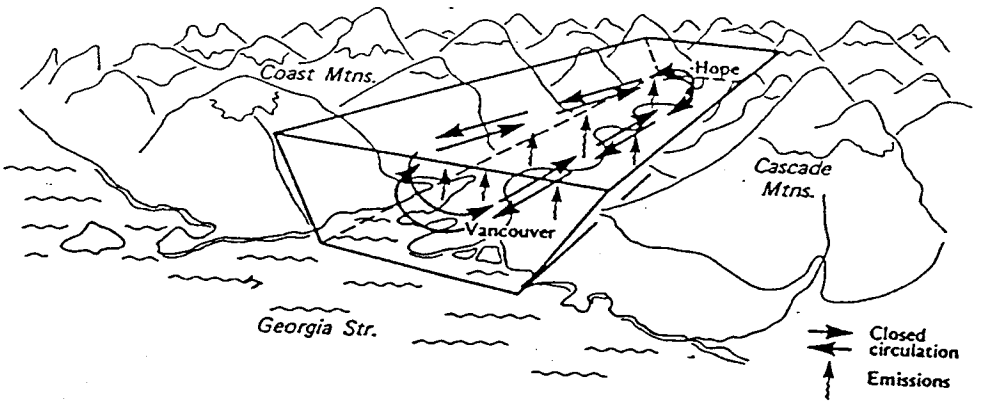

Figure 1.2: The essentially closed atmospheric circulation system characteristic of Vancouver while under the influence of a stagnant high-pressure system. Taken from Hay and Oke (1976).

contamination experienced during the 1986 Chernobyl disaster in the former Soviet Union (Persson, Rodhe and Geer, 1987; Smith and Clark, 1988; Stern et al., 1984; Wheeler, 1988). Air pollution dispersion can be very different from one scale to another. At local scales, turbulent diffusion and advection dominate the dispersion of pollutants. Dispersion is limited to the lower atmosphere, and affects a fairly small radius in the vicinity of the pollutant source. At the continental and global scales, long-range transport plays a major role in the movement of pollutants. Pollutants are often transported through the stratosphere and affect regions well beyond the source areas. The regional or mesoscale is of particular interest in the present study. This scale shares some of the characteristics of both small and large scale problems in that turbulent diffusion and atmospheric transport are important. While emission sources are typically local, the dispersal of the pollutants is driven by regional meteorology.

Coastal Mesoscale Meteorology

a)

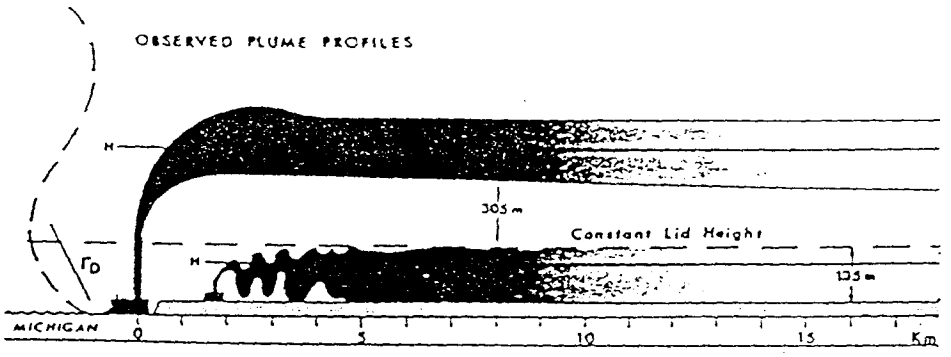

b)

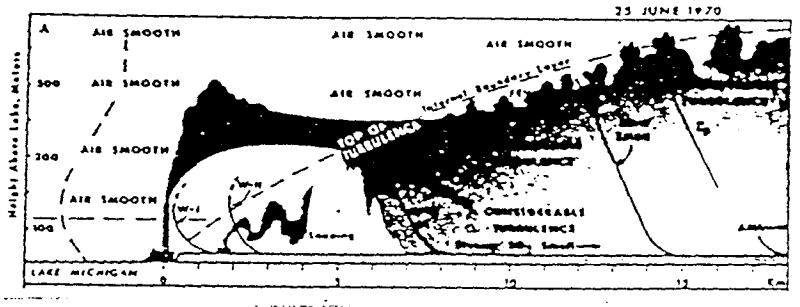

c)

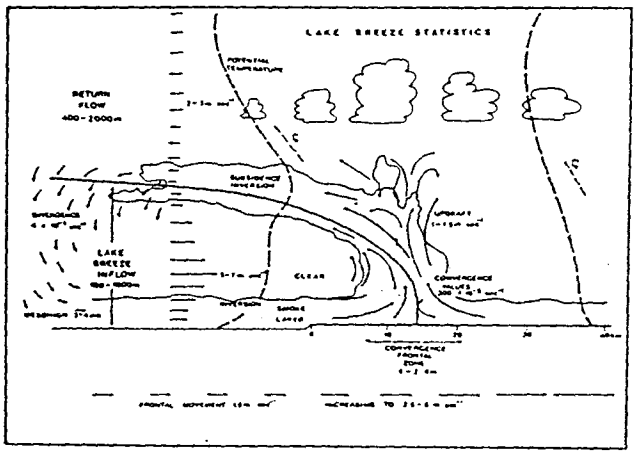

d)

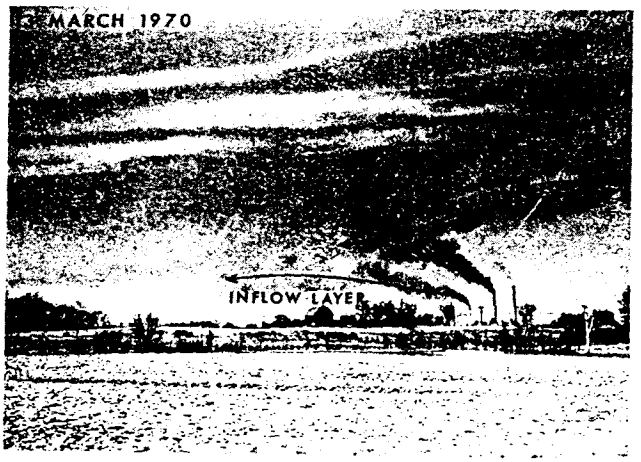

Figure 1.3: Examples of coastal meteorology and resultant air pollution. a) plume trapping. b) fumigation. c) sea breeze. d) plume behaviour within the sea breeze regime. Taken from Lyons (1975).

Mesoscale air pollution problems are experienced in many places. Since most major population and industrial centres are located along rivers, oceans and lakes, emphasis is given to coastal meteorology and its impact on air pollution. Typified by differential heating between land and water, coastal areas form a distinct environment in diffusing and transporting pollutants. On a cloudy day or at night, neutral to stable air moving across warmer near-shore water before landfall will result in a shallow mixed layer near the surface. This shallow layer will be enhanced slightly by the mechanical mixing when the air travels inland. A plume emitted from a low stack near the shore will then be trapped in this shallow mixed layer (Fig. 1.3a), a phenomenon known as *plume trapping* (Lyons, 1975). On a sunny day, when air flows onshore, the air mass will be modified by changes in roughness and temperature. A thermal internal boundary layer (TIBL) will form and deepen with distance downwind of the shoreline (Stull, 1989). The intersection of a plume released from an elevated near-shore source with the TIBL will result in *fumigation*(Fig. 1.3b).

The sea/land breeze is a well-known mesoscale phenomenon in the shoreline environment with onshore sea breeze in the daytime and offshore land breeze at night (Atkinson, 1981). This phenomenon is a direct consequence of differential heating over land and sea. The inland sea breeze near the surface is often associated with an offshore return flow aloft(Fig. 1.3c). These two flows often form a circulation called *sea breeze circulation* which has an important influence on pollutant movement (Lyons, 1975). Pollutants injected in the near surface inflow may enter the return flow once being lifted in a convergence zone such as a sea breeze front. If the synoptic pattern is stagnant for several days, pollutants may recirculate in the coastal regions, a condition conducive to air pollution episodes. The varying wind direction in the vertical could also cause plumes at different heights to move in very different directions. Figure 1.3d illustrates such phenomena. All these distinct features in the coastal atmosphere complicate the study of air pollution

near the coast.

The picture is further complicated by the presence of mountains. When mountains are present, mountain/valley winds, upslope/downslope winds and channel flows are often observed (Atkinson, 1981). For mountain-valley situations, stable lapse rates can result in a marked decoupling of the air within the valley from the upper-air flow. This phenomenon results in poor ventilation of the lower levels and constitutes meteorological conditions conducive to the long-term buildup of air pollution levels. A similar situation occurs when an elevated inversion exists near or below ridge levels and contains a flow within a valley region. Such mountainous coastal regions present a complex mesoscale picture with interactions among various terrain-induced mesoscale phenomena and synoptic flow. Air pollution studies in such an area are indeed a big challenge. Extensive meteorological observations, and atmospheric diffusion and transport experiments are necessary to reveal the dynamics of mesoscale meteorology and its impact on pollutant transport. Unfortunately field experiments are costly. Mesoscale modelling, on the other hand, provides a convenient and economic tool to simulate and forecast the wind flow in a region. In fact, a complete picture of wind fields can only be achieved with a prognostic mesoscale model.

Mesoscale and Air Pollution Modelling in Coastal Regions

A number of modelling studies have been carried out on such urbanized mountainous coastal areas as Los Angeles, Tokyo and Athens (Chang et al., 1990; Chang et al., 1989; Chang et al., 1990; Moore et al., 1991; Moussiopoulos, 1993; Ulrickson and Mass, 1990a; Ulrickson and Mass, 1990b). A common purpose of these studies was to understand how the regions' various mesoscale phenomena interact with each other and with large-scale weather patterns, and how the specific local meteorological conditions determine the transport of pollutants in and around the studied area.

Ulrickson and Mass(1990a, 1990b) employed the hydrostatic Colorado State University Mesoscale Model (CSUMM) to simulate three-dimensional airflows in the Los Angeles basin. Having documented the model's accuracy in simulations of diurnal mesoscale features in the basin, they then looked at synoptic influences on mesoscale circulations during episode days. They concluded that light large-scale winds had little influence on strong summertime mesoscale circulations such as sea/land breeze and mountain/valley wind circulations, whereas stronger large-scale winds exerted considerable influence on the weak mesoscale wintertime circulations. They further investigated the interactions between various mesoscale phenomena and the influence of these phenomena on pollutant transport using a forward parcel trajectory method. One of their findings is that daytime upslope flows near mountains ventilate the basin, inducing basinwide airflow and augmenting the sea breeze. However, based on their simulations, the mechanism for the development of air pollution episodes was not clear.

Moussiopoulos (1993) reviewed air pollution studies over the past decade in the Greater Athens Area (GAA), a region surrounded on three sides by mountains and on the fourth side by the sea. Observations have shown that most of the air pollution episodes are associated with the development of a sea breeze (Lalas et al., 1983) which tends to stratify the atmosphere above Athens, thus trapping air pollutants at a relatively low height above ground. Offshore pollutant transport by the land breeze and its readvection into the basin by the sea breeze result in the further buildup of pollutants. A nonhydrostatic mesoscale model - MEMO was used to simulate the wind fields in Athens (Moussiopoulos et al., 1993) on episode days when a sea breeze was observed. Using this model output, they went on to simulate the dispersion and chemical transformation of air pollutants in the GAA with a fully vectorized photochemical dispersion model - Model for the Atmospheric Dispersion of Reactive Species (Moussiopoulos, 1989; Moussiopoulos and Oehler, 1988). Predicted O_3, CO, NO and NO_2 values compared favourably with

available observations.

The long-range transport (LRT) of oxidant pollutants in central Japan is believed to play an important role in regional air pollution (Chang et al., 1990; Chang et al., 1990; Kurita et al., 1985). Although the Tokyo metropolitan complex contains most of the emission sources in the region, observed maximum ozone concentrations are much higher in a mountainous region 150 km away than they are in Tokyo (Kurita et al., 1985). With the aid of an intensive meteorological and photochemical field study carried out in central Japan in 1983, Chang et al. (1989) explored the long-range transport mechanism through a trajectory method and found that the combined roles of land/sea breeze, mountain/valley winds, steady onshore winds, strong thermal low and subsidence inversions under a synoptic high pressure system contributed to the LRT mechanism. An advanced Eulerian combined transport/chemistry/removal model: The Sulfate Transport Eulerian Model-II was then used to analyze LRT and the associated chemical processes. Predictions coincided well with the observations and showed clearly that sources located more than 100 km from the region could have a profound impact on local air quality.

1.2 Objectives

1.2.1 Previous Air Pollution Studies in the LFV

A number of studies on air pollution in the LFV have been carried out (Robeson and Steyn, 1990; Steyn and Faulkner, 1986; Steyn and McKendry, 1987; Steyn and McKendry, 1988; Steyn and Oke, 1982; Steyn, Roberge and Jackson, 1990). A continuous monitoring network for meteorological and pollutant data has been in operation for more than a decade. Since terrain-induced mesoscale phenomena like sea/land breeze, mountain/valley wind and valley channel flows are often associated with air pollution episodes, a major effort has been given to the study of the LFV's specific local meteorology and

its impact on air pollution.

Mixed layer depth is known as an important surrogate for pollutant diffusion or mixing. An attempt was made by Steyn and Oke (1982) to simulate the mixed layer depth in the LFV using an Eulerian mixed layer depth model. The model predicted temporal variations of the mixed layer depth agreed well with the observations, and revealed that the mixed layer depth in the LFV rarely exceeds 800 m due to the onshore advection of cool marine air. As an adjunct study to the observational and modelling studies of the physical nature of the sea breeze, Steyn and Faulkner (1986) studied the climatology of sea breezes in the LFV through examination of ten years of hourly wind data from two stations in the LFV, one near the coast and the other in the valley. The study revealed that the sea breeze is a phenomenon frequently observed in the LFV. It also showed strong interactions between the sea breeze and slope winds near the shoreline, and between sea breeze and valley winds further inland.

As part of the efforts in providing a scientific basis for the GVRD's air pollution control and abatement strategies, Robeson and Steyn (1990) presented three statistical models to forecast daily maximum ozone concentrations in the LFV. They concluded that the TEMPER regression model, based on daily maximum air temperature and the previous day's ozone concentration, provided the most accurate forecast.

Steyn, Roberge and Jackson (1990) analysed the LFV's meteorology surrounding a persistent ozone episode occurring between September 1-3, 1988. They confirmed the typical meteorological characteristics of episodes in the LFV: high temperatures, low wind speeds, shallow mixed layer depth, slack synoptic pressure gradients, strong subsidence and the occurence of the sea breeze phenomena.

Taylor (1991) also looked at the meteorology especially the synoptic conditions surrounding air pollution episodes in the LFV. Based on the recent work of Atmospheric Environment Service Pacific Region on the relationship between synoptic patterns and

high ozone events in the LFV, Taylor concluded that synoptic conditions of a strong upper ridge over the eastern Pacific and British Columbia coupled with a surface thermal trough along the Washington-southern B.C. coast are necessary for elevated ozone concentrations in the LFV. He further pointed out that the lowered sea level pressure on the coast produced by these thermal troughs may also interfere with and restrict the development of mesoscale sea breeze. An ozone forcast method based on the crucial connection between specific synoptic patterns and high ozone events was carried out and showed some success in predicting ozone. He also used a statistical ozone forecast model, which links maximum daily ozone to temperature, yesterday's ozone, precipitation and mean sea level pressure differences between the coast and the interior, to forecast the ozone concentrations. He argued that this may be a more promising tool to the ozone forecast.

McKendry and Li-Ting-Wai (1993) investigated further of the relationship between high ozone events in the LFV and synoptic meteorological conditions with extensive set of ozone concentration data at Port Moody and synoptic charts at both 500 hPa and mean sea level for the period of 1978-92. Their studies confirmed what Taylor (1991) discovered about the specific synoptic meteorological conditions on the days of high ozone, i.e., a low level thermal trough and upper level ridge of high pressure. The inter-annual variability of ozone episode days was also studied in their report.

A realistic model to simulate the windfields in the LFV is an essential prerequisite to the understanding of the etiology of severe ozone episodes during summertime and to the knowledge of the horizontal spatial structure of the pollutant concentrations in this region. Intensive mesoscale modelling has been carried out to identify the local meteorology in the LFV during episodes. Steyn and McKendry (1987) employed the hydrostatic CSUMM model to simulate windfields in the LFV for episode days in 1985 and 1986. Quantitative and qualitative comparisons of the model output with observed

data were also conducted for one episode day (Steyn and McKendry, 1988). Results showed that in general the model performed well in simulating both the spatial and temporal variability of the thermally-forced flows within the chosen domain. The model performed less well at night and had a tendency to overpredict wind speeds in the daytime. Unfortunately their modelling studies were limited to the simulation of the meteorological fields and did not try to investigate the relationship between the mesoscale meteorology and pollutant transport.

1.2.2 Objectives

Given that extensive modelling studies have been carried out on the local meteorology, but have not considered in detail the interaction of the meteorology with air pollutant transport, the present study will expand on these previous modelling efforts and will attempt to elucidate the relationship between the mesoscale meteorology and air pollutant transport in the LFV. The major objectives of this study are the following:

- Simulate the three-dimensional windfields over the LFV for a 24-hour period during a specific summer ozone episode day using the Regional Atmospheric Modelling System(RAMS).

  The simulation will be performed with the RAMS model from Colorado State University. This is an advanced version of the CSUMM model, and should provide more realistic windfields given its non-hydrostatic formulation and more realistic treatment of physical processes. Furthermore, improved model performance should be achieved by using the following considerations:

  1. Use 2.5km x 2.5km resolution in the horizontal so as to resolve more terrain features. Steyn and McKendry (1987) used a horizontal resolution of 5km x 5km in their model runs.

2. Select the model domain to cover the Georgia Strait and part of Vancouver Island to the west and the American part of the LFV to the south in order to include all the mesoscale phenomena in the LFV that might influence the pollutant movement within the region.
3. Preserve the surface inhomogeneity in the model.
4. Develop a prognostic surface temperature scheme using a semi-empirical surface energy balance representation to replace a pure soil model. The RAMS soil models are not adequate to deal with the various landcovers of the LFV.

The study day of August 23, 1985 is chosen for the following reasons.

1. Reliable tethersonde data from Queen Elizabeth Park in Vancouver were available and showed the day exhibited classical sea breeze features, i.e., development of a shallow layer of onshore flow overlain by offshore winds during the day. Also available on this day were surface wind and temperature observations obtained from an expanded wind monitoring network set up to study thermally-forced mesoscale flows in the LFV during the summer of 1985 (Steyn and McKendry, 1988).
2. That day was characterised by clear skies, light winds and an upper ridge aloft associated with a surface thermal trough, a synoptic meteorological pattern typical for the ozone episode buildup in the LFV as discovered by Taylor (1991) and McKendry and Li-Ting-Wai (1993).
3. It was a significant atmospheric oxidant episode day. Three out of nine ozone monitoring stations recorded ozone concentrations in excess of 82 ppb on the study day and the following day. Contours depicting maximum ozone concentrations for 23 August 1985, as shown in Fig. 1.4, indicate the severity of the

episode.

An additional reason for selecting this day is that it is the same day as studied intensively by Steyn and McKendry (1987), Steyn and McKendry (1988). Therefore model output can be compared against theirs even though this is not a major objective of this study.

- Verify the model performance with an extensive set of wind and temperature observations covering the selected 24-hour period.

  It is critical that the model's ability to produce a realistic meteorological field be demonstrated before any further studies based on the model output can be made with confidence. In addition to the general qualitative evaluations, Willmott's (1985) systematic statistical model evaluation methods will be used to conduct the model evaluation.

- Investigate pollutant transport in the LFV.

  A Lagrangian Particle Dispersion Model (Moran, 1992) will be employed for this purpose. Specifically, forward trajectories will be calculated to explore the hypothesized possibilities of heated upslope flow ventilation and pollutant recirculations through sea breeze regimes. It is hoped that this study will shed light on the etiology of the air pollution episode occurring on the selected day.

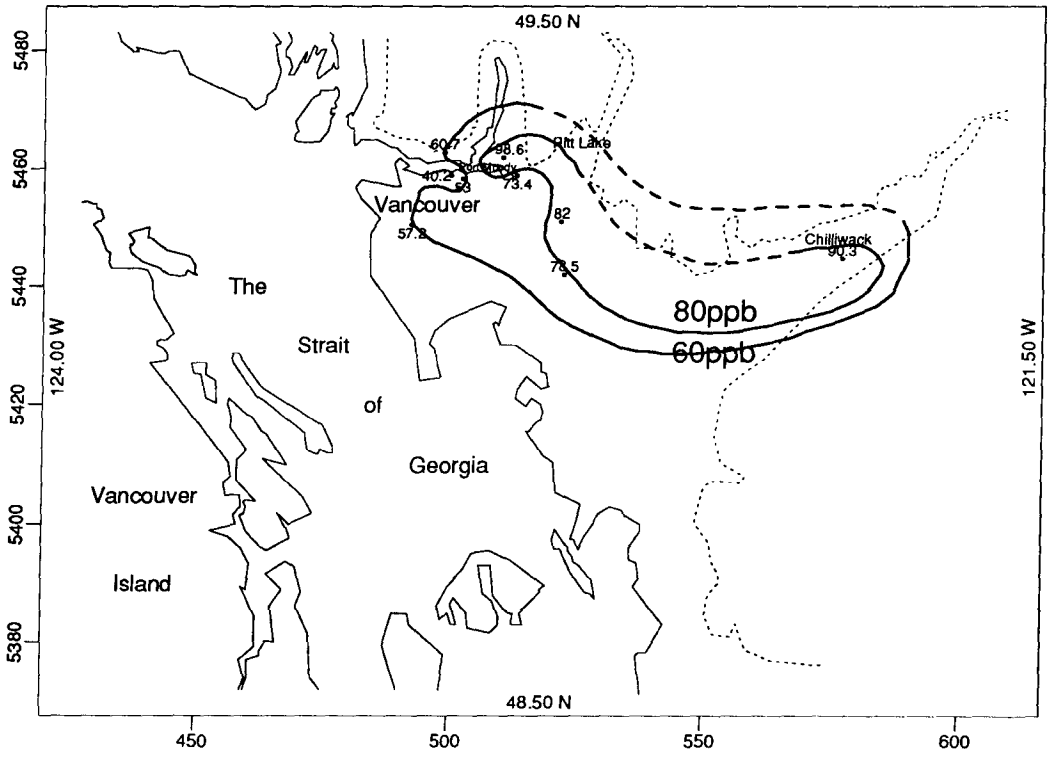

Figure 1.4: Maximum ozone concentration isopleths on August 23, 1985 in the LFV. Thick solid line refers to ozone contour, and thick dashed line refers to uncertain ozone contour. Thinner soild line is the coastline, and thinner dashed line is the 100m terrain contour indicating the edge of the valley walls. Values beside dots are the ozone concentrations at respective stations. Inner labels refers to the corresponding latitude or longitude of the boundary. Outer labels are in units of UTM coordinates (x 10^3).

Chapter 2

The RAMS Model and Its Application

2.1 Introduction

In a study of the meteorological impact on regional air pollution, a detailed three-dimensional flow structure is an essential prerequisite to the understanding of the etiology of an air pollution episode. Observations, while generally accurate and reliable, often fail to provide such detailed information due to the limited observational coverage. This is especially the case in the vertical direction. On the other hand, realistic three-dimensional meteorological modelling could provide us with such information at a considerably lower cost. Once validated against observations, model output could be used for many other purposes, e.g., studying the pollutant transport and diffusion. In this study, a three-dimensional windfield simulation will be performed for one selected ozone episode day in the LFV with the aid of the RAMS model. The configuration of the RAMS model used for this study will be discussed in this chapter.

2.2 RAMS Configuration

The RAMS model is a merging of three models that were designed to simulate different atmospheric circulations. These were a non-hydrostatic cloud model and two hydrostatic mesoscale models (McNider and Pielke, 1981; Pielke, 1974a; Pielke, 1974b; Tremback et al., 1986; Tripoli and Cotton, 1982). Because of this, RAMS is a general and flexible limited-area, finite-difference modelling system rather than a single-purpose

model (Pielke et al., 1992). The atmospheric model is constructed around the full set of primitive dynamical equations which govern atmospheric motions, and supplements these equations with optional parameterizations for turbulent diffusion, solar and terrestrial radiation, moist processes, sensible and latent heat exchange between the atmosphere and multiple soil layers, the kinematic effects of terrain, and cumulus convection (Walko and Tremback, 1991). This model system is suitable for the study of thermally-forced, terrain-induced mesoscale phenomena.

Table 2.1 lists the important parameters and options of RAMS used in this study. In addition, the choice of some important parameters, the input data, and an important modification that was made to the RAMS' surface temperature prediction and surface flux calculations, will be discussed.

2.2.1 Model Domain and Grid Structure

Grids in the model use the Arakawa type C grid stagger. Scalar variables are assigned to the centres of grid boxes while velocity components are designed to lie in the midpoints of the grid-box faces or sides normal to their direction of motion.

As real topography is involved in this modelling study, a terrain following or "sigma-Z" coordinate system (Gal-Chen and Somerville, 1975) is chosen to permit more efficient use of computer resources, and to simplify the application of lower boundary conditions.

A decision has to be made first on the size of a model domain and the resolution for both horizontal and vertical direction. Ideally the model domain should include as many of the meteorological effects on the air pollution episodes in the LFV, and the resolution should be fine enough to resolve most of the terrain features and surface inhomogeneities in the valley. Yet the constraint of the available computer resources should also be taken into account. The LFV has its north wall, the Coastal Mountains, merge with its southeast wall, the Cascade Range, in the east. The only opening in the LFV is

Table 2.1: RAMS meteorological model configuration used in the LFV simulations.

Model Characteristic	**Option Used**
Model mode	non-hydrostatic
Numerical scheme	
Nested grids	not used
Coordinate system	terrain-following
Grid dimensions	100 x 68 x 26(complete domain) 72 x 44 x 26(domain of interest)
Horizontal spacing	2.5km x 2.5km
Vertical spacing	100m at surface, 1.15 stretch factor, maximum spacing 2000m, 19km top
Horizontal advection	second-order leapfrog
Vertical advection	second-order forward
Time differencing	forward-backward time-split
Time step	40 s long, 8 s short
Parameterizations	
Radiation	Mahrer and Pielke's shortwave, longwave schemes
Moist processes	passive water vapour only: no condensation
Horizontal diffusion	Smagorinsky's deformation K (coefficient=0.5)
Vertical diffusion	Smagorinsky's deformation K (coefficient=0.5)
Surface layer	Louis scheme
Boundary conditions	
Lateral boundaries	Klemp-Lilly radiative
Upper boundary	rigid top
Bottom boundary	semi-empirical surface energy balance scheme to prognose surface temperature for various landuse types.
Initialization	horizontally homogeneous
Other aspects	
Start time	0500 PST, August 23, 1985
Simulation length	24 h

on the west side facing Georgia Strait and Vancouver Island. The series of mountain chains outside the valley make this V-shaped valley an essentially isolated region. With the synoptic weather pattern usually being a stagnant high-pressure system during a severe ozone episode, air pollution buildup in the valley is mainly orchestrated by the terrain-induced mesoscale flows in the region. Based on this rationale, the model domain is selected to cover the whole LFV and a small area outside the LFV (Fig 1.1). Also because of the static nature of synoptic conditions during ozone episodes, nested grids are not used. This simplifies the simulation and avoids the possible distortion of flows caused by the interactions between different grids.

Horizontal Discretization

While nested grids are not necessary for this study, problems arise for this limited-area modelling study due to the influence of the artificially imposed lateral boundary conditions on the flows generated in the model domain. A common technique to circumvent this problem is to extend the boundaries as far away from the domain of interest as possible. Since a stretched grid spacing scheme in the horizontal is not available in the RAMS model, a buffer area with constant grid spacing was added outside the domain of interest. The terrain height at each grid point in the buffer area has been assigned to be the same as that of the domain of interest boundary point it directly faces with the exception at the southwest corner where real smoothed terrain is imposed instead. The model domain of interest covers a rectangular area from 48.5 degrees latitude south to 49.5 degrees latitude north, and from 121.5 degrees longitude east to 124 degrees longitude west. Horizontal grid spacing has been set to 2.5 km on both sides. That makes a horizontal grid of 100 x 68 points covering a total model area of 250km by 170km with the domain of interest consuming 72 x 44 points and an equivalent area of 182km by 110 km (Fig. 2.1). The buffer area occupies a band 28 and 24 grids wide in East-West, and

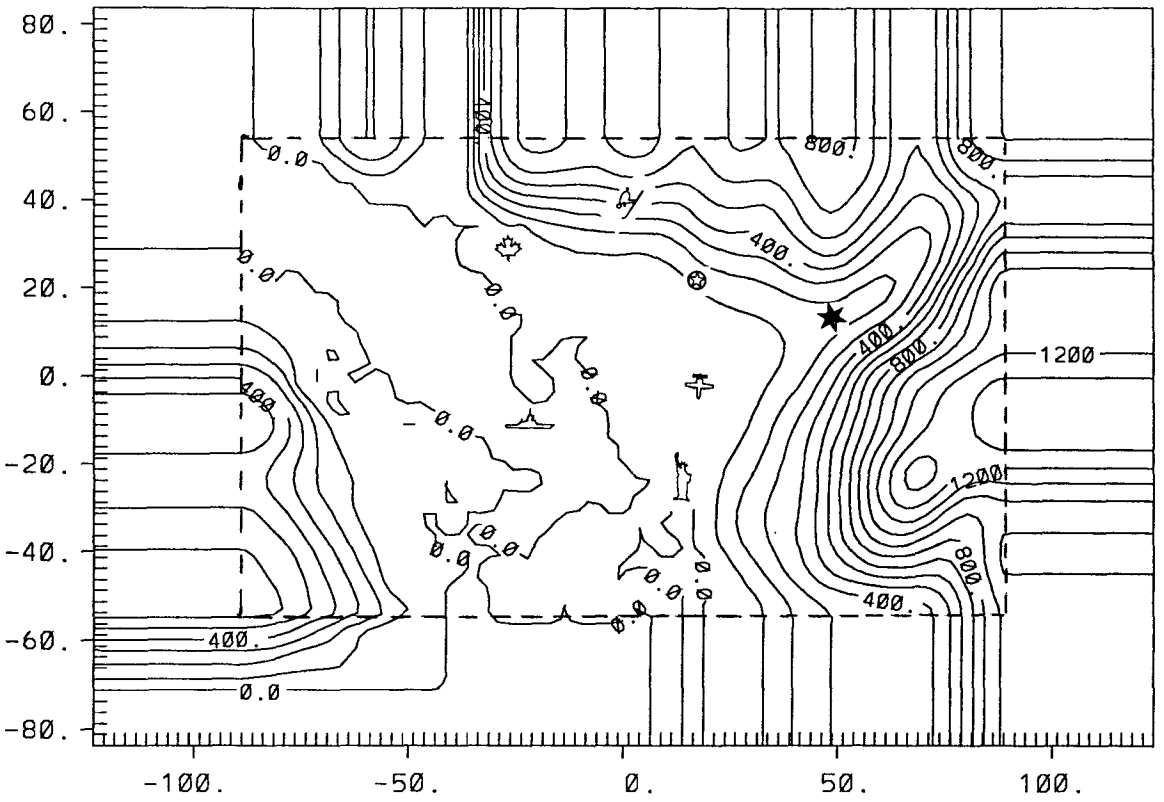

Figure 2.1: Smoothed terrain contour map for the model domain that includes the model domain of interest (inside the dashed line) and the buffer area (outside the dashed line). Contour interval is 100 metres. Outer labels are in units of km. Symbol refers to Vancouver; to Tsawwassen; to Bellingham; to Abbotsford; ★ Chilliwack; to Mission City and to Pitt Lake.

North-South directions, respectively outside the domain of interest.

Vertical Discretization

Vertical discretization uses stretched grid spacing. This stretched vertical spacing enables more detailed vertical structures of the mesoscale flows to be presented as a result of finer spacing near the surface, and enables the top of the domain to be placed well beyond the mesoscale flow active zone, with coarser grid spacing in the upper levels. Grid spacing of 100 metres, stretch ratio of 1.15 and a maximum grid spacing of 2000 metres

are assigned to this study. A total of 26 vertical levels are used. The top of the domain is therefore as high as 19 km. The resultant vertical discretization is listed in Table 2.2. Vertical grid spacing smaller than 100-metre is not permitted according to Mahrer (1984), who showed that too fine a vertical resolution may lead to a numerically inconsistent approximation of the horizontal pressure gradient terms. To avoid this problem, he showed that, at the surface, the smallest vertical grid interval must satisfy the requirement that $\Delta z_1 \geq \Delta z_G$, where Δz_1 is the vertical grid spacing in the first model layer and Δz_G is the elevation difference between two horizontally adjacent grid points. In this study, some grid points have elevation differences of greater than 100 metres between their adjacent points (maximum Δz_G is less than 200 metres). Therefore vertical spacing should be at least 100 metres for this study.

2.2.2 Initialization and Initial Data

As discussed in Chapter 1, August 23, 1985 is chosen for this modelling study. This was a significant episode day characterized by clear skies and light winds aloft associated with a broad high-pressure region over the British Columbia-Washington coastal zone and a thermal trough at the surface (Fig. 2.2 and Fig. 2.3). With this synoptic pattern persisting over the day of study as can be easily seen on Figs. 2.2 and 2.3, ventilation in the LFV is restricted and high ozone concentrations may accumulate quite favourably. This invariant nature of the synoptic meteorological conditions also allows us to conveniently impose a constant synoptic weather condition for the simulation period.

A horizontally homogeneous scheme is adopted to initialize the simulation. It is recognized that this initialization scheme leaves room for improvement as it assumes the identical initial wind and temperature profiles at each grid point. In reality, this is hardly true, given the fact that various surface inhomogeneities exist in the LFV. A

Table 2.2: RAMS vertical discretization and initial conditions. **Z** denotes scalar levels and **ZZ** denotes vertical velocity levels in the RAMS Arakawa C stagger in meters. **p**, θ, **q**, **u** and **v** are initial pressure (in Pa), potential temperature (in K), water vapour mixing ratio (in gkg^{-1}), east-west and north-south wind component (in ms^{-1}) respectively, corresponding to scalar levels **Z**.

N	ZZ	Z	p	θ	q	u	v
1	0.	-45.0	102638.0	287.19	8.0	-.14	-.20
2	100.	48.3	101518.3	287.19	8.0	-.14	-.20
3	215.	155.5	100246.4	289.39	8.1	-.45	-.36
4	347.	278.8	98807.3	291.03	8.0	-.55	-.45
5	499.	420.6	97178.2	292.12	7.8	-.65	-.31
6	674.	583.7	95334.0	292.86	7.5	-.70	-.14
7	875.	771.3	93249.6	293.77	7.1	-.71	-.01
8	1110.	987.0	90903.8	295.83	6.2	-.89	-.19
9	1370.	1235.0	88279.9	299.03	4.6	-1.08	-.02
10	1680.	1520.3	85348.8	300.12	4.2	-1.31	.00
11	2030.	1848.3	82083.2	302.58	4.0	-1.68	.00
12	2430.	2225.6	78469.0	305.23	3.8	-2.22	.00
13	2900.	2659.4	74491.6	308.38	3.6	-2.65	.00
14	3440.	3158.3	70135.5	310.70	3.4	-3.00	.00
15	4050.	3732.1	65387.2	312.83	3.2	-3.00	.00
16	4760.	4391.9	60255.6	315.82	2.9	-3.00	.00
17	5570.	5150.7	54765.6	318.69	2.4	-3.00	.00
18	6510.	6023.3	48965.6	323.05	1.4	-3.00	.00
19	7580.	7026.8	42943.5	329.07	0.8	-3.00	.00
20	8820.	8180.8	36807.2	335.99	0.2	-3.00	.00
21	10200.	9507.9	30682.1	343.96	0.1	-3.00	.00
22	11900.	11034.1	24718.3	353.12	0.0	-3.00	.00
23	13800.	12798.5	19051.9	362.92	0.0	-3.00	.00
24	15800.	14755.6	14047.1	372.70	0.0	-3.00	.00
25	17800.	16763.2	10072.0	384.49	0.0	-3.00	.00
26	19800.	18763.2	7066.1	396.48	0.0	-3.00	.00

a)

b)

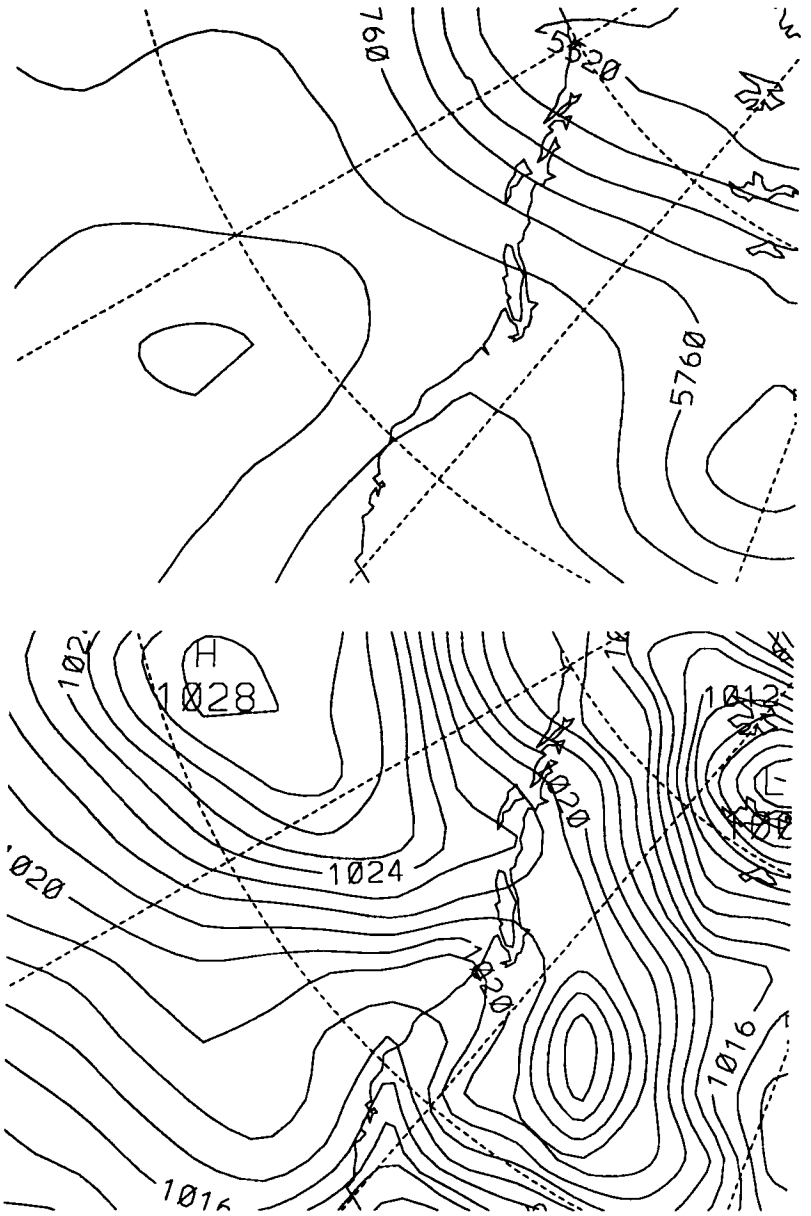

Figure 2.2: a) 500 mb chart for August 23, 1985 1200Z(0400 PST on August 23). Units of contours are in dm. b) Corresponding sea level pressure chart. Units of contours are in mb.

a)

b)

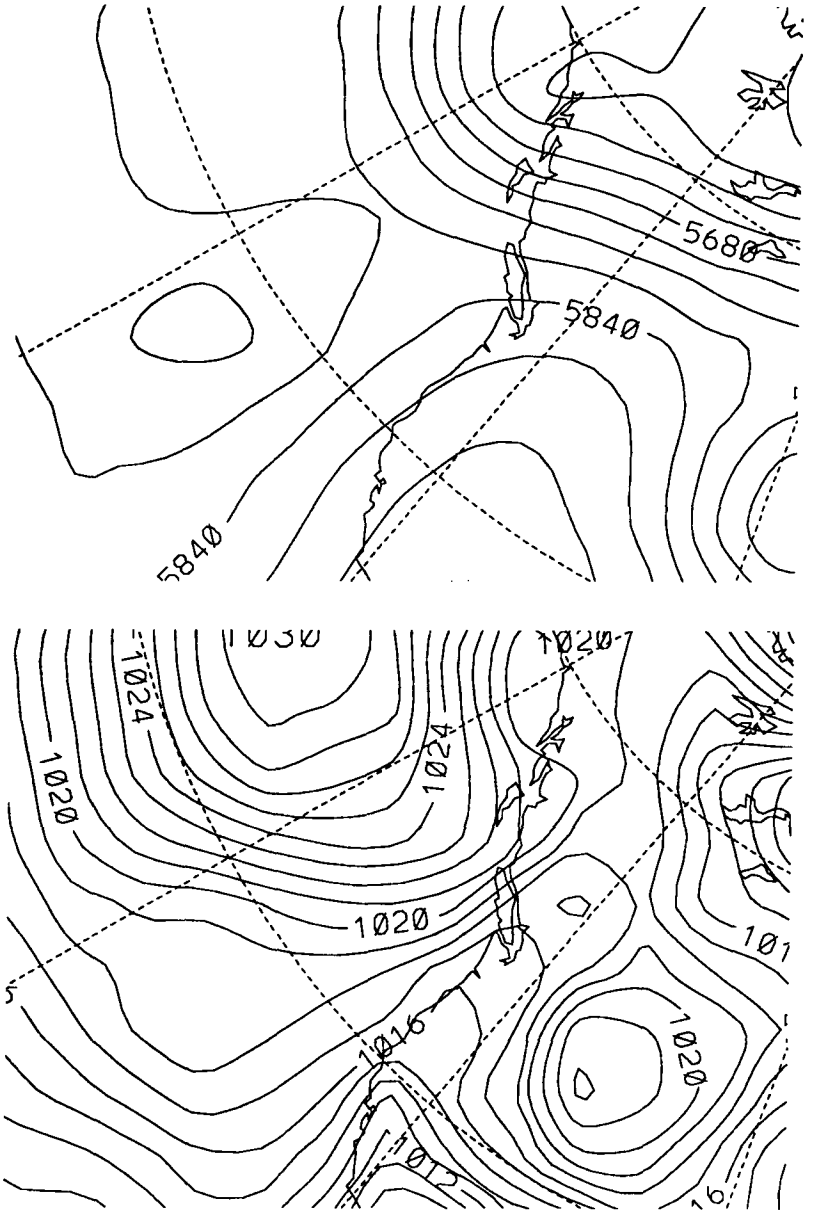

Figure 2.3: a) 500 mb chart for August 24, 1985 0Z(1600 PST on August 23). Units of contours are in dm. b) Corresponding sea level pressure chart. Units of contours are in mb.

more accurate approach would be the use of a variable initialization scheme if sufficient sounding stations were available.

This initialization deficiency is presumed to be remedied within a few hours after the simulation is started as the model quickly adjusts itself to the strong daytime solar heating. The simulation starts near sunrise at 0500 PST. Vertical profiles of potential temperature and specific humidity at initialization were derived from a composite of the 1200Z radiosonde sounding at Quillayute (200km to the southeast of Vancouver) and a tethersonde sounding (0545 PST) from Queen Elizabeth Park in Vancouver. The input initial wind profile is based on the Queen Elizabeth Park tethersonde sounding, the Quillayute sounding as well as a pilot balloon sounding from Vancouver International Airport, and was adjusted by an Ekman spiral wind profile. The determination of a proper initial wind field proves to be far more difficult than that of the initial temperature field because of the more variable nature of the wind field across the valley. However, Pielke (1984) argued that if the ratio of the advection and horizontal pressure gradient force $I_0 = U^2/R\delta T$, (U is the characteristic horizontal velocity, δT is the representative magnitude of the horizontal temperature variations across the mesoscale system and R is the gas constant for dry air (287 $JK^{-1}kg^{-1}$)), is much smaller than unity, an accurate wind initialization is less important than that for temperature. Such is the case in this study, as the wind speed is of the order of only several metres per second and the horizontal temperature difference as large as 10 degrees between land and water. This means that I_0 is far less than unity, thus justifying the initialization method and procedure. Table 2.2 lists these initial profiles together with the vertical discretization.

2.2.3 Boundary Conditions

As Moran (1992) pointed out, boundary conditions are an integral and important component of a limited-area model since time-dependent boundary conditions must be

specified in order to close any initial-boundary value problem. While specification of the bottom boundary conditions is relatively straightforward, specification of the lateral and upper boundary conditions has been a thorny problem since the earliest days of numerical weather prediction (Charney, Fjortoft and Neumann, 1950; Oliger and Sundstrom, 1978; Platzman, 1954; Platzman, 1979). This is not too surprising considering the artificiality of conceptually 'cutting out' a finite volume of the atmosphere. The model boundaries must then be perfectly transparent, i.e., 'open', both to flow 'information' travelling from the atmospheric exterior into the model interior by advection or wave propagation and to flow structures or disturbances generated within the model domain and propagating away from their source. Ideally, the lateral and upper boundaries should not be reflective or refractive in any way nor should they themselves be the source of any disturbances or noise.

Lateral Boundary Conditions

It is very difficult, if not impossible, to make the lateral boundaries totally open given the artificial nature of the boundary conditions. It is therefore always desirable to move the lateral boundaries as far from the region of interest as possible. Following this logic, this study adds a buffer area just outside the domain of interest in order to minimize the effects of the lateral boundaries on the flows.

RAMS offers a variety of lateral boundary condition options, including cyclic conditions in either or both horizontal directions, three different radiative boundary conditions on the normal velocity component and radiative, zero-gradient, or constant conditions on other variables, and two schemes to incorporate large-scale boundary time tendencies. Cyclic conditions are not appropriate in this real topography problem since the values of the dependent variables at one boundary of the model domain are assumed identically equal to the values at the other end. Radiative boundary conditions on the other hand

are more commonly used in mesoscale modelling because they are designed to make variables at the lateral boundaries change in value so as to minimize the reflection of outward propagating perturbations back into the model domain.

Klemp and Lilly's (1978) lateral boundary conditions are selected from three available options in the model, and are applied to all variables. This boundary condition has the advantage that the predicted vertical profile of momentum at the boundary is a linear combination of the previous flow at the boundary and the flow at the vertical grid column adjacent to the boundary. Unlike Orlanski's (1976) or Klemp and Wilhelmson's (1978) radiation condition, large imbalances of horizontal momentum flux integrated in the vertical which lead to domain scale pressure trends do not occur. This seems to be especially valuable in simulations of flow over topography where a mountain barrier tends to rearrange the vertical profile of horizontal momentum severely.

Upper Boundary Conditions

The top of the mesoscale model, as with the lateral boundaries, should be moved as far as possible from the region of significant mesoscale disturbance. In this study, the top of the vertical domain has been placed as high as 19 kilometres, well inside the stratosphere. Such a setup provides a deep layer of stable thermodynamic stratification which could effectively minimize the vertical advection or propagation of mesoscale disturbances from reaching the top of the domain. Therefore the choice of a proper upper boundary condition becomes less important in this case; rather, economics and efficiency occupy more weight in making the choice. Among four available options provided by RAMS, only "wall on top" and the "Klemp-Durran radiative" upper boundary conditions could be used for the nonhydrostatic mode. "Wall on top" is selected as the top upper boundary condition for this study. Sensitivity studies showed that model studies using the " wall on top" option presented no appreciably different results from that with

the Klemp-Durran radiative upper boundary condition, while consuming significantly less CPU time.

Bottom Boundary Conditions

The realistic specification of bottom boundary conditions is important when terrain forcing is significant, as it is expected to be in this study. The imposed kinematic bottom boundary conditions used are the "no slip" condition in the tangential direction and zero velocity in the normal direction. For the surface temperature and surface fluxes, the RAMS model has two multi-level soil models to predict surface temperature and soil moisture for 12 classes of soil and uses surface-layer similarity theory to diagnose surface fluxes. As much of the LFV is urbanized or covered in vegetation, applying a pure soil model to various complex land surfaces is inappropriate. In this study, soil models were replaced with a semi-empirical energy balance model which is able to predict the surface temperature and surface fluxes for five typical landuse types in the LFV. The details of this model will be discussed later. As a first step, terrain, and surface properties for each landuse type will be discussed below.

Terrain and Surface Properties Terrain height data were obtained from a 1 km dataset developed by Ministry of Energy Mines and Resources, Canada. The data were first averaged to 2 km using 4 points (2 x 2), and then interpolated to 2.5 km using an inverse distance weighting method. The resultant dataset is smoothed by a binomial filter to eliminate wavelengths less than two grid lengths. This smoothing procedure is necessary to maintain computational stability within the numerical scheme. The smoothed terrain contour map for the domain of interest is displayed in Fig. 2.1, together with the buffer area discussed before. With this resolution, the principle features of the regional terrain are retained.

Table 2.3: Roughness Length and Albedo for Each Land-use Type.

Land-use Type	Urban	Suburban	Rural	Agricultural	Forest
Roughness (m)	1.8	0.6	0.5	0.25	1.5
Albedo	0.15	0.18	0.19	0.23	0.15

One important surface inhomogeneity is the water and land contrast. Therefore a 2.5km x 2.5km resolution "percentage-of-land" data file was built up for the model domain from the UTM grid system maps.

In addition, various surface inhomogeneities over land should be identified and included in the model application if simulations are to be in correspondence with observations. Five broad landuse categories representing urban and suburban environments, forested mountain regions, and rural and agricultural areas have been recognized in the model region as being shown in Fig. 1.1. Two important surface properties, aerodynamic roughness length and albedo are assigned for each landuse type through survey, observations (roughness for forested and suburban areas in the LFV) (Lee, 1992; Steyn, 1980), and consultation with experts and recognized values for similar landuse types (Lewis and Carlson, 1989; Oke, 1989; Steyn and McKendry, 1988; Wieringa, 1991). Table 2.3 displays these two surface property values for each landuse type.

Surface Temperature and Fluxes As mentioned earlier, an effort has been made to develop a realistic, yet semi-empirical surface energy balance model to predict surface temperature and surface fluxes for each landuse type. This model is made possible by the recent developments and extensive observational studies of the surface energy balance in this region (de Bruin, 1983; de Bruin and Holtslag, 1982; Camuffo and Bernardi, 1982; Cleugh, 1990; Deardorff, 1978; Grimmond, Cleugh and Oke, 1991; McCaughey, 1985; McCumber, 1980; McNaughton and Spriggs, 1987; Monteith, 1981; Oke, 1989). A

complete description of the model and the specific surface properties used in the model for each landuse type are given in Appendix A. In brief, this model adopts Mahrer and Pielke's (1977b) short- and long-wave radiation parameterization scheme to calculate the net radiation for every 600 seconds (15 times the long time step). It relates the storage heat flux ΔQ_S directly to net radiation Q^* by an objective hysteresis model (Grimmond, Cleugh and Oke, 1991), and the latent heat flux Q_E to the difference between net radiation and the storage heat flux through the Priestley and Taylor equation (Priestley and Taylor, 1972). The remaining term, the sensible heat flux Q_H, is calculated through Louis'(1979) analytic functions. Ground surface temperature is then solved in this surface energy balance equation through iteration. This surface temperature is, in turn, used to obtain the needed fluxes. Care has been taken to make this model compatible with the rest of the RAMS model code.

Chapter 3

Results and Model Validation

The model is evaluated based on a comparison between modelled outputs and observations. Particular focus is placed on the model's ability to reproduce the observed forced mesoscale flows in the LFV.

A 24-hour simulation was carried out for the period starting at 0500 Pacific Standard Time (PST) 23 August 1985 (near sunrise). Prior to the scheduled run, dynamic initialization periods of one-hour, two-hour and four-hour were applied, as suggested by Steyn and McKendry (1988) in order to achieve realistic nocturnal flow features at sunrise. Unfortunately the results showed that the predicted nocturnal winds were too strong. Therefore dynamic initialization was not used in the final model run. Model output was recorded every hour. The model run was performed on an IBM RS/6000, and consumed about 24 hours of CPU time.

Extensive observations were carried out in the LFV during the period of interest (Steyn and McKendry, 1988). The observation network is displayed in Fig. 3.1. Surface winds and directions at a height of 10 m above ground level (AGL) were monitored continuously at 25 locations on the valley floor. Eight of the stations operated by the University of British Columbia also monitored temperature with identical shielded thermistors installed at the same height. In addition, direct measurements of the energy balance components Q^* (surface net all-wave radiation) and Q_H (sensible heat flux) were available until midafternoon from a suburban location. The storage heat flux ΔQ_S was calculated using a hysteresis model developed by Grimmond, Cleugh and Oke (1991)

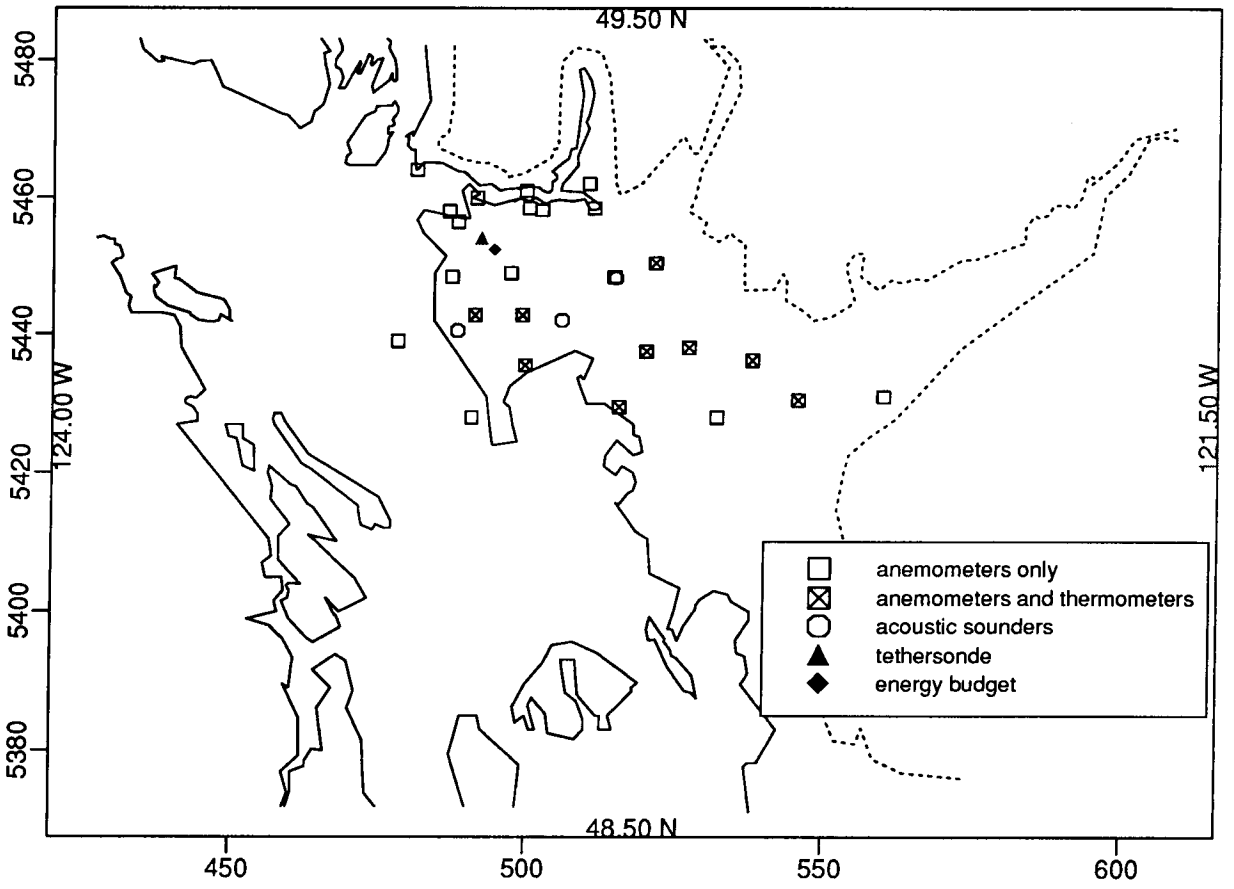

Figure 3.1: Observation network for August 23 1985 in the LFV. The solid line is the coastline. The dashed line is the 100 metre terrain contour, showing the edge of the valley wall. Outer labels are in units of UTM coordinates ($x10^3$).

while Q_E (the latent heat flux) was calculated from residuals. Vertical variations in wind speed and direction, temperature and humidity were derived from tethersonde soundings carried out at Queen Elizabeth Park, Vancouver during the daytime. Soundings were made continuously and took about one hour for an ascent and descent. Three acoustic sounders located in the valley were also used to monitor the vertical thermal structure and to give an indication of mixed layer depth.

Evaluations of model performance are made both quantitatively and qualitatively. Comparison between this model performance and that of Steyn and McKendry (1988) has also been conducted briefly. Model evaluation is necessary in order to establish the credibility of the RAMS output and enable us to use the validated output to perform further investigations.

3.1 Quantitative Evaluation of Model Performance

Willmott (1985) recommended that quantitative evaluation of model performance be based on the following groups of parameters:

- Observed and modelled means and standard deviations;
- Total, systematic, and unsystematic root mean squared differences (RMSD, RMSD_S, RMSD_U) between observed and modelled values (scalars or vectors). Total RMSD represents the total difference between modelled values and observations. The systematic RMSD represents model linear bias while the unsystematic RMSD represents model precision. These parameters are defined as (Willmott, 1982; Willmott, 1985):

$$\text{RMSD} = \left[\frac{1}{N}\sum_{i=1}^{N}|\mathbf{p}_i - \mathbf{o}_i|^2\right]^{0.5} \tag{3.1}$$

$$\mathrm{RMSD}_S = \left[\frac{1}{N}\sum_{i=1}^{N}|\hat{\mathbf{p}}_i - \mathbf{o}_i|^2\right]^{0.5} \tag{3.2}$$

$$\mathrm{RMSD}_U = \left[\frac{1}{N}\sum_{i=1}^{N}|\hat{\mathbf{p}}_i - \mathbf{p}_i|^2\right]^{0.5} \tag{3.3}$$

where N is the number of stations; $\mathbf{p}_i$ and $\mathbf{o}_i$ are modelled and observed variables respectively; $\hat{\mathbf{p}}_i$ is the ordinary least square estimate of $\mathbf{p}$ ($\hat{\mathbf{p}}_i = a + b\mathbf{o}_i$, where a and b are the intercept and slope). Areal weight has been assumed to be unity for each station.

- The Index of Agreement d, which is defined as:

$$d = 1 - \frac{\sum_{i=1}^{N}|\mathbf{p}_i - \mathbf{o}_i|^2}{\sum_{i=1}^{N}(|\mathbf{p}_i - \bar{\mathbf{o}}| + |\mathbf{o}_i - \bar{\mathbf{o}}|)^2} \tag{3.4}$$

where $\bar{\mathbf{o}}$ is the simple mean of the elements in $\mathbf{o}$. This dimensionless index has a theoretical range of 0.0 (for no agreement) to 1.0 (for perfect agreement).

It must be pointed out that this statistical method assumes that all observations are error-free and that all errors come from model simulations. Therefore it is very important to filter out the erroreous observational data before applying the statistics.

According to Willmott (1981), this set of statistical measures is necessary and sufficient for the complete assessment of model performance. These validation statistics have been applied in atmospheric modelling by Steyn and McKendry (1988), Ulrickson and Mass (1990b) and Jackson (1993). This study will employ the same method to compare RAMS surface wind and temperature fields, with observed surface data, covering 24 hours during which a sea-breeze circulation was observed in the LFV. All data are hourly means. Before comparison, modelled fields were extrapolated to the observation height of 10 metres AGL from the lowest model level of 48.3 metres. Businger's profile functions (Businger et al., 1971) are used to make the extrapolation. Friction velocity u_*, Monin-Obukhov length L, scaling temperature θ_* and surface potential temperature θ_0

are extracted from the model results and applied to Businger's profile functions together with specified roughness length z_0. The extrapolation is made within the RAMS model run.

3.1.1 Surface Wind Evaluation

Figures 3.2a and b display time series of observed and modelled surface mean wind direction and speed on August 23, 1985. From Fig. 3.2a, it can be seen that the modelled average wind direction is in close agreement with that observed throughout the day except near sunrise (transition period from land breeze to sea breeze) and near midnight (transition period from sea breeze to land breeze), when winds in the valley are very light (less than 1 ms^{-1}). Wind direction is almost persistently westerly during the day, indicating the prevalence of the sea breeze. Modelled average wind speeds follow the observed pattern quite closely in most hours with a maximum of about 3 ms^{-1} occurring at about 1500 PST (Fig. 3.2b). The relative magnitudes also show good agreement but with a slight tendency for the model to overpredict the wind speed around the peak and after 2100 PST at night.

Figures 3.3a-c show, respectively, the wind standard deviation, root mean square differences and Index of Agreement. The modelled wind standard deviation is less than the observed value by up to 1 ms^{-1} until 1900 PST. This is to be expected as modelled surface winds represent the winds over a volume of 2.5km x 2.5km x 48.3m (later extrapolated to 10m) and do not include subgrid scale effects, while observations must be significantly affected by local surface conditions. At night, however, the transition from sea breeze to land breeze and from upslope to downslope make the wind field in the valley very variable. This effect, together with the slight overprediction of modelled wind speed, may be the cause of the larger modelled standard deviation at night. The total RMSD in Fig. 3.3b indicates that the model capably simulated the observed wind

field, with total RMSD values no greater than 2 ms^{-1} thoughout the simulation. The systematic component $RMSD_S$ is the major contributor to the total RMSD. The small unsystematic component $RMSD_U$ indicates good precision. The Index of Agreement is another important tool in evaluating model performance and is especially useful in making cross-comparions between models (Steyn and McKendry, 1988; Willmott, 1985). Figure 3.3c shows that except for the first two hours of the simulation when the model was adjusting itself to the solar radiation and overcoming the inexact initialization, the index stays consistently around 0.6 with an average of 0.58.

Steyn and McKendry (1988) studied the same event in the LFV with a hydrostatic Colorado State University Mesoscale Model (CSUMM) and used the same statistical methods to evaluate their model results. For the wind field evaluation, their results had an Index of Agreement ranging between 0.41 to 0.61 and with a average of 0.51. Clearly the present modelling study has an improved overall performance.

3.1.2 Surface Air Temperature Evaluation

Surface heating is an important driving force in inducing sea breezes and slope winds. Its realistic representation by the model will influences the success of wind field simulations. A direct index of such surface heating is the near surface air temperature (10 metres AGL).

Figure 3.4a presents the evolution of observed and modelled near-surface air temperature, and shows relatively close agreement between them, with peak temperatures occurring at 1600 PST in both cases. Modelled temperatures tend to underestimate the observed values in the daytime by up to 3 degrees and overestimate the observed values at night. A comparison of standard deviations in Fig. 3.4b reveals that the observed fields have greater spatial variation than the modelled fields, presumably because the model only dealt with five broad landuse types in the LFV while in reality every station may

a)

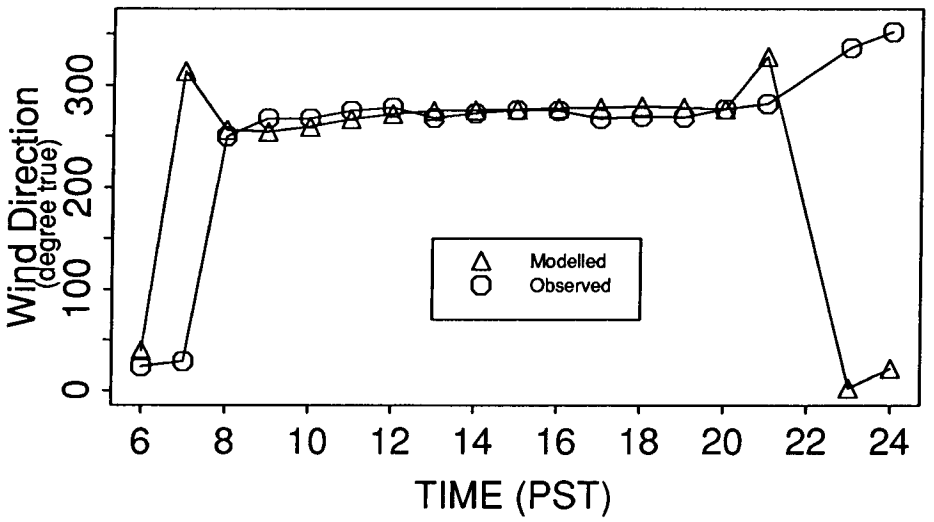

b)

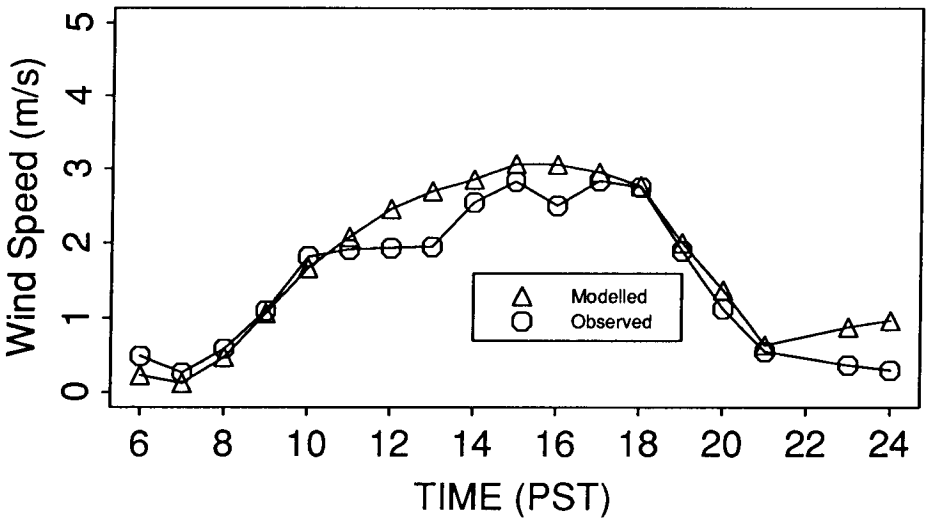

Figure 3.2: The evolution of modelled and observed: a) average wind direction, b) average wind speed for August 23, 1985.

a)

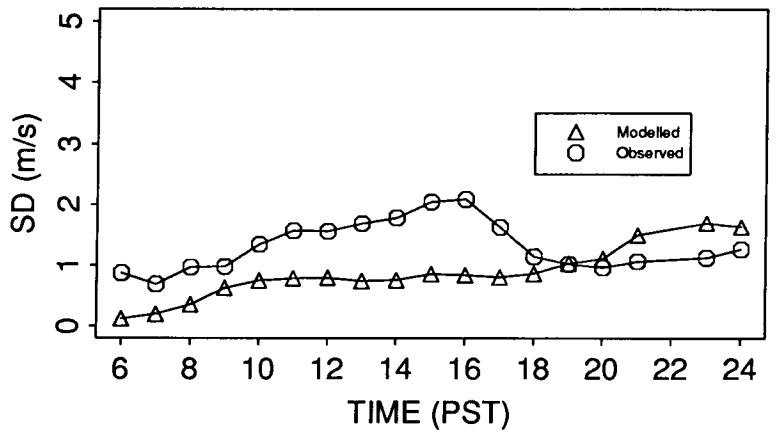

b)

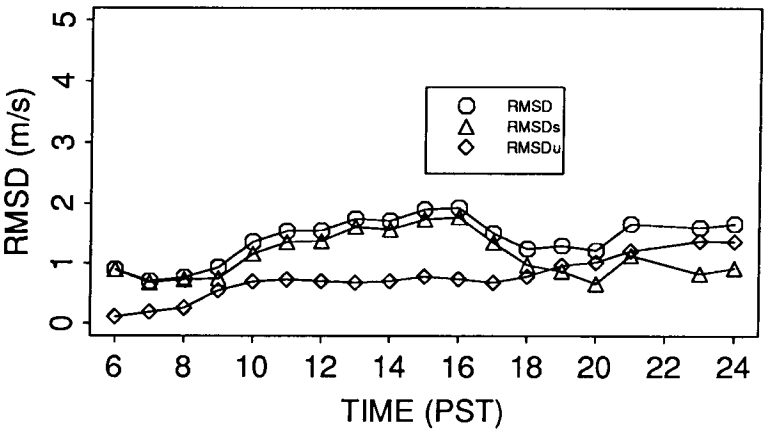

c)

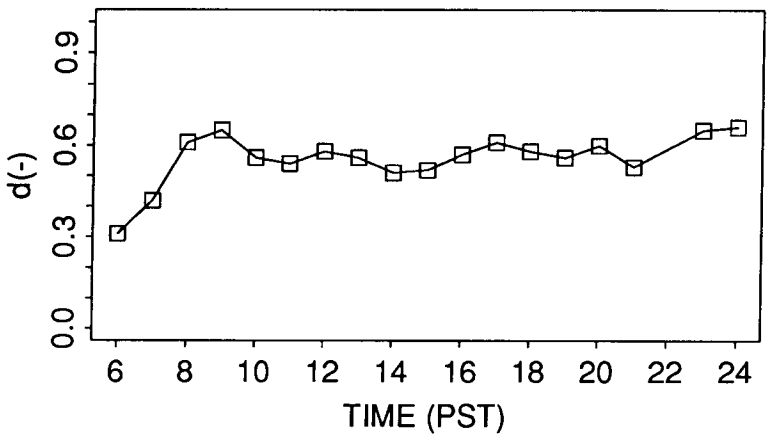

Figure 3.3: Statistic comparison of modelled and observed wind as time series of a) standard deviation of wind speed, b) total (RMSD), systematic (RMSDs) and unsystematic (RMSDu) root mean square deviations and c) index of agreement for August 23, 1985.

a)

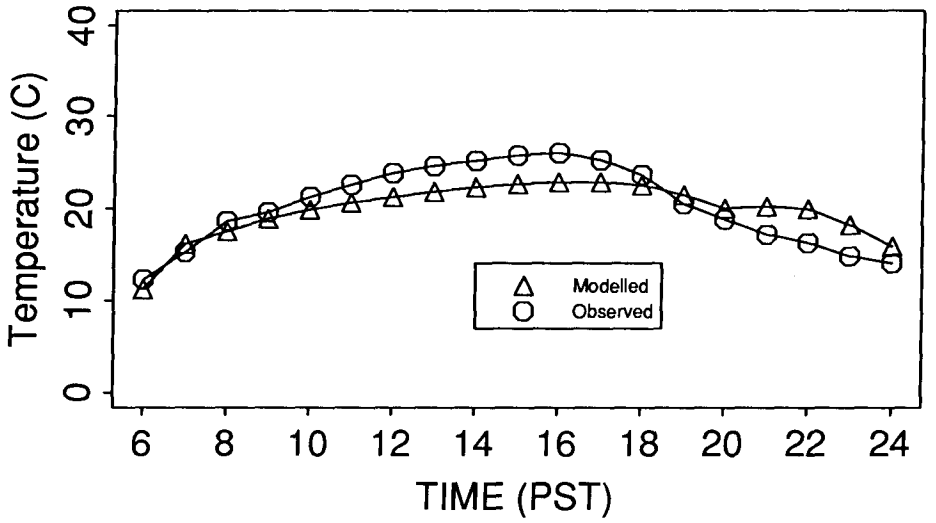

b)

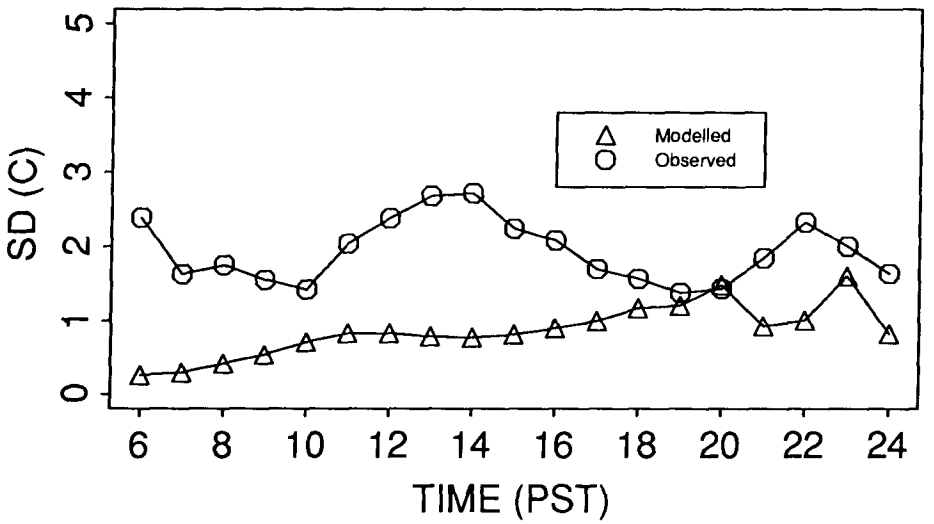

Figure 3.4: The evolution of the modelled and observed: a) average temperature, b) standard deviation of temperature for August 23, 1985.

a)

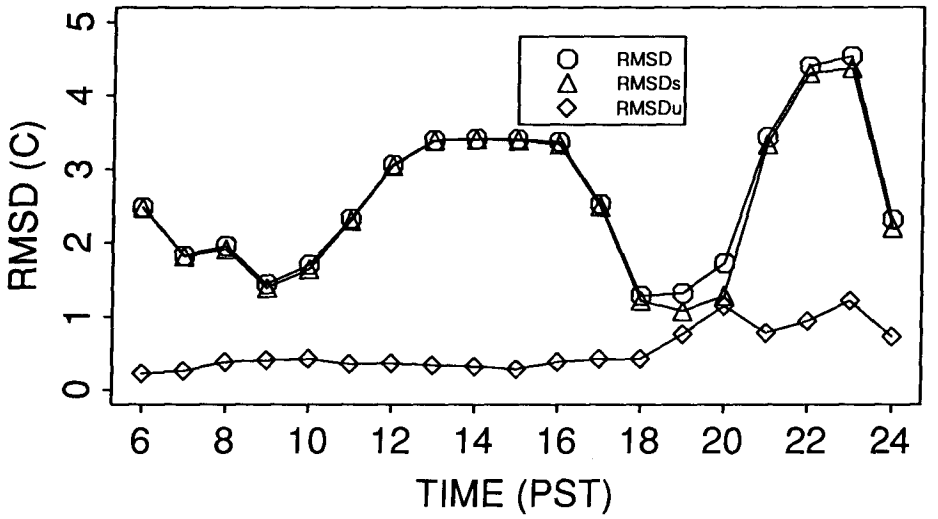

b)

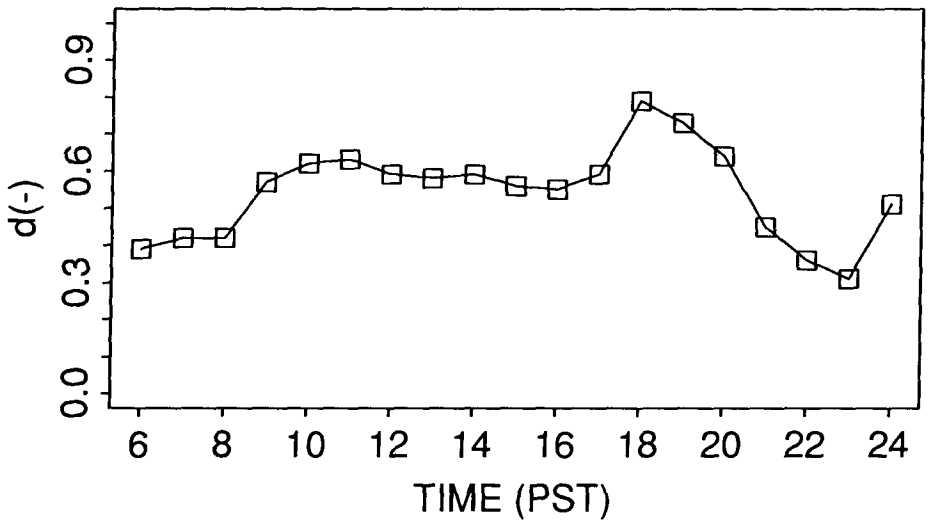

Figure 3.5: The evolution of the modelled and observed: a) total (RMSD), systematic (RMSDs) and unsystematic (RMSDu) root mean square deviations of temperature, b) index of agreement for August 23, 1985.

be exposed to a different surface environment. The less variable modelled wind fields, as previously mentioned, may also be the cause for the smaller variation in the modelled temperature fields. It is worthy of mention that the modelled standard deviation tends to increase with time and equals the observed value at 2000 PST, thereafter decreasing. The pattern of the RMSD and the clear dominance of the systematic $RMSD_S$ in Fig. 3.5a show that the discrepancy between modelled and observed temperatures comes mostly from the underestimation of the model near the peak and from the overestimation at night. Again, model precision remains high as the unsystematic RMSD remains low throughout. The Index of Agreement (d) (Fig. 3.5b) is low near sunrise and at night but remains higher than 0.55 during most hours with a maximum index of 0.79 at 1800 PST when the modelled temperature mean matches the observed one exactly and when the RMSD is a minimum. Steyn and McKendry's (1988) temperature Index of Agreement ranged from 0.11 to 0.74, with a mean of only 0.34. This study has a mean d for temperature of 0.54, with a range of 0.31 to 0.79. This is another strong indication that RAMS performs a much better job than CSUMM.

3.2 Qualitative Evaluation of Model Performance

A visual comparison of the observed and modelled wind fields is an important supplement to the above quantitative evaluations. It gives a direct picture of how well the modelled field matches the observed one. In the following two sections, surface wind and vertical profile visualization will be presented.

3.2.1 Surface Winds

Two major differences between the modelled and observed surface wind fields must be taken into account when comparing these fields. Firstly, modelled surface wind fields

represent instantaneous "snapshots" while observed wind fields are hourly means valid for the previous hour. Secondly, modelled wind fields are collected at the lowest model level of 48.3 metres above ground whereas the wind observations were made at 10 metres AGL.

This complicates the comparison but does not result in significant discrepancies for this visual comparison. The magnitude of the modelled wind should be slightly smaller at 10 metres but its direction should be much the same. The instantaneous modelled wind field should be similar to the hourly averaged one as long as the winds are not changing drastically over the course of an hour.

Figures 3.6a-h depict a series of surface wind fields from 0900 PST to 2300 PST on August 23 1985 at 2-hour intervals. Observed wind vectors are represented by bold arrows which overlay the modelled wind fields. As can be seen in Fig. 3.6a, thermally-driven sea breeze and upslope flows have been built up 4 hours after sunrise yet are still very weak. As time progresses, the westerly sea breeze from the Strait of Georgia strengthens while upslope winds also increase in strength and flow up the valley walls (Figs. 3.6c-h). These two winds merge at some point and constitute an integral wind field. Channel flow blowing eastward along the valley also forms as a result of the interactions among the valley wind, the pumping effect of slope winds on both the southeast and northeast walls, and the westerly sea breeze. Around 1500 to 1700 PST, one or two hours after the maximum surface heating, sea breeze and upslope winds come to their maximum (Figs. 3.6d and e). Thereafter the sea breeze continues with diminishing strength until around 2100 PST when it almost ceases and strong downslope winds come down from valley walls to drive the wind seaward. Weak land breezes then start to build, while a stream of southeastward wind continues to flow over the Strait of Georgia.

In the daytime, both the magnitude and direction of the model surface winds show good agreement with observations for most of the 25 stations. They do not coincide

a)

b)

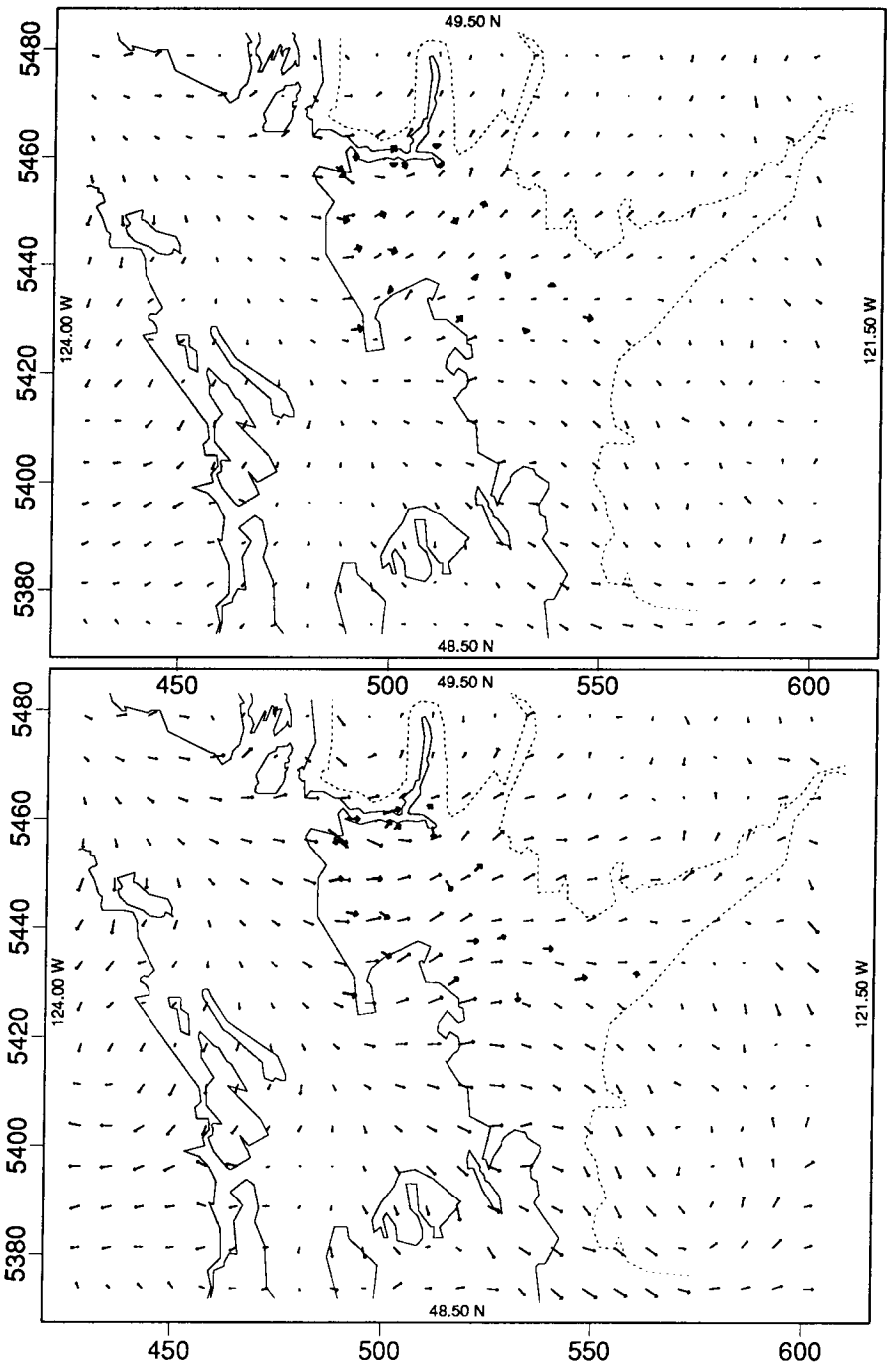

Figure 3.6: (a-h) The observed and modelled surface winds at a) 0900 PST and b) 1100 PST of August 23, 1985. Bold arrows are the observed winds. The dashed line is the 100 metre terrain contour, refering to the edge of the LFV wall. The solid line is the coastline. Outer labels are in units of UTM coordinates (x10^3). Inner labels are latitude or longitude values for the boundaries. The spacing between vector tails represents 7.5 ms^{-1}.

a)

b)

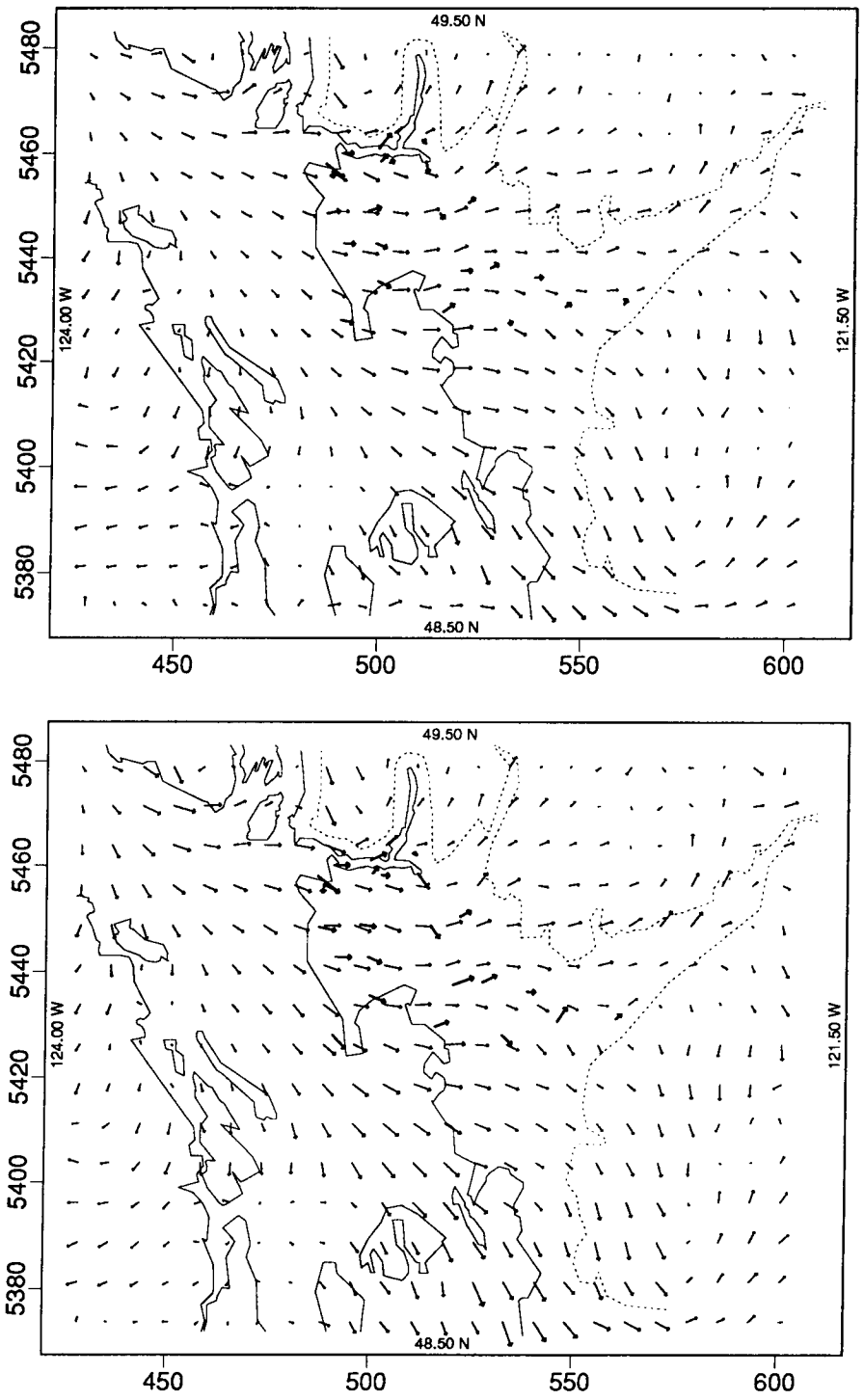

Figure 3.6: c) 1300 PST and d) 1500 PST of August 23, 1985.

a)

b)

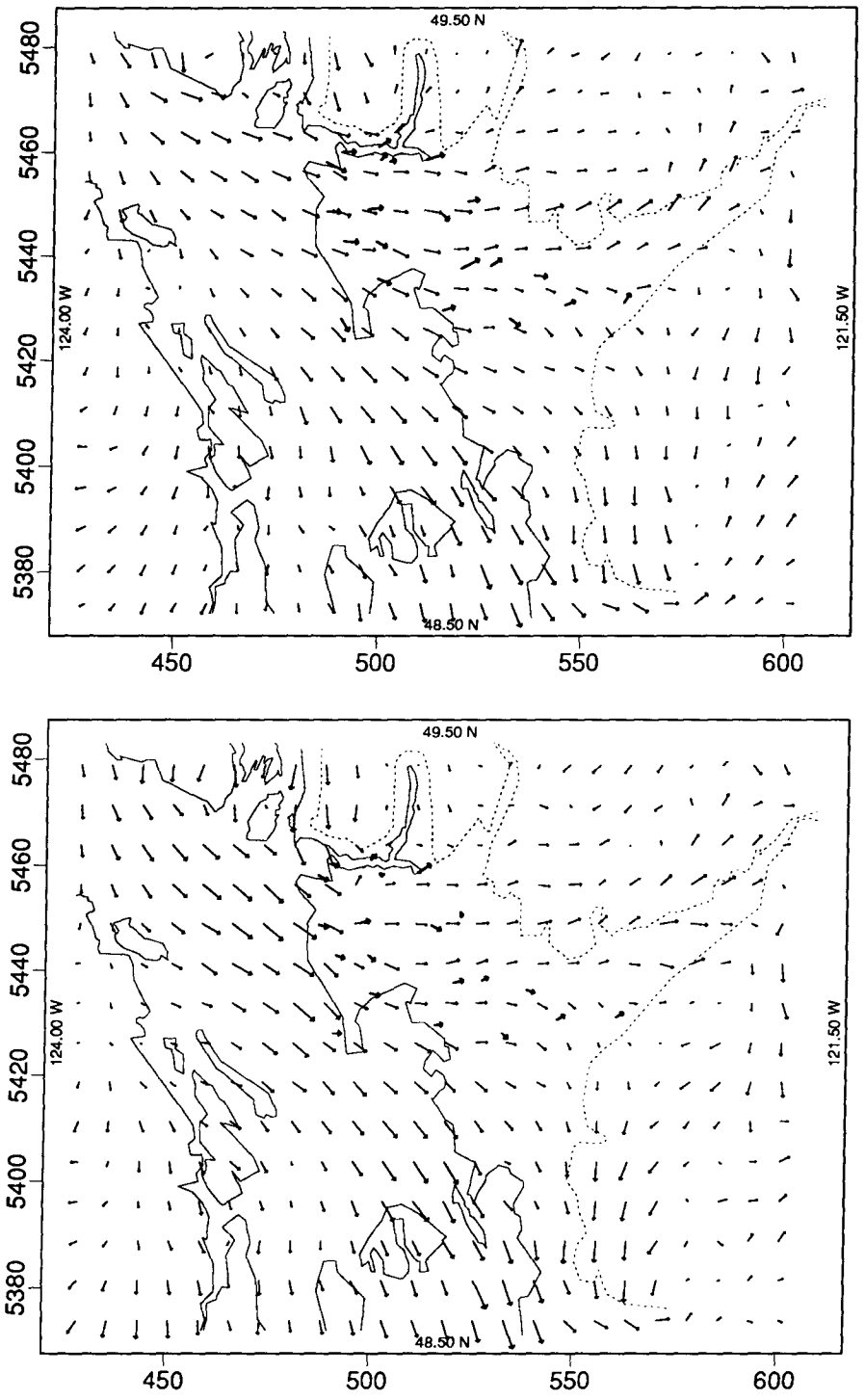

Figure 3.6: e) 1700 PST and f) 1900 PST of August 23, 1985.

a)

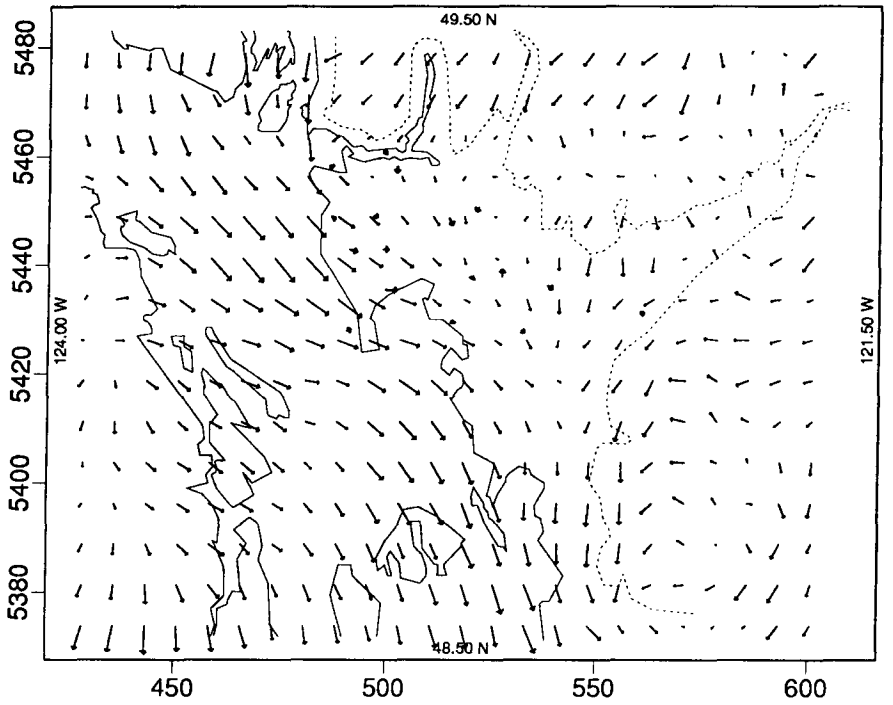

b)

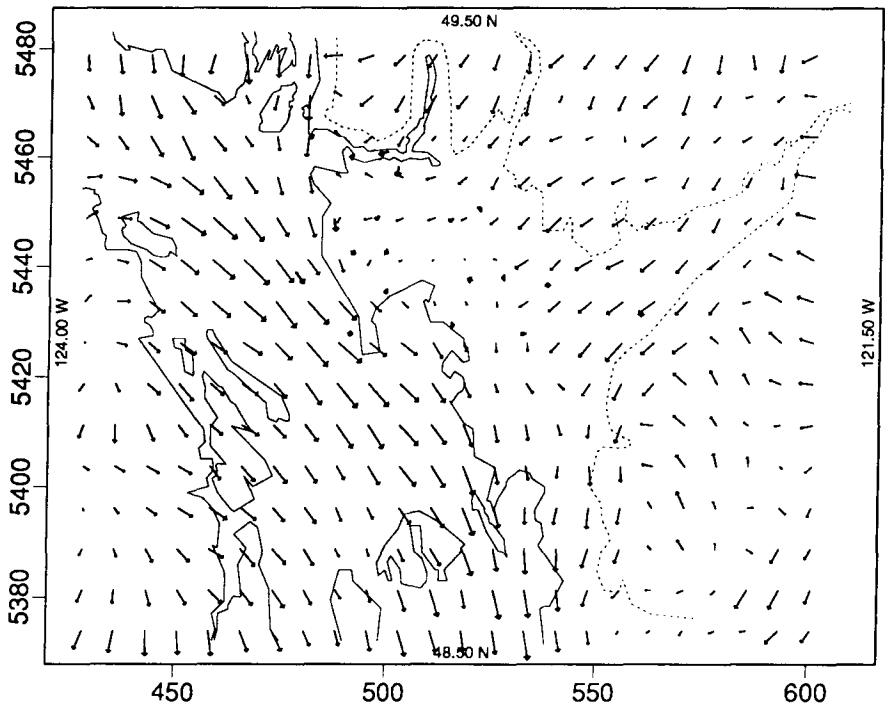

Figure 3.6: g) 2100 PST and h) 2300 PST of August 23, 1985.

as well at night when the model simulated flows along the Strait of Georgia that are significantly stronger than observed (Fig. 3.6g and h). This problem was also encountered by Steyn and McKendry (1988) and may be due to the over-simplified surface heat flux representations over the sea. Their daytime simulations also suffered problems such as overestimating the strength of the sea breeze and unrealistically strong downslope winds along the northwest wall in the daytime. As can be seen in Figs. 3.6a-h, these two problems have been alleviated in this study.

3.2.2 Vertical Profiles

In an attempt to investigate the model's ability to simulate vertical wind profiles, this section conducts a vertical profile comparison at a single urban site in Vancouver where tethersonde measurements were made to provide instantaneous observed vertical profiles. It should be understood that to expect exact duplication of the instantaneous wind profiles is not practical, considering that even the instantaneous observed profiles took about 15 minutes to complete, and that randomness was inevitably involved in monitoring the wind. Therefore, profile patterns and approximate magnitudes are the main focus.

Figures 3.7a-d display the observed and modelled wind profiles of the east-west components at Queen Elizabeth Park for the hours 0900, 1200, 1500 and 1800 PST. General patterns of the modelled profiles are seen to match those of the observed ones surprisingly well in all cases. Moreover, sea breeze and return flow aloft are clearly simulated and the modelled height of zero wind is roughly in agreement with that observed, especially when the sea breeze is strong (Fig. 3.7b and c). However, it is also obvious that the model overpredicts the strength of the observed sea breeze and return flow. A glimpse of the north-south wind component (Fig. 3.8a-d) shows that this component is very small compared with east-west component, indicating the dominance of the westerly sea

breeze. While the small and variable north-south component makes the exact simulation very difficult, the simulated patterns do agree in gross term with the observed ones.

Steyn and McKendry (1988) also performed a comparison of vertical profiles using the same observations. Results from this study demonstrate a clear improvement over their simulations. While one single-point vertical profile validation is not sufficient to identify the success of the model simulation in the vertical direction, it does give us an indication of the RAMS' capability to simulate the vertical structure.

3.3 Conclusions

This chapter shows quantitative and qualitative comparisons between observations and RAMS model output for the episode day of August 23, 1985 in the LFV. The results showed that, overall, RAMS is able to simulate real-world mesoscale flows in complex terrain. Model results show general agreement with the observations made on this day. Comparison with Steyn and McKendry's model performance evaluation reveals that the RAMS model performance was better in almost every respect.

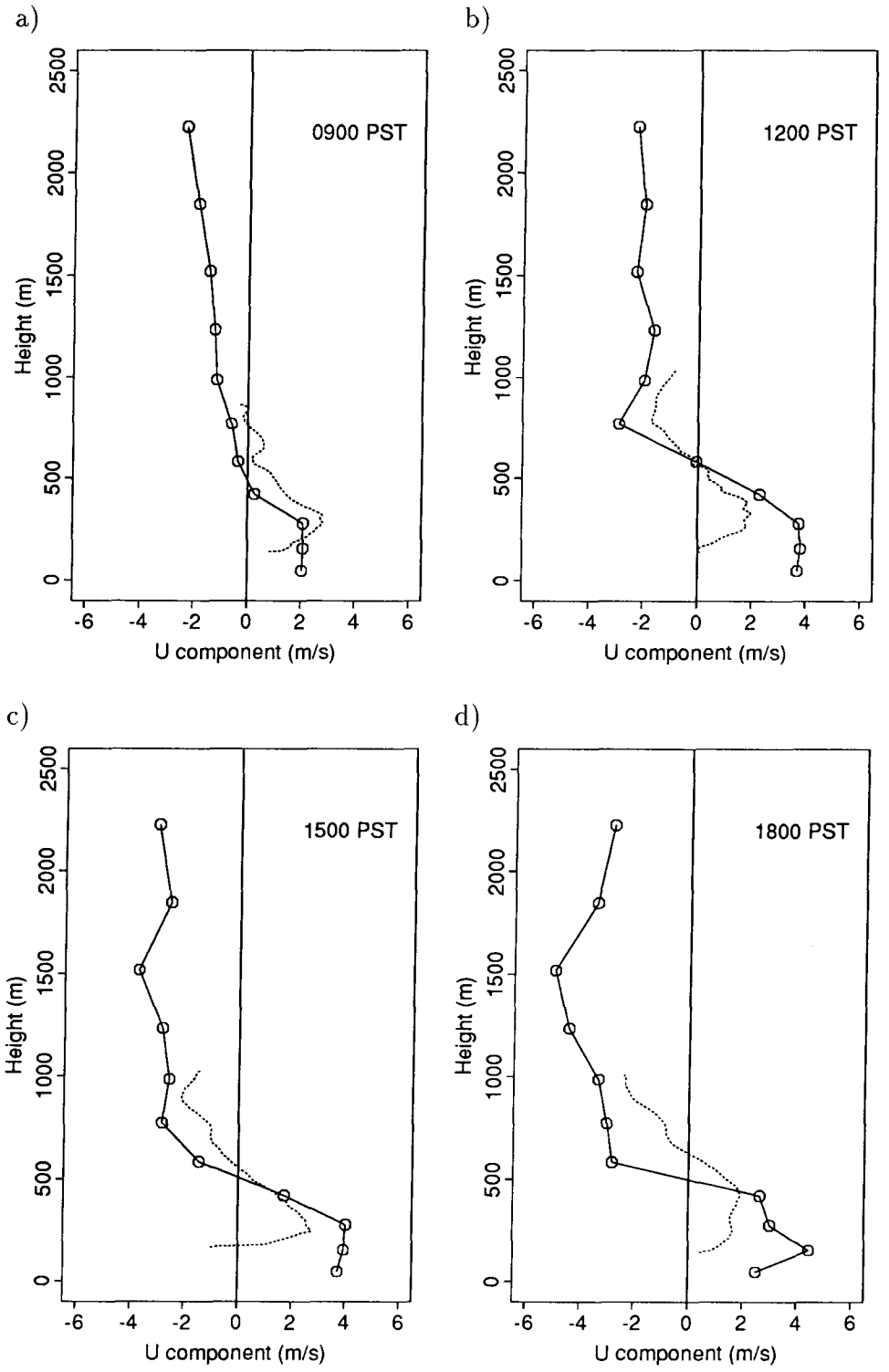

Figure 3.7: Profiles of the east-west component of wind velocity at Queen Elizabeth Park in Vancouver at a) 0900 PST, b) 1200PST, c) 1500 PST, and d) 1800 PST. The solid line refers to the modelled profile; The dashed line to the measured profile. Positive wind speed value indicates a westerly wind.

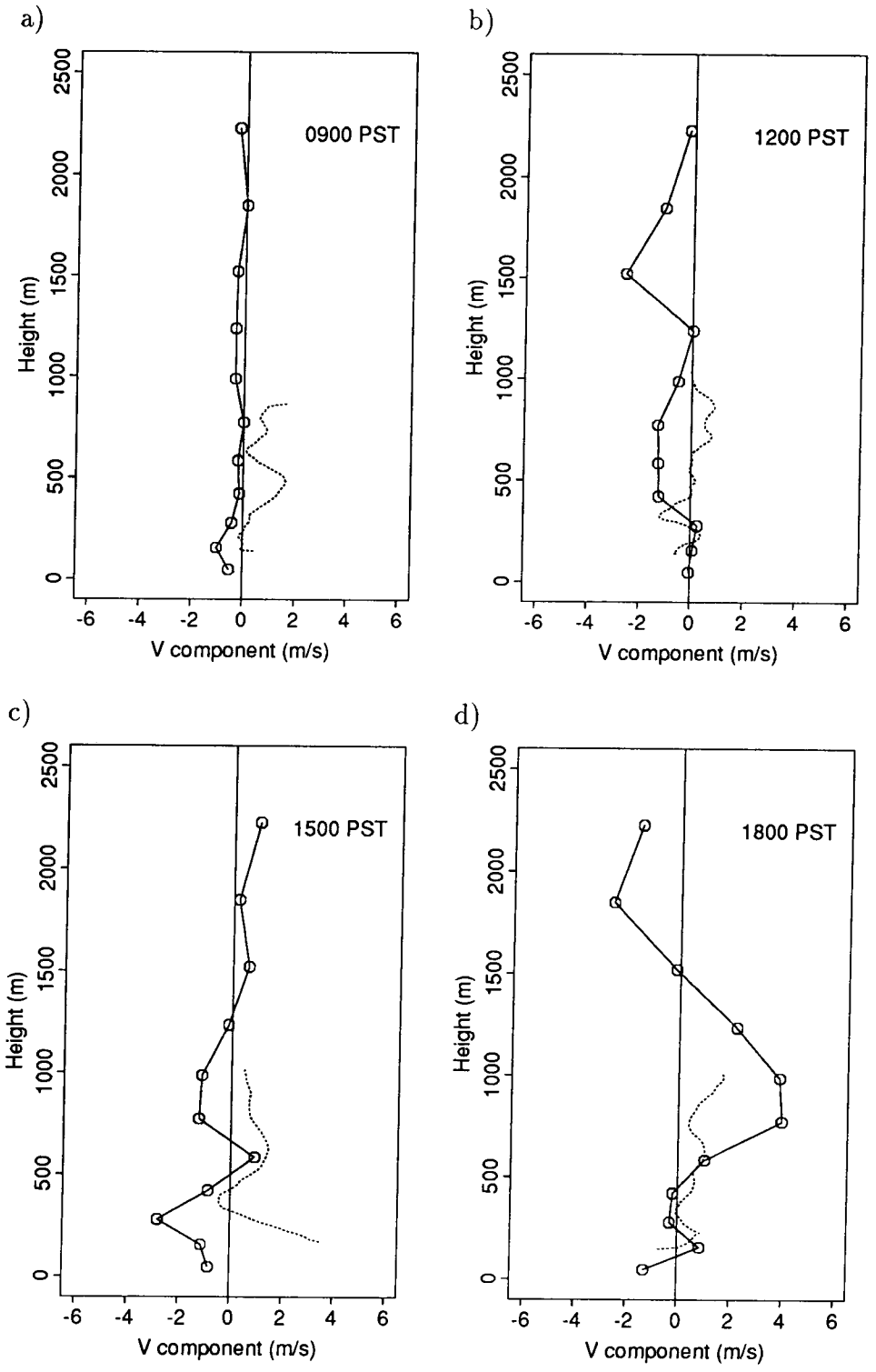

Figure 3.8: As in Fig. 3.7 but of the north-south component of wind velocity. Positive wind speed value indicates a southerly wind.

Chapter 4

Trajectory Study

This chapter studies the pollutant transport in the LFV with the RAMS mesoscale Lagrangian particle dispersion model (MLPDM). The validated meteorological fields in the LFV as described in Chapter 3 are used as input to the MLPDM model.

4.1 The RAMS Lagrangian Particle Dispersion Model

MLPDM is compatible with the RAMS meteorological model, and has been coded as a component of the RAMS visualization and analysis (VAN) postprocessing package. It is based on the MLPDM developed by McNider (1981) and uses a discrete form of the Langevin equation. Meteorological information is supplied by RAMS: these meteorological fields are used both to specify the resolved grid-scale flow field and to parameterize subgrid-scale turbulence quantities required by the MLPDM (Moran, 1992). More detailed descriptions of the formulation of this model and its application are given in Moran(1992), McNider et al. (1988) and Pielke (1984)

The particle model can be used simply as a Lagrangian analysis package to calculate parcel trajectories based on gridded wind fields from the RAMS meteorological analysis files. It can also simulate one-particle, subgrid-scale atmospheric diffusion by releasing, and then tracking, a set of passive, independent tracer particles from one or more sources. Differential advection and shear-enhanced dispersion may occur due to grid-scale resolved velocities (Moran, 1992).

The trajectory mode in the MLPDM model is used in the present study. The MLPDM

turbulence parameterization is turned off and particles are advected solely by the time-varying grid-scale RAMS wind fields. RAMS wind fields were available every hour of the simulation and linear interpolation was employed in time (the model does this automatically) to ensure a gradual transition between consecutive wind fields. The MLPDM time step was set to 15 s for calculating these 'grid-scale' trajectories.

4.2 General Pollutant Transport Investigation in the LFV

A survey of the general patterns of the pollutant transport in the LFV is first conducted. Forward trajectories of fifteen particles, released at three near-coastal sites, and at five different heights, are displayed in Figure 4.9. Their paths are remarkably different. Based on the meteorological fields depicted in Fig. 3.6, it appears that the lower three trajectories at each station are influenced by the mesoscale flows while the upper two trajectories at any of the three locations (Trajectories '4','5','9','10','14'and '15'), are driven out of the LFV mainly by easterly synoptic winds. The upper-level transport of pollutants does not appear to assist in the development of a pollutant episode and so will not be investigated further in this study. It is apparent from Fig. 4.9 that in the lower levels, not all source areas contribute to pollutant buildup in the LFV. Trajectories '11,'12','13' originating over Bellingham in the United States leave the LFV in less than 14 hours. The same is true for trajectory '8' which travelled well out of the LFV. Two other trajectories ('6' and '7') released from Tsawwassen headed southeast and up the slope of the Cascade Range, giving no indication of being returned to the valley. The three trajectories demonstrating the potential for recirculation were all from Vancouver ('1','2' and '3').

The survey of the general patterns of pollutant transport is extended to the eastern LFV. This time all particles are released 50 metres AGL at three eastern locations on

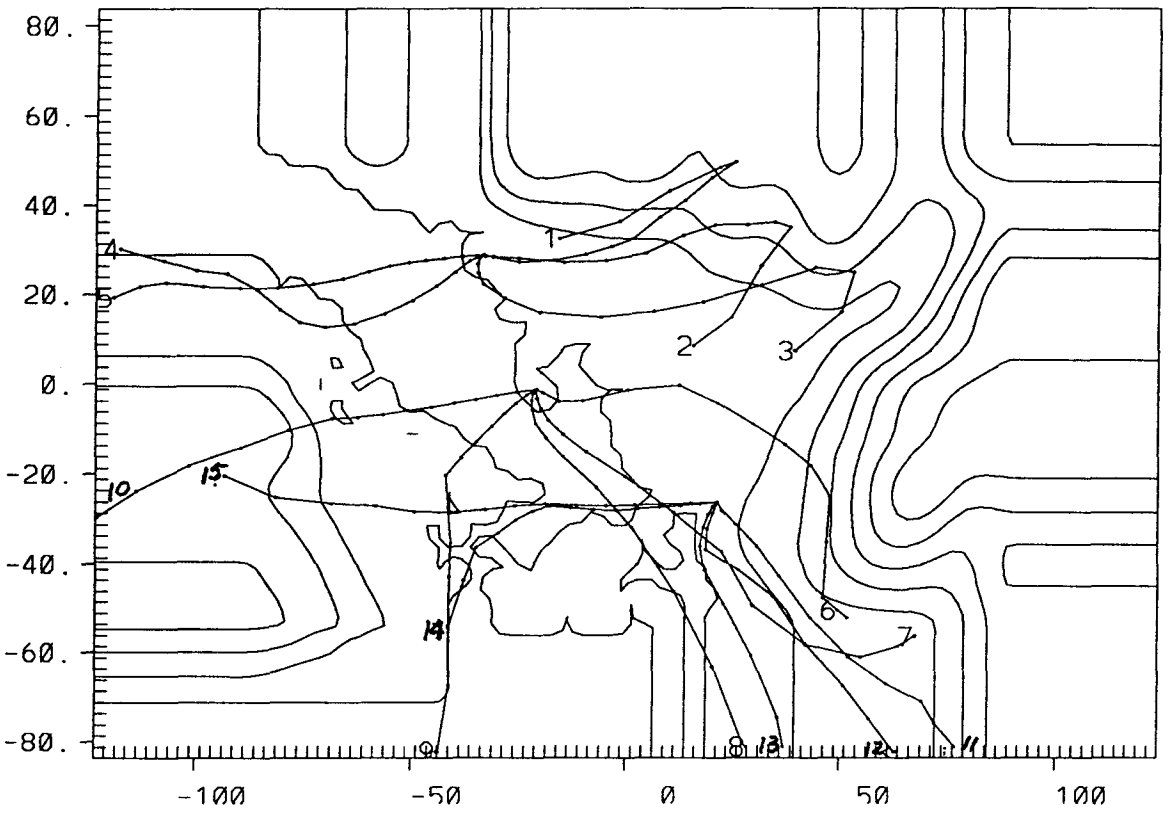

Figure 4.9: Plan view of 15 three-dimensional grid-scale trajectories at three coastal locations and at five different heights. Each trajectory starts at 0800 PST 23 August 1985 and lasts for 14 hours. Trajectory ending point labels '1','2','3','4','5' indicate the five release heights of 176m, 328m, 670m 1103m and 1673m above sea level (ASL) at one site in Vancouver. '6' to '10' sequentially are for trajectories released at Tsawwassen at heights of 130m, 335m, 660m, 1094m and 1668m ASL correspondingly. '11' to '15' are for trajectories near Bellingham, USA at heights of 206m, 407m, 733m, 1174m and 1783m ASL, respectively. The dots on the trajectories indicate the hourly trajectory positions. The background is the 200m-interval terrain contour map for the LFV and the model buffer area.

a)

b)

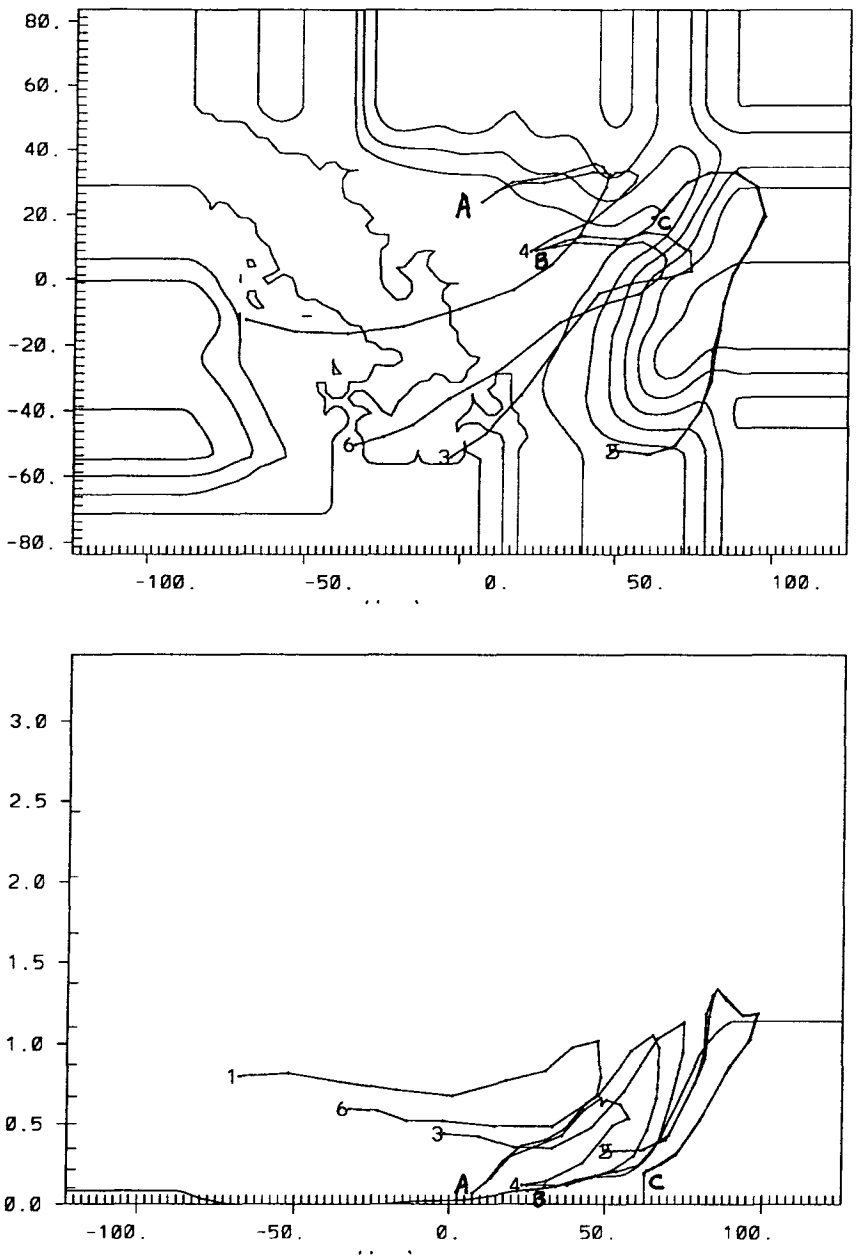

Figure 4.10: Six three-dimensional grid-scale trajectories released about 50m above the ground at three eastern locations of the LFV and at two different times. a) plan view, and b) west-east vertical slice viewed northward. 'A', 'B' and 'C' refer to releasing stations near Mission City, Abbostford and Chilliwack, respectively. '1', '2' and '3' are the corresponding trajectories released at 0800 PST 23 August 1985 while '4', '5' and '6' are for releases at 0900 PST. Each trajectory lasts for 19 hours. The dots on the trajectories indicate the hourly trajectory positions. The background on a) is the 200m-interval terrain contour map for the LFV and the model buffer area. The background on b) refers to the terrain on the slice that cuts through station "C". Labels are in units of km.

the valley floor. In addition, two releases are made at 0800 PST and 0900 PST on August 23 1985 at each station to see if there are any distinct differences resulting from release time. Figures 4.10a and b depict the resultant trajectories in a plan view and a west-east vertical slice, respectively. The three particles released at 0800 PST are similar to each other in terms of the respective trajectories and destinations after 19 hours. Each of these trajectories leaves the valley. Releases made at 0900 PST produce similar trajectory patterns, with the exception of station 'A'. Unlike trajectory '1', released at 0800 PST, which later moves with the upper-level southwestward flow, trajectory '4' is caught in downslope winds at about 1900 PST and is then driven back to the valley floor. It is possible that pollutants released around station 'A' after 0900 PST on the day of study may assist in episode buildup because they stay in the valley. On the other hand, emissions released around stations 'B' and 'C' may not be important in episode formation.

The following conclusions may be drawn from these preliminary trajectory studies.

1. High-altitude emission sources are not the major concern in episode buildup since they usually move with the synoptic wind in the upper level and eventually leave the valley.

2. Low-level emissions from the Vancouver area and its eastern neighbours are the possible areas which may contribute significantly to the episode because of their locations in relation to air flows that recirculate pollutants.

3. Other parts of the LFV do not seem to contribute as much to the elevated air pollution levels on and after the study day.

4. A different release time may result in a very different pollutant transport in the valley.

Further pollutant transport investigation will therefore focus on the pollutant emission in the Vancouver area and on the influence of the different release time on the pollutant transport.

4.3 Intensive Investigation of Pollutant Transport in the LFV

To investigate in more detail how different release times affect pollutant transport, a near-surface source in the Vancouver area will be examined first. Figures 4.11a and b give plan and elevation (northward) views of seven trajectories released at seven one-hour intervals beginning at 0800 PST. These two pictures reveal two categories of pollutant transport based on release time. If released before 1200 PST as in trajectories '1' to '4', pollutants first move up the Coastal Mountains through the combined effect of both the strong sea breeze and upslope winds. They are able to travel high enough to be captured in the sea breeze return flow and the assisting easterly geostrophic wind at about 1700 PST, and are driven westward at a height of about 800 meters above ground. On the other hand, if released on or after 1200 PST, pollutants do not seem to have enough time and momentum to climb as high along the mountain slopes before being captured by downslope winds at about 2000 PST. They are then driven back to the valley, 30 to 50km to the southeast of their origins. Emissions trapped in these parcels will likely contribute to pollution levels of the following day.

4.3.1 Dual Release-time Study of Pollutant Transport in Vancouver

Having observed a large difference in pollutant transport for different release times at a single site in Vancouver, it is of interest to see if this is true for the whole Vancouver area. In order to carry out an experiment, a rectangular area of 25km x 15km in Vancouver is selected. Emission sources are evenly distributed in a regular 5 x 3 array, with 5km

a)

b)

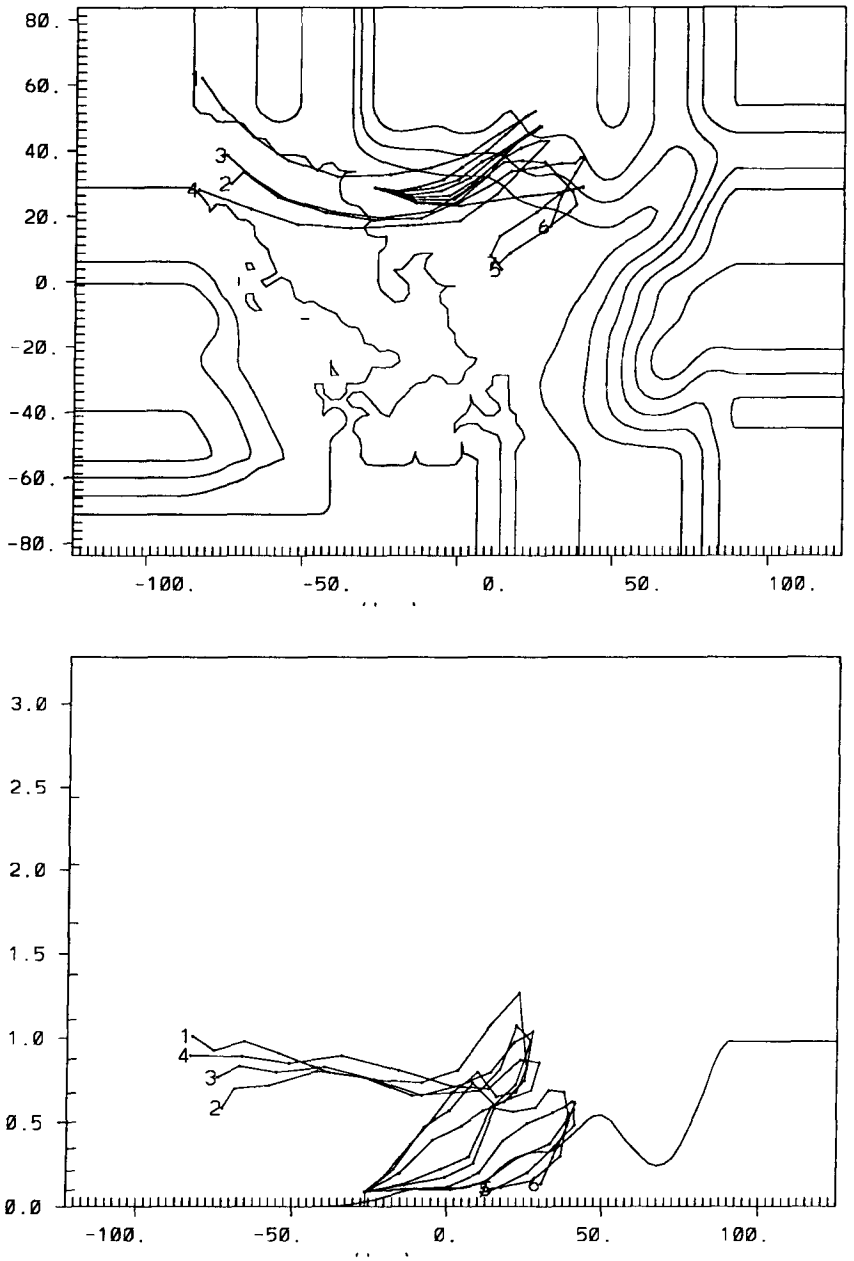

Figure 4.11: Seven three-dimensional grid-scale trajectories 50m above the ground released at one site in Vancouver at seven one-hour intervals starting from 0800 and followed for up to 19 hours. a) plan view, and b) west-east vertical slice viewed northward. Trajectory endpoint labels '1' to '7' indicate the seven release times from 0800 to 1400 PST, respectively. The dots on the trajectories indicate the hourly trajectory positions. The background on a) is the 200m-interval terrain contour map for the LFV and the model buffer area. The background on b) refers to the terrain on the slice that cuts through the release station. Labels are in units of km.

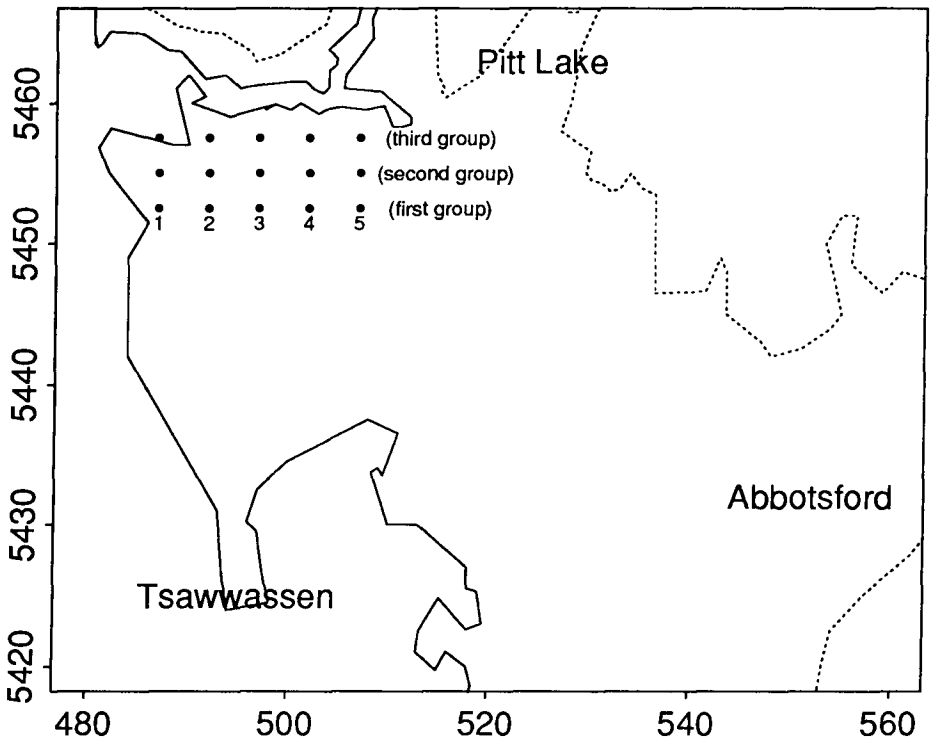

Figure 4.12: Locations of 15 emission stations in Vancouver that form three groups for the trajectory study. The solid line is the coastline, and the dashed line is the 100m terrain contour. Outer labels are in units of UTM coordinates (x 10^3).

spacing (Fig. 4.12).

Results are analyzed in terms of each east-west 5 x 1 array. The most southerly array is designated as the first group; the middle array is the second group; and the most northerly array is the third group. A paired study is conducted for each group by setting two different release times; one at 0800 PST, the other at 1200PST. In the end, inter-group comparison is made to see if there is any notable difference in the pollutant transport due to different source locations.

Figures 4.13 to 4.15 show, from three different view points the trajectories of particles released from five evenly-spaced near-surface sources of the first group at a) 0800 PST

and b) 1200 PST on 23 August 1985 and followed for 19 and 17 hours, respectively. In Figs. 4.13-4.15a, three out of five particles released at 0800 PST are later captured in the return flow of both the sea breeze and upslope winds, but do not seem to travel very far. The other two particles numbered '1' and '2', are caught in the downslope wind along Pitt Lake and are driven back down towards the valley. This means that for this study group, even pollutants released in the early morning can be recirculated in the valley. For releases at 1200 PST, all trajectories are returned to the valley floor to the east of the source region and most appear to converge in the vicinity of Abbostford.

Figures 4.16 to 4.18 depict similar information to that in Figures 4.13 to 4.15, but for trajectories of the second group. For the 0800 PST release, Figs. 4.16-4.18a show only one trajectory '3' is captured in the sea breeze return flow, but still remains in the valley. The other four trajectories are clearly returned to the valley. For the 1200 PST release case, not surprisingly, all trajectories return to regions east of Vancouver. Trajectory number '5' travels up and down Pitt Lake, suggesting that this valley might be affected by a pollutant episode.

Results from the third group are depicted in Figs. 4.19-4.21. Except for two trajectories numbered '4' and '5' from the morning release that travel southward to the Strait of Georgia, all other trajectories remain in the valley.

4.3.2 Summary of the Dual Release-Time Study

Contrary to initial investigations conducted at the beginning of the section, morning emissions may also have a substantial influence on the recirculation pollutants. Afternoon emissions appear to reduce the air quality in the LFV to a greater extent; every trajectory simulated for the study day returns to the east of Vancouver without exception, resulting in a carry-over of pollutants to the following day. The spatial locations among emissions in the Vancouver area do not affect the pollutant transport pattern significantly.

a)

b)

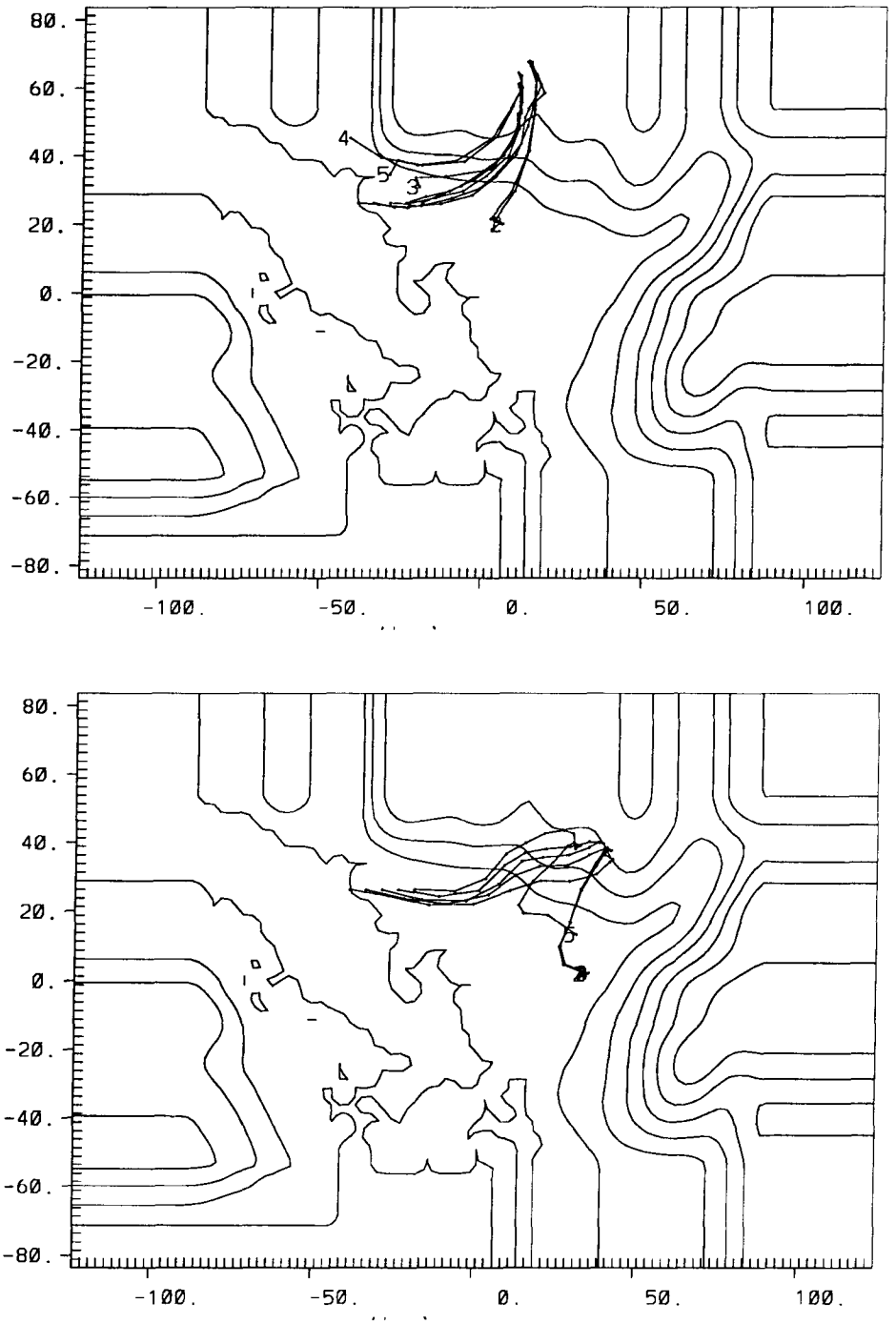

Figure 4.13: Plan view of the three-dimensional grid-scale trajectories from five sources of the first group in Vancouver. Released near the surface at a) 0800 PST, and b) 1200 PST 23 August 1985 followed up to 19 hours. Trajectory end-point labels '1' to '5' indicate the five stations spaced from west to east at 5km interval. The dots on the trajectories indicate hourly trajectory positions. The background is the 200m-interval terrain contour map for the LFV and the model buffer area. Labels are in units of km.

a)

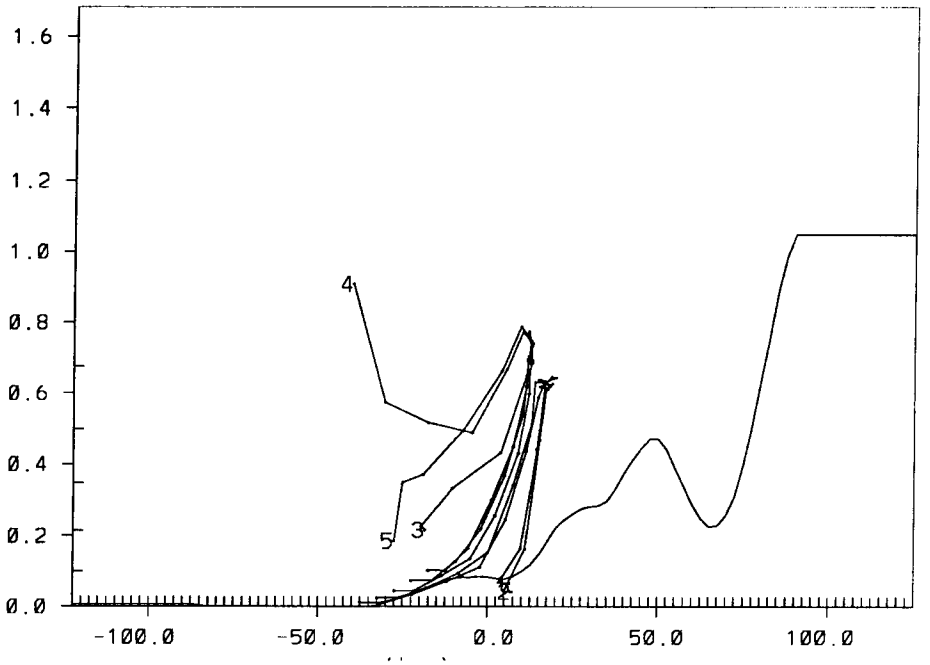

b)

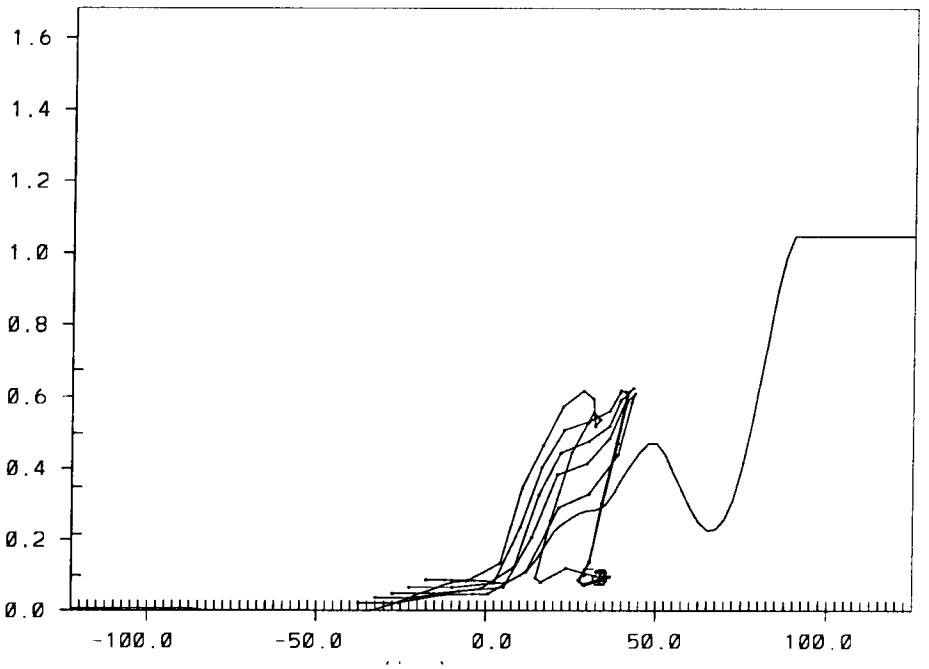

Figure 4.14: Same as Fig. 4.13 but the XZ projection that cuts through the second emission group on Fig. 4.12. Viewpoint is northward.

a)

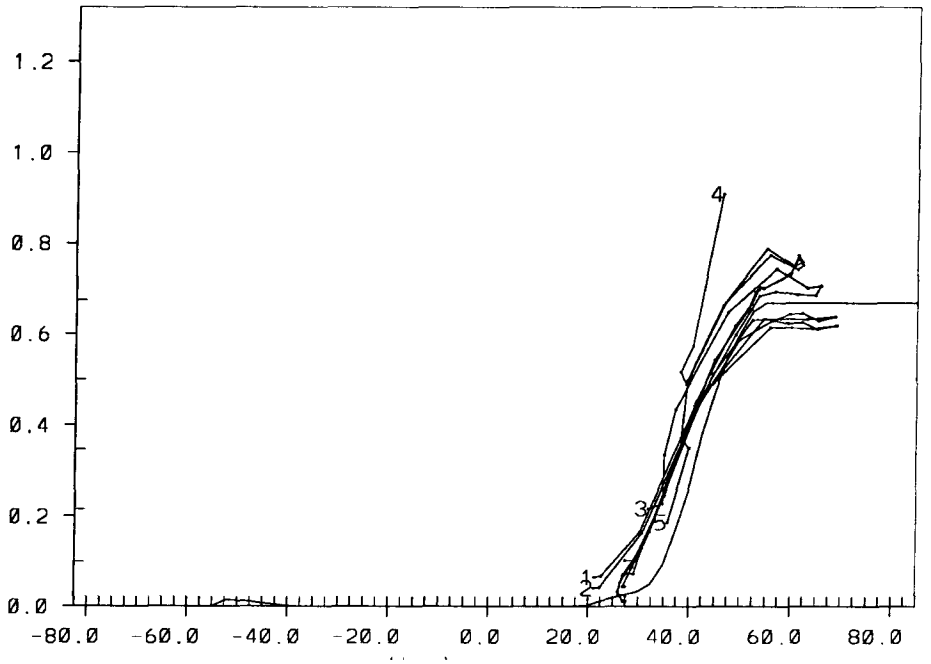

b)

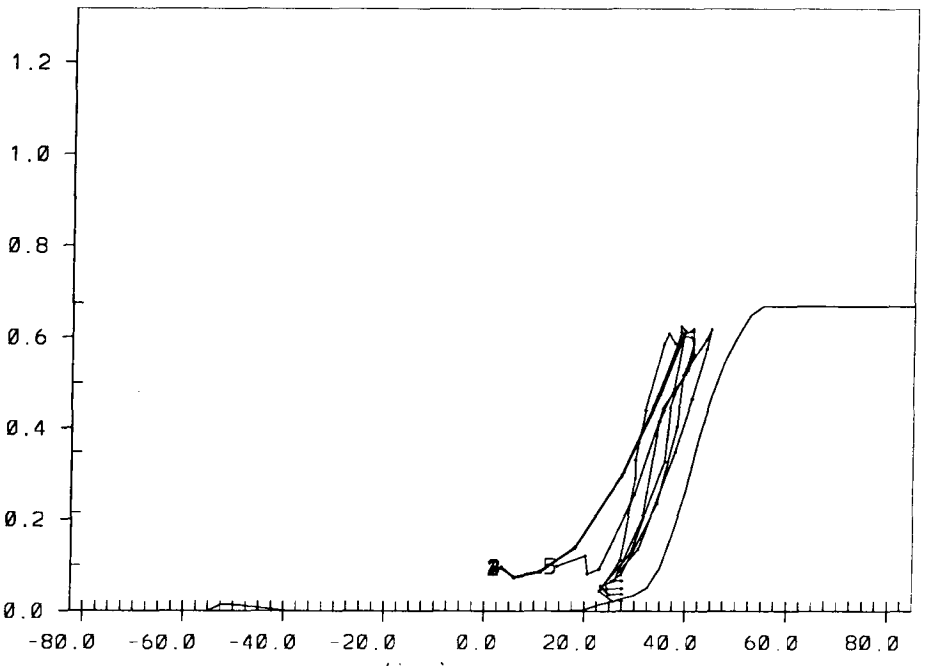

Figure 4.15: Same as Fig. 4.13 but the YZ projection that cuts through the station numbered '3' on Fig. 4.12. Viewpoint is westward.

a)

b)

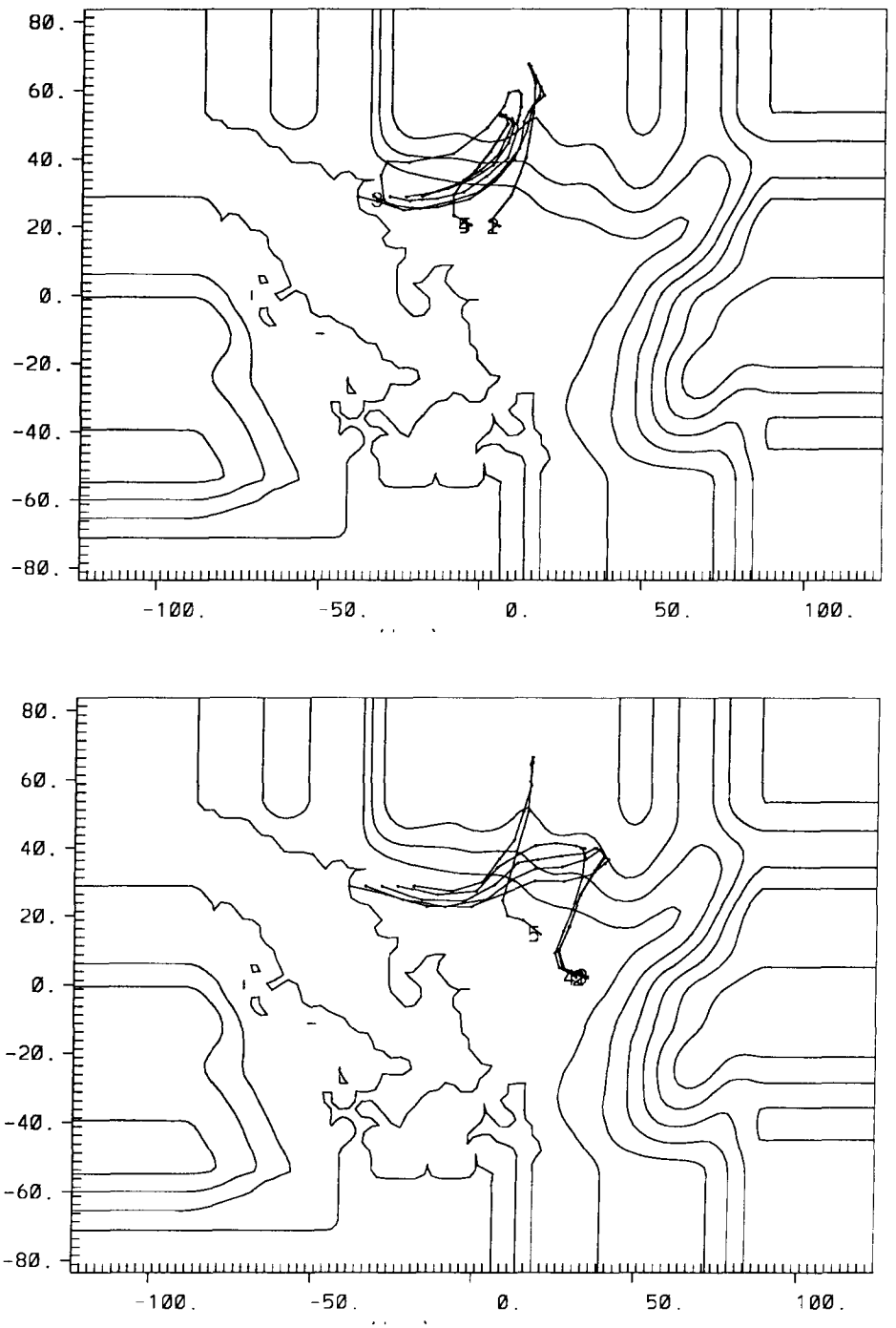

Figure 4.16: Plan view of the three-dimensional grid-scale trajectories from five sources of the second group in Vancouver. For details see caption to Fig. 4.13.

a)

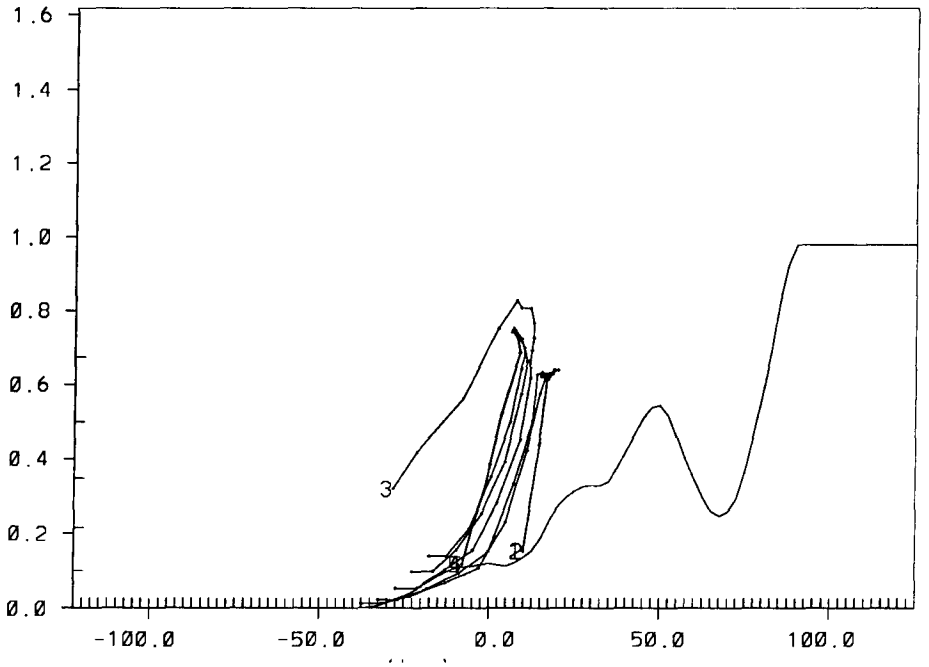

b)

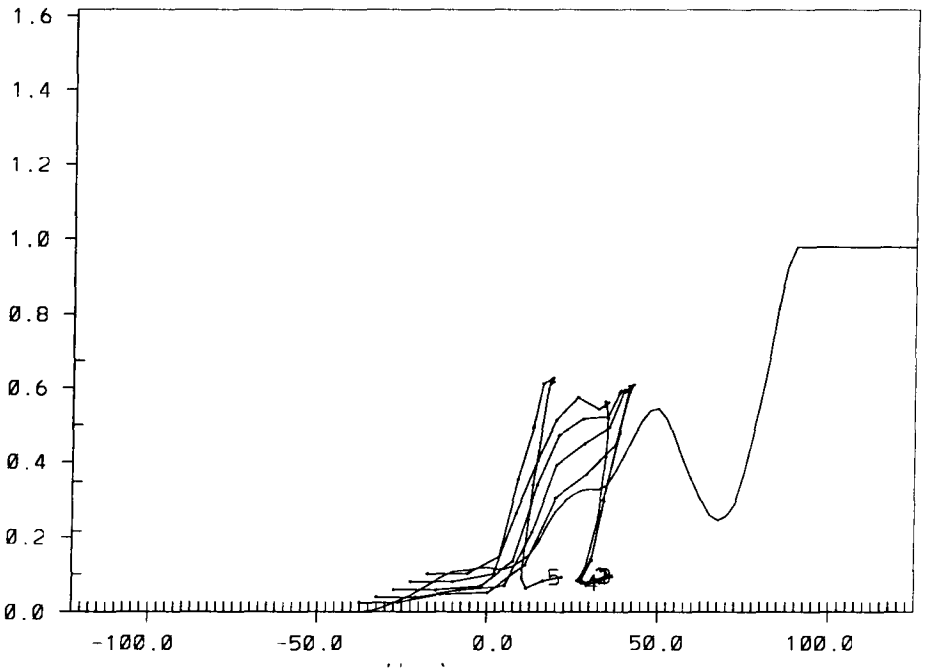

Figure 4.17: Same as Fig. 4.16 but the XZ projection that cuts through stations of this second group. Viewpoint is northward.

a)

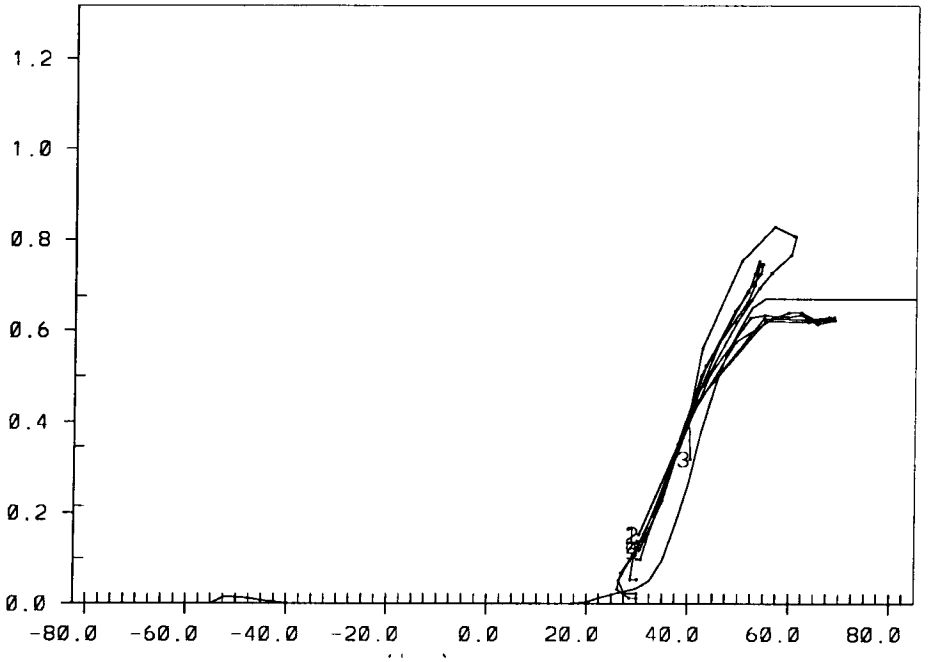

b)

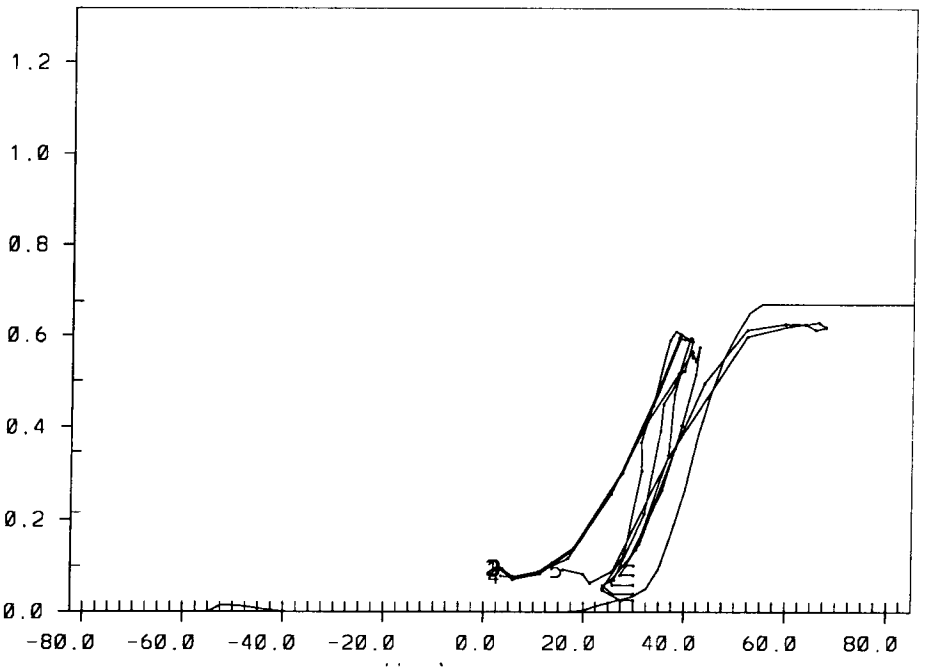

Figure 4.18: Same as Fig. 4.16 but the YZ projection that cuts through the station numbered '3' on Fig. 4.12. Viewpoint is westward.

a)

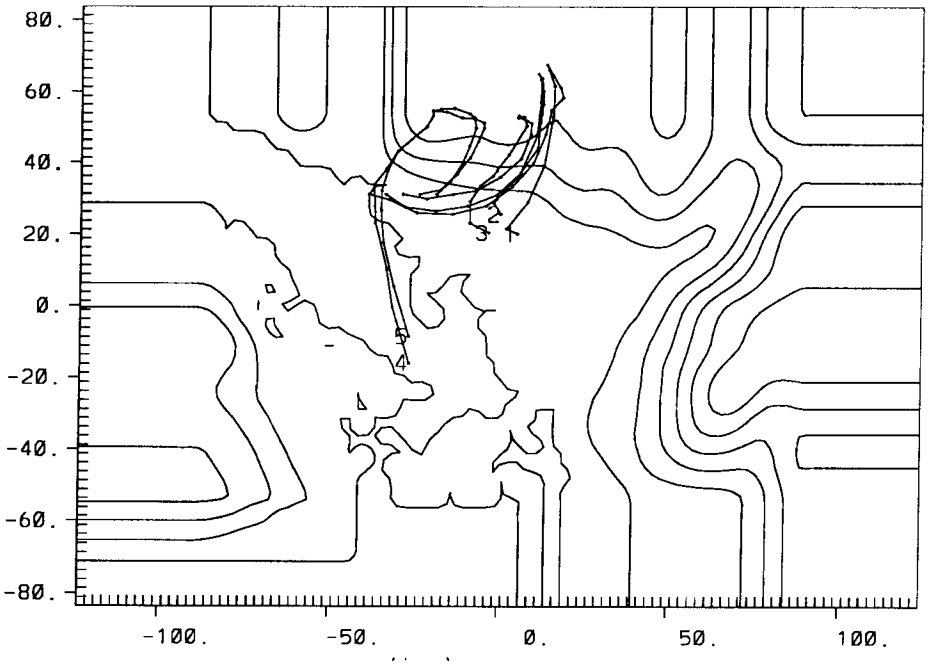

b)

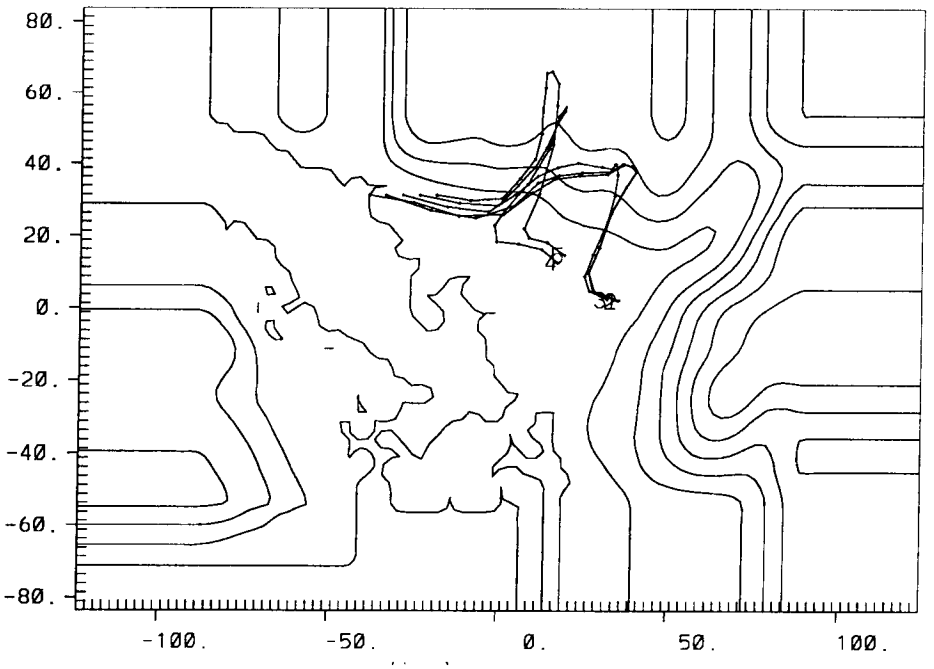

Figure 4.19: Plan view of the three-dimensional grid-scale trajectories from five sources of the third group in Vancouver. For details, see Fig. 4.13.

a)

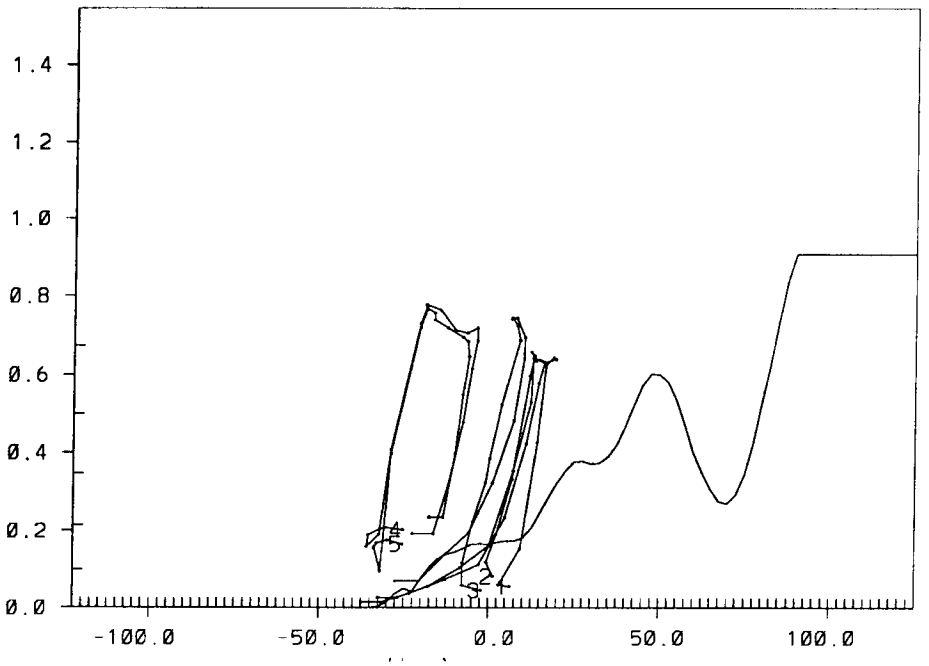

b)

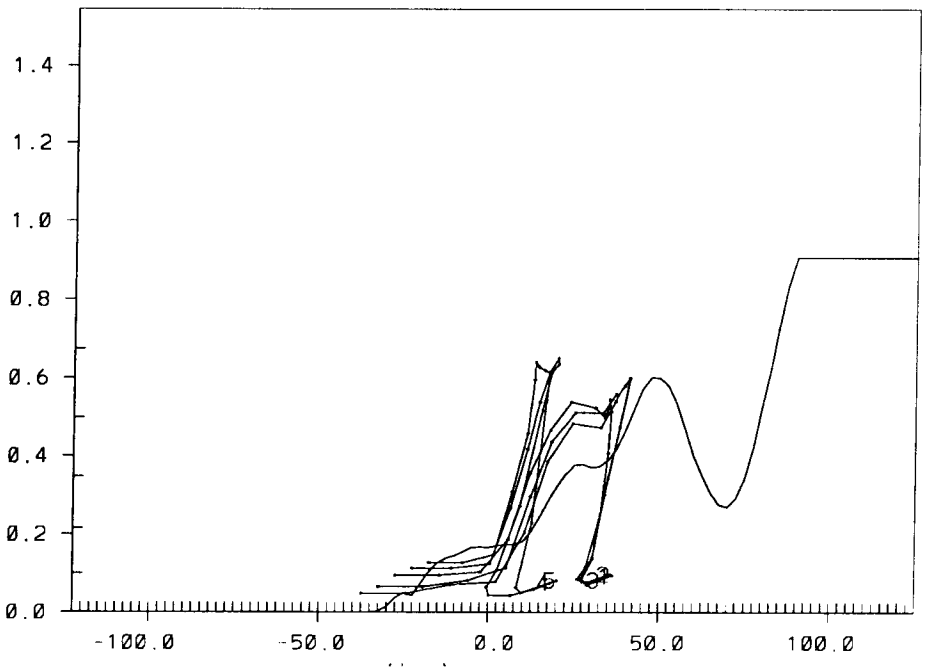

Figure 4.20: Same as Fig. 4.19 but the XZ projection that cuts through the second emission group on Fig. 4.12. Viewpoint is northward.

a)

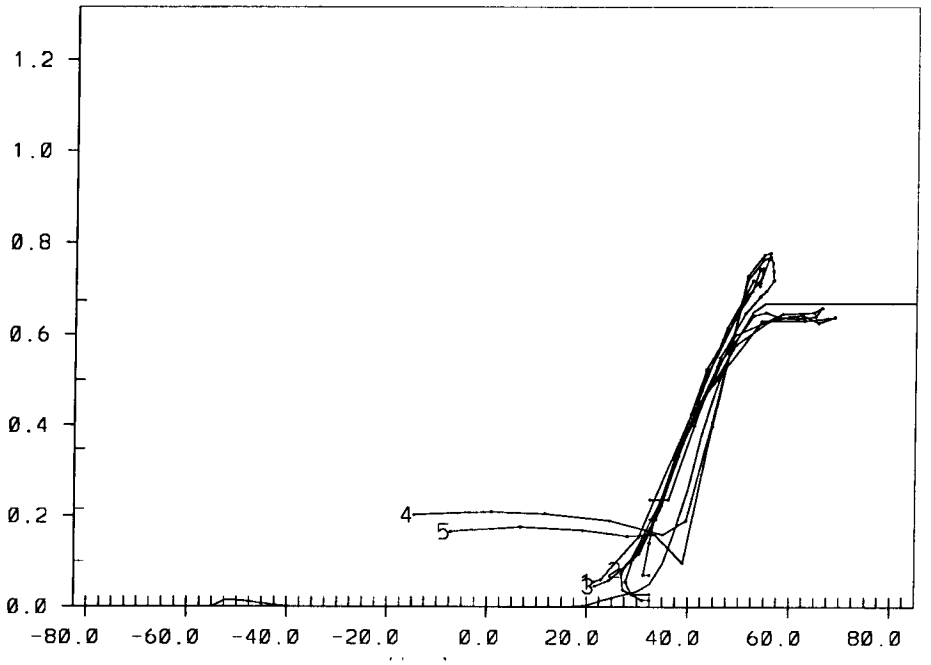

b)

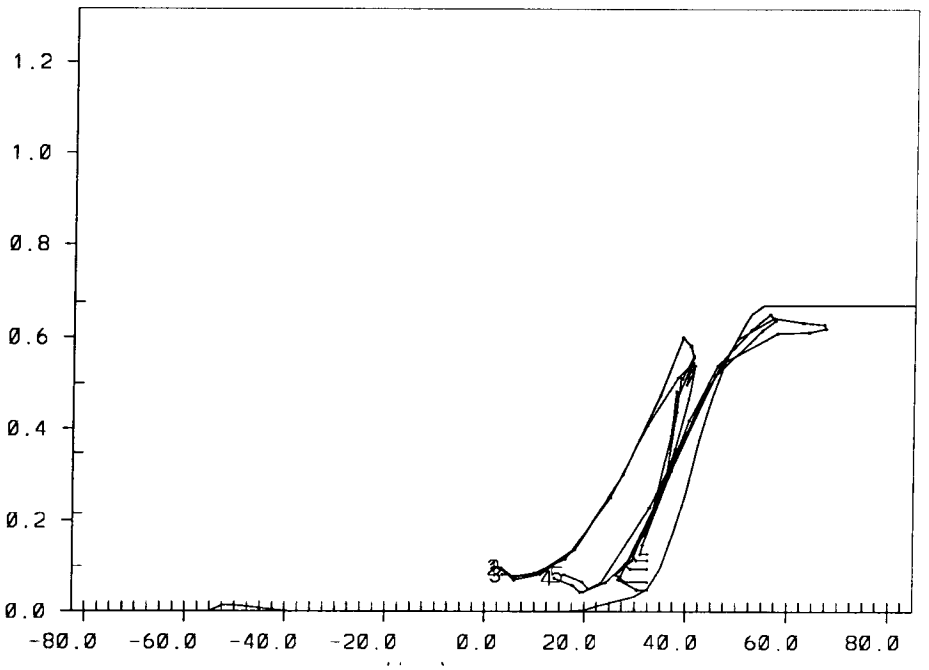

Figure 4.21: Same as Fig. 4.19 but the YZ projection that cuts through the station numbered '3' on Fig. 4.12. Viewpoint is westward.

4.4 Discussions and Conclusions

This trajectory study starts with a survey of the general patterns of the pollutant transport in the LFV by deploying six emission source stations across the LFV and by tracking particles released from these stations at different heights as well as at different times. Results show that particles at high levels do not affect much the air quality of the LFV as they usually travel with the sea breeze return flow and the easterly geostrophic winds out of the valley. Yet for emissions at lower levels, it appears that only those in Vancouver area and its easterly neighbouring area are of primary concern as they travel in a recirculating form within the valley while at most other stations, pollutants travel out of the valley. Different release time also show some importance in affecting the way particles travel. These preliminary conclusions provide us with guidelines to focus the further trajectory studies on the Vancouver area, the near-surface emissions and the different release time.

A look at trajectories produced by particles released at a near-surface emission station in Vancouver at seven different times almost makes one convinced that two distinct pollutant transport categories can be defined by release time. Morning emission releases before 1200 PST are all captured in the return flow of both sea breeze and upslope wind, and then travel westward out of the LFV. Whereas afternoon emission releases on or after 1200 PST are all driven back to the valley by downslope winds. This image is later proved not exactly true for other emission stations in the Vancouver region by three sets of dual-release-time trajectory studies conducted in the Vancouver area. While the results from the studies do confirm that particles released in the afternoon recirculate in the valley, they do not agree very well with the results from the previous study at a single point in Vancouver. Trajectories from morning particle releases mostly stay in the valley, even though there are a few which do not. It is therefore clear that even morning

emissions in Vancouver exacerbate the air pollution problem of the LFV on the study day and after.

When sea breeze flows onshore in summertime, one would intuitively suppose that pollutants emitted in Vancouver area would travel directly to the east and may very probably arrive at Chilliwack (the eastmost city in the LFV) in the afternoon. This trajectory study does not support this hypothesis. The strong upslope winds over the Coastal Mountains have deflected the pollutant paths, and the combined sea breeze and upslope flows make many pollutants released in Vancouver travel northeastward up the northern mountains in the daytime and southwestward at night by the downslope winds. Many pollutants are never able to reach Chilliwack during the day, although they may in the following day.

This trajectory study can at least partly explain the high ozone concentration pattern observed in the LFV on the study day and the following day. Ozone episode occurred on 23th and 24th of August in 1985. A maximum ozone concentration contours in the LFV on the study day is presented in Fig. 1.4. Figure 4.22 gives a snapshot of the ozone concentration contours at 1500 PST on the study day. Due to the sparsity of monitoring stations, the contour lines should be used as an approximation. The highest ozone concentration zone shown on both figures lies in a broad area from Port Moody to Chilliwack along the base of the northeast valley wall-the Coastal Mountains. Recalling those trajectory plots in this study, one would discover that the destinations of most of the trajectories which remain in the valley, are to the east of Vancouver near the northeast valley wall, coinciding with this high ozone area. This discovery suggests that the high ozone area result mainly from the emissions in the Vancouver area and pollutant recirculations induced by the mesoscale flows on the study day.

It can therefore be concluded that this trajectory study reveals the great influence of mesoscale flows on pollutant transport in the LFV. Pollutant recirculations are shown

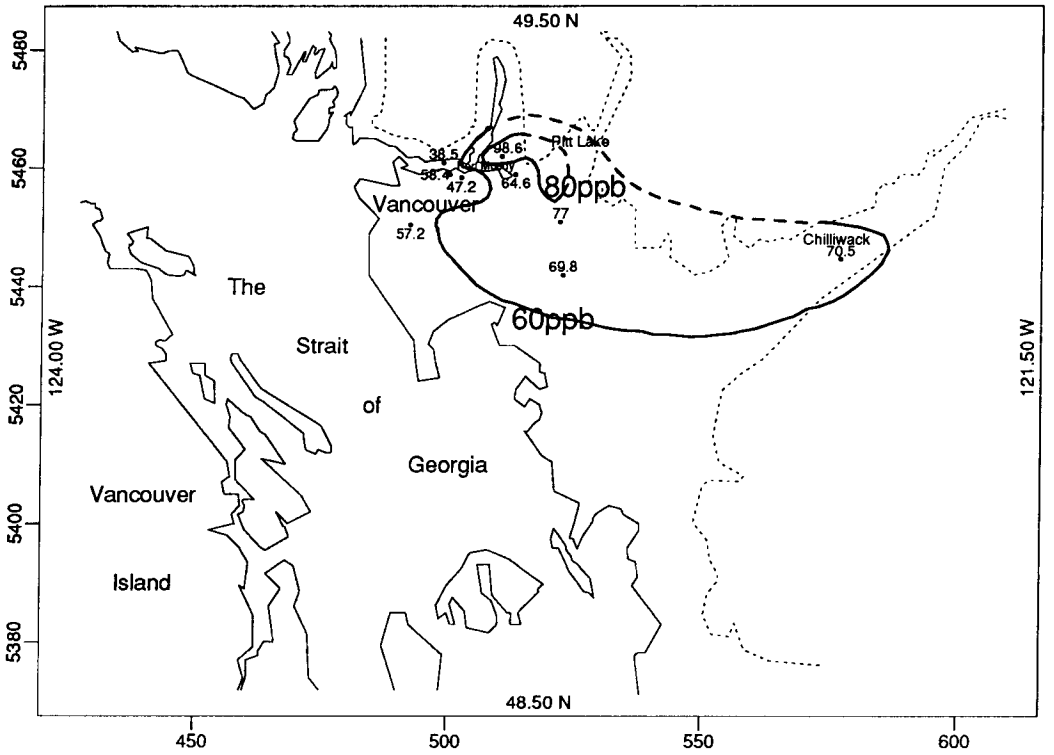

Figure 4.22: Snapshot of the ozone concentration isopleths at 1500 PST on August 23, 1985. Thick solid line refers to ozone contour, and thick dashed line refers to uncertain ozone contour. Thinner solid line is the coastline, and thinner dashed line is the 100m terrain contour indicating the edge of the valley walls. Values beside dots are the ozone concentrations at respective stations. Inner labels refer to the corresponding latitude or longitude of the boundary. Outer labels are in units of UTM coordinates (x 10^3).

clearly to occur frequently because of the specific mesoscale flows, and this pollutant recirculation may be the cause for the continued ozone episode in the following day.

4.5 Significance and Speculations

This is the first of such attempts to investigate the pollutant transport in the LFV with comprehensive model studies. Before this study, there were only speculations about how the sea breeze and other mesoscale flows would influence the pollutant transport that leads to the ozone episodes in the LFV. This study presents a series of visualizations that demonstrate the interactions among mesoscale flows and the resultant pollutant transport patterns. Pollutant recirculations are detected in various trajectories and suggest the linkage to the elevated ozone concentrations on August 23, 1985 and the following day. This study day is characterized with the slack high pressure synoptic system, northeasterly or easterly weak synoptic wind, strong solar radiation and prevalence of the thermally forced mesoscale flows. It is possible to conclude that under similar meteorological conditions to 23 August 1985, severe air pollution would likely occur as pollutants can not be easily ventilated out of the valley but recirculate within the valley. Pollutant transport for other meteorological conditions can be explored with the same methodology. Sufficient pollutant transport studies like this study under different meteorological scenarios would provide invaluable information to the air quality control and management in the LFV.

A multi-day pollutant transport study is recommended to reveal the relationship between the air pollution episode and the mesoscale meteorology. Unfortunately this study was unable to track pollutants for more than one day because the RAMS model could not provide realistic meteorological fields beyond one day. A nested-grid RAMS configuration would allow us to update the synoptic condition and may be a solution to

this problem. Future inclusion of the atmospheric diffusion process and incorporation with a photochemical model will enable the present model study to explore the temporal and spatial pollutant concentration structures in the LFV.

Appendix A

Surface Energy Balance and Surface Temperature

A.1 Introduction

In a mesoscale atmospheric model the bottom is the only boundary that has physical significance. Moreover, it is the differential gradient of the dependent variables along this surface that generates many mesoscale circulations and that has a pronounced influence on the remaining mesoscale flows. Because of the crucial importance of this boundary for the mesoscale atmospheric systems, it is essential that it be represented as accurately as possible.

Among those important variables necessary to represent this boundary, wind velocity is least difficult to determine and can be reasonably set to zero in all three directions at the roughness height. However, good determination of the surface temperature and the surface heat fluxes requires substantial effort. Various schemes for the specification of surface temperature have been presented in the past. They range widely in complexity from a sinusoidally-varying surface temperature to the "force-restore"method (Blackadar, 1976; Deardorff, 1978), to multi-level soil models (Mahrer and Pielke, 1977b; Tremback and Kessler, 1985), and to vegetation parameterizations (Deardorff, 1978; McCumber, 1980). Both multi-level soil models mentioned above have been adopted in the RAMS mesoscale model and are designed to deal with up to 12 different kinds of soil ranging from sand to peat. While these soil models are adequate to deal with bare soil energy balances, this is only a limited case since much of the world is covered with vegetation. Neglecting

the presence of vegetation incurs errors of up to a factor of two in evapotranspiration (Pielke, 1984). Moreover, even accompanied by a vegetation parameterization method as suggested by Deardorff (1978) or McCumber (1980), there are still difficulties in treating such complex land-use types as urban or suburban which contain mostly buildings and concrete with little presence of vegetation and bare soil. In view of the complexities of this problem, a different approach has been tried in this study. It relates the storage heat flux ΔQ_S directly to net radiation Q^* by an objective hysteresis model (Grimmond, Cleugh and Oke, 1991) and the latent heat flux Q_E to the difference between net radiation and the storage heat flux through the Priestley and Taylor equation (Priestley and Taylor, 1972). The remaining term, the sensible heat flux Q_H, is calculated through Louis'(1979) analytic functions. Ground surface temperature can then be solved in the surface energy balance equation through iteration. The principle of this model and the methods used are discussed in the following text.

A.2 The Model

Heat fluxes at the ground surface are related through an energy budget balance equation:

$$Q^* - Q_H - Q_E - \Delta Q_S = 0 \tag{A.1}$$

Each term in the above equation is discussed individually in the following. Finally, a scheme to compute the surface temperature will be presented.

A.2.1 The Net Radiation Flux

Mahrer and Pielke's(1977b) short- and long-wave radiation parameterization scheme for clear sky has been adopted in this study. The following is a description of this scheme.

Short-wave Radiation

The diurnal variation of the solar flux on a horizontal surface at the top of the atmosphere is computed from

$$S = S_0 \cos Z \tag{A.2}$$

with

$$\cos Z = \sin\phi \sin\delta + \cos\phi \cos\delta \cos\psi \tag{A.3}$$

where S_0 is the solar constant, Z is the solar zenith angle, ϕ is the latitude, δ is the solar declination and ψ is the solar hour angle. At the surface the solar radiation is obtained by using two empirical functions. The first empirical transmission function includes molecular scattering and absorption by permanent gases such as oxygen, ozone, and carbon dioxide. This function (denoted in the following as G), originally presented by Kondratyev (1969) and modified by Atwater and Brown (1974) to account for the forward Rayleigh scattering, is given by

$$G = 0.485 + 0.515\left[1.041 - 0.16\left(\frac{0.000949p + 0.051}{\cos Z}\right)^{1/2}\right] \tag{A.4}$$

where p is pressure in mb.

The second empirical function is from McDonald (1960) and accounts for the absorptivity of water vapour

$$a_w = 0.077\left[\frac{r(z)}{\cos Z}\right]^{0.3} \tag{A.5}$$

where r is the optical path length of water vapour above the layer z. It is given as

$$r(z) = \int_z^{top} \rho q dz \tag{A.6}$$

where ρ is the density of water vapour and q is the specific humidity. The net short-wave radiative flux at the surface is

$$R_S = \begin{cases} S_0 \cos Z(1 - A)(G - a_w) & \cos Z > 0 \\ 0 & \cos Z \leq 0 \end{cases} \tag{A.7}$$

where A is the albedo.

The solar radiative heating rates are computed for the absorption of short-wave energy by water vapour only and are given by

$$\left(\frac{\partial T}{\partial t}\right)_S = 0.0231 \frac{S_0 \cos Z}{\rho c_p} \left[\frac{r(z)}{\cos Z}\right]^{-0.7} \frac{dr}{dz} \tag{A.8}$$

Long-wave Radiation

Long-wave radiation and atmospheric heating due to its flux divergence are calculated for each time step. Carbon dioxide and water vapour are considered as emitters of long-wave radiation. The path length for water vapour(Δr_j) is computed for each layer from the surface to the top of the model by

$$\Delta r_j = -\frac{(p_{j+1} - p_j)}{g} q_j \tag{A.9}$$

The path length for $CO_2(\Delta c_j)$ is

$$\Delta c_j = -0.4148239(p_{j+1} - p_j) \tag{A.10}$$

After these increments are obtained they are summed from the first level to the ith level to give the total path length, for water vapour and carbon dioxide, respectively:

$$r_i = \sum_{j=1}^{i} \Delta r_j, \qquad c_i = \sum_{j=1}^{i} \Delta c_j \tag{A.11}$$

The emissivity for water vapour was derived from data of Kuhn (1963) and are given in Jacobs and Brown (1974).

$$\epsilon_r(i,j) = \begin{cases} 0.113 \log_{10}(1 + 12.63 r_{ij}) & \log_{10} r_{ij} < -4 \\ 0.104 \log_{10} r_{ij} + 0.440 & \log_{10} r_{ij} < -3 \\ 0.121 \log_{10} r_{ij} + 0.491 & \log_{10} r_{ij} < -1.5 \\ 0.146 \log_{10} r_{ij} + 0.527 & \log_{10} r_{ij} < -1 \\ 0.161 \log_{10} r_{ij} + 0.542 & \log_{10} r_{ij} < 0 \\ 0.136 \log_{10} r_{ij} + 0.542 & \log_{10} r_{ij} > 0 \end{cases} \tag{A.12}$$

where $r_{ij} = |r_i - r_j|$ is the optical path length between the ith and jth levels. Kondratyev's(1969) emissivity function for carbon dioxide in the form

$$\epsilon_{co2}(i,j) = 0.185\left[1 - \exp(-0.3919|c_i - c_j|^{0.4})\right] \tag{A.13}$$

is used, and finally the emissivity at each level is given by

$$\epsilon(i,j) = \epsilon_r(i,j) + \epsilon_{co2}(i,j) \tag{A.14}$$

Using the above emissivity functions we have for the downward and upward fluxes at a level N

$$R_d(N) = \sum_{j=N}^{top-1} \frac{\sigma}{2}(T_{j+1}^4 + T_j^4)\left[\epsilon(N,j+1) - \epsilon(N,j)\right] + \sigma T_{top}^4(1 - \epsilon(N,top)) \tag{A.15}$$

and

$$R_u(N) = \sum_{j=1}^{N-1} \frac{\sigma}{2}(T_{j+1}^4 + T_j^4)\left[\epsilon(N,j) - \epsilon(N,j+1)\right] + \sigma T_G^4(1 - \epsilon(N,0)) \tag{A.16}$$

where T_G is the ground surface temperature in degrees Kelvin.

When $N = 1$, $R_d(1)$ is the downward long-wave flux to the surface R_L. The radiative cooling at each layer is computed from

$$(\frac{\partial T}{\partial t})_N = \frac{1}{\rho c_p}\frac{(R_u(N+1) - R_u(N) + R_d(N) - R_d(N+1))}{z(N+1) - z(N)} \tag{A.17}$$

Terrain Effects on Radiation

Kondratyev (1969) gives the following expression for the solar radiation on a slant surface

$$S_{sl} = S_0 \cos i \tag{A.18}$$

where i is the angle of incidence of solar rays on the inclined surface, and

$$\cos i = \cos\alpha\cos Z + \sin\alpha\sin Z\cos(\beta - \eta). \tag{A.19}$$

Here Z is the zenith angle, α is the slope angle, β and η are solar and slope azimuths. The latter three are defined as:

$$\alpha = \tan^{-1}\left[(\frac{\partial z_G}{\partial x})^2 + (\frac{\partial z_G}{\partial y})^2\right] \tag{A.20}$$

$$\beta = \sin^{-1}\left[\frac{\cos\delta \sin\psi}{\sin Z}\right] \tag{A.21}$$

$$\eta = \tan^{-1}\left[\frac{\partial z_G}{\partial y}/\frac{\partial z_G}{\partial x}\right] - \frac{\pi}{2} \tag{A.22}$$

where z_G is the ground height. For a slant surface the solar and infrared radiation will be modified

$$R_S|_{sl} = R_S\frac{\cos i}{\cos Z} \tag{A.23}$$

and

$$R_L|_{sl} = R_L \cos\alpha \tag{A.24}$$

The net all-wave radiation Q^* on the surface is therefore equal to:

$$Q^* = R_S|_{sl} + R_L|_{sl} - \sigma T_G^4 \tag{A.25}$$

A.2.2 The Storage Heat Flux

Since the surface in the real world is not usually well defined and homogeneous at the spatial scales of interest, it is much useful to introduce the concept of a surface volume. The top of the volume is to just above roof/tree/vegetation level and the base to a depth in the ground where no net vertical heat transport takes place over the period of interest (Oke and Cleugh, 1987). Then the storage heat flux (ΔQ_S) is defined to account for the latent and sensible heat changes in, as well as the heat conduction into or out of, a surface volume.

This study adopts an objective hysteresis storage heat flux model developed by Grimmond, Cleugh and Oke (1991) to parameterize heat storage change in terms of the surface

all-wave radiation which forces the energetics of the system, and the nature of the surface cover. This model is essentially empirical but its form has both theoretical and physical support. The performance of the model has been validated against suburban data (Grimmond, Cleugh and Oke, 1991; Roth, 1991; Roth and Oke, 1993). It was originally developed for a study of urban environments. Since an objective method to characterize the surface is used, it can also be applied generally to other areas.

The Hysteresis Storage Heat Flux Model

For a certain surface material, the storage heat flux can be related to the net all-wave radiation Q^* (Camuffo and Bernardi, 1982) as:

$$\Delta Q_S = a_1 Q^* + a_2 \frac{\partial Q^*}{\partial t} + a_3 \tag{A.26}$$

where a_1, a_2, a_3 are coefficients for the surface with the units of dimensionless, hour and Wm^{-2}, respectively. The second term involving $\frac{\partial Q^*}{\partial t}$ describes the rate and direction of change of Q^*, and is included to reproduce the observed out-of-phase relationship between ΔQ_S and Q^* (the peak of ΔQ_S precedes that of Q^* by one or more hours). To represent the storage heat flux for any specific land-use type, which may consist of several different surface materials, Grimmond, Cleugh and Oke (1991) developed a composite equation which weights the role of each surface according to their plan coverage in the area under study, so that:

$$\Delta Q_S = \sum_{i=1}^{n} \varphi_i \{a_{1i} Q^* + a_{2i} \frac{\partial Q^*}{\partial t} + a_{3i}\} \tag{A.27}$$

A simplified form of this equation could be written as:

$$\Delta Q_S = C_1 Q^* + C_2 \frac{\partial Q^*}{\partial t} + C_3 \tag{A.28}$$

where φ_i is the fraction of the area covered by the ith surface. a_{1i}, a_{2i}, a_{3i} are coefficients for the ith surface, and C_1, C_2, C_3 refer to the composite coefficients for the study area

Table A.1: Summary of Coefficients for Some Surface Materials.

Land cover	Author	Regression coefficients		
		a_1	a_2(h)	$a_3(Wm^{-2})$
Greenspace/Open				
Short grass	Doll *et al.*(1985)	0.32	0.54	-27.4
Grassland	Clarke *et al.*(1971)	0.33	0.03	-11.0
Bare soil	Novak(1981)	0.38	0.56	-27.3
Rooftop				
Vancouver	Yap(1973)	0.17	0.10	-17.0
Uppsala	Taesler(1980)	0.44	0.57	-28.9
Paved				
Concrete	Doll *et al.*(1985)	0.81	0.48	-79.9
Asphalt	Narita *et al.*(1984)	0.36	0.23	-19.3
Canyon				
N-S canyon	Nunez(1974)	0.32	0.01	-27.7
Forest				
Mixed forest	McCaughey(1985)	0.11	0.11	-12.3

(grid box in RAMS). By using this equation, ΔQ_S in any distinct area can be calculated as long as an inventory of the dimensions of any buildings, the distribution of surface materials and other information necessary to characterize the study area is provided. The coefficients for several surface materials representative of the present study area are available from various observations, including observations made in the Vancouver area. However there are some surface materials representative of rural and farmland areas of the LFV that are not adequately characterized by existing observations. Under these circumstances, combinations of the known coefficients for other surface materials are used. Here, consideration is given to materials having similar characteristics such as moisture content. These approximations are used when assigning coefficients for greenspace in rural areas and for agricultual areas.

Coefficients resulting from observational studies for several surface materials are listed

Table A.2: Summary of Coefficients for Various Land-use Types.

Land-use type	Land cover	Weighting factor	Regression coefficients		
			a_1	a_2(h)	$a_3(Wm^{-2})$
Urban	Rooftop	0.20	0.17	0.10	-17.0
	Paved	0.20	0.58	0.35	-49.6
	Canyon	0.60	0.32	0.01	-27.7
	Composite Coefficients		**0.34**	**0.10**	**-29.9**
Suburban	Greenspace	0.33	0.32	0.37	-29.2
	Rooftop	0.13	0.17	0.10	-17.0
	Paved	0.11	0.58	0.35	-49.6
	Canyon	0.43	0.32	0.01	-27.7
	Composite Coefficients		**0.33**	**0.18**	**-29.2**
Rural	Vegetation	0.90	0.34	0.38	-21.9
	Rooftop	0.05	0.17	0.10	-17.0
	Paved	0.05	0.58	0.35	-49.6
	Composite Coefficients		**0.35**	**0.36**	**-23.0**
Agricultural	Vegetation	1.00	0.15	0.03	-11.0
	Composite Coefficients		**0.15**	**0.03**	**-11.0**
Forest	Forest	1.00	0.11	0.11	-12.3
	Composite Coefficients		**0.11**	**0.11**	**-12.3**

in Table A.1. Table A.2 contains information about the weighting factors (percentage of specific surface type in an area) and coefficients of the five land-use types defined for the LFV in summertime. The assignment of the weighting factors in each land-use type is made possible with the aid of field surveys and aerial photographs. Experts were consulted before values of the coefficients for each land-use type are finally set.

In all cases, coefficients for paved surfaces have been taken as averages of concrete and asphalt. Greenspace values for suburban land-use takes its coefficients from the average of dry and irrigated grass lawn since this may be more representative than using only one moisture status. For rural areas, coefficients are estimated as averages of short grass, grassland and bare soil (Grimmond 1992, personal communication). In agricultural areas, only coefficients from moist grassland are applied since the condition of the grass is very

close to that in the agricultural area.

A.2.3 The Latent Heat Flux

Priestley and Taylor (1972) argued that for a wet area at the scale of the grids used in computer solutions of numerical weather-forcasting models, radiant energy receipt must dominate over advective effects in controlling evaporation. Following this idea, they developed an equation for evaporation from wet regions as

$$Q_E = \alpha \frac{s}{s+\gamma}(Q^* - \Delta Q_S) \tag{A.29}$$

where Q_E is the latent heat flux and α is an empirical coefficient. A value for α of 1.26 was found to fit well the data from several sources. s is the slope of the saturation specific humidity curve, $s = dq^*/dT$ (K^{-1}). $\gamma = c_p/\lambda \cong 0.0004$ $(g_{water}/g_{air})K^{-1}$ is the psychrometric constant. λ (Jkg^{-1}) is the latent heat of vaporization of water and $c_p = 1004$ $Jkg^{-1}K^{-1}$ is the specific heat of dry air at constant pressure. dq^*/dT is given by the *Clausius-Clapeyron* equation:

$$\frac{dq^*}{dT} = 0.622\frac{\lambda q^*}{RT^2} \tag{A.30}$$

where

$$q^* = 0.622\frac{e^*}{P} \tag{A.31}$$

$$e^* = (0.6112kPa)\exp\left(\frac{17.67(T-273.16)}{T-29.66}\right) \tag{A.32}$$

and q^* is the saturation specific humidity in $kgkg^{-1}$. Temperature T is in degrees Kelvin. P and e^*, both expressed in terms of kPa, are the atmospheric pressure and saturation vapour pressure, respectively. R is the gas constant for dry air, and is equal to 287.04 $m^2s^{-2}K^{-1}$.

Although the Priestley-Taylor equation was developed mainly to deal with evaporation in a well-watered region, it may be used more generally to ascribe evaporation

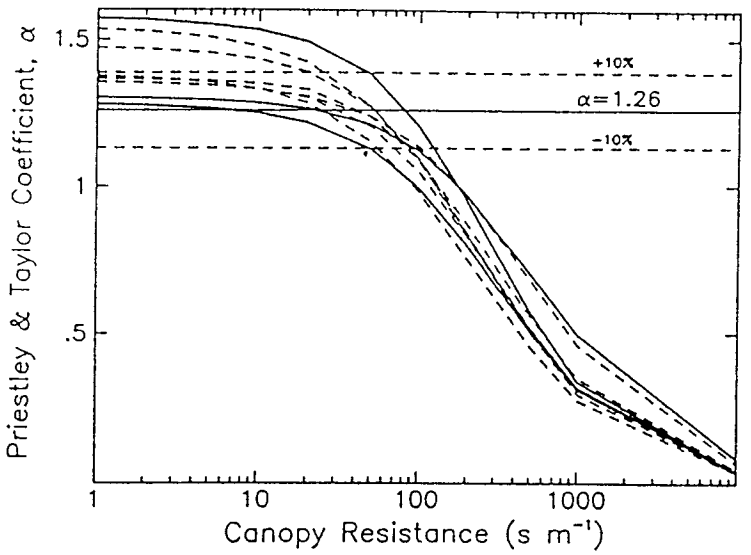

Figure A.1: Priestley-Taylor coefficient α calculated for a range of canopy resistance for the Cabauw data set (from McNaughton and Spriggs 1987).

even in water-constrained areas if the Priestley-Taylor coefficient (hereafter referred to as the P&T coefficient) α can be adjusted to reflect the evaporative condition of the area (de Bruin, 1983; de Bruin and Keijamn, 1979; McNaughton and Spriggs, 1987). McNaughton and Spriggs (1987) found from experiments at Cabauw that estimation of α may be made from canopy or surface resistance alone. Figure A.1 shows the relationship between the calculated P&T coefficient α and canopy resistance. Canopy resistance is a parameterized variable accounting for water loss of an area treating it as if it were a single hypothetical leaf with characteristics related to diurnal and seasonal variations.

Based on this idea, with the aid of experience and some experimental data of canopy resistance, a set of summertime P&T coefficients are assigned to five different land-use types in the LFV in Table A.3. These values are only appropriate to the conditions applying on the day in question.

The effect of advection have also been considered. Uncertainties are inevitably involved in the process. The assigned P&T coefficients are considered reasonable to reflect

Table A.3: Summary of P&T Coefficient for Each Land-use Type.

Land-use Type	Urban	Suburban	Rural	Agricultural	Forest
P&T Coef.	0.2	0.8	1.0	1.26	1.0

evaporation conditions for different land-uses in summertime. This difference in P&T coefficients is necessary to induce a non-uniform temperature and wind field across the Lower Fraser Valley.

A.2.4 The Sensible Heat Flux

The sensible heat flux is calculated through an independent channel rather than as a residual in the surface energy balance. The scheme of Louis' (1979) analytic functions method is adopted. It is based on Monin and Obukhov (1954) similarity theory and makes use of Businger's functions for the flux-profile relationships in the surface layer. The sensible heat flux may be written: $Q_H = -\rho c_p u_* \theta_*$, where u_* and θ_* are the scaling velocity (or friction velocity) and temperature, respectively. If the roughness length z_0, potential temperature θ and wind speed u above the surface, and temperature difference between surface and air $\Delta\theta$ are provided, u_* and θ_* can be found through the flux-profile relationships. The following is what Louis conceived to get u_* and θ_*. From the flux-profile relationships:

$$u_*{}^2 = a^2 u^2 F_m(\frac{z}{z_0}, R_{iB}) \tag{A.33}$$

$$u_* \theta_* = 1.35 a^2 u \Delta\theta F_h(\frac{z}{z_0}, R_{iB}) \tag{A.34}$$

where R_{iB} is the bulk Richardson number.

$$a^2 = \kappa^2/(lnz/z_0)^2 \tag{A.35}$$

$$R_{iB} = \frac{gz\Delta\theta}{\theta u^2} \tag{A.36}$$

and κ is von Karman's constant (0.35). g is the gravitational acceleration (9.8 ms^{-2}). Having the numerically computed curves for the functions a^2F_m and a^2F_h, Louis used analytical formulae to fit these curves:

For unstable cases ($R_{iB} < 0$)

$$F_m = 1 - \frac{9.4R_{iB}}{1 + c_m|R_{iB}|^{0.5}} \tag{A.37}$$

$$F_h = 1 - \frac{9.4R_{iB}}{1 + c_h|R_{iB}|^{0.5}} \tag{A.38}$$

where

$$c_m = 69.56a^2(\frac{z}{z_0})^{1/2} \tag{A.39}$$

$$c_h = 49.82a^2(\frac{z}{z_0})^{1/2} \tag{A.40}$$

For stable cases ($R_{iB} > 0$)

$$F_m = F_h = 1/(1 + 4.7R_{iB})^2 \tag{A.41}$$

In this manner, both vertical eddy fluxes of momentum $\overline{w'u'} = u_*^2$ and sensible heat $\overline{w'\theta'} = -u_*\theta_*$ could be obtained without going through complicated iterative computations.

A.3 Numerical Procedures

It must be appreciated that until an appropriate surface temperature at one time step is decided, all terms in the surface energy balance equation remain unsettled. The surface temperature is computed by a Newton-Raphson iterative solution to the surface energy balance. The computational procedure is as follows.

1. Compute Q^* and Q_H using the surface temperature of the last time step, and then compute ΔQ_S and Q_E.

2. Let $F(T_G)$ be equal to the sum of the terms on the left side of equation A.1 and get $F(T_G)$ value. If $|F(T_G)|$ is not less than some small value (set to 10^{-3}), then apply the Newton-Raphson iteration process in the form

$$T_G^{N+1} = T_G^N - F(T_G)/F'(T_G) \tag{A.42}$$

Here $F'(T_G)$ is the derivative of $F(T_G)$ with respect to T_G. The four heat flux terms are then recalculated.

3. Repeat step 2, until the desired accuracy of $F(T_G)$ has been reached. This ensures that the energy balance equation (A.1) is closed. The final correct heat fluxes for the current time step can then be calculated with the last iterated surface temperature T_G.

A.4 Energy Balance and Surface Temperature at Night

At night, surfaces exhibit very different behaviour to that in the daytime in terms of the partitioning of the net radiation into the three flux terms. In light wind cases, the sensible and latent heat fluxes usually become insignificant energy sinks or sources so the storage heat flux tends to approximately balance the loss of net radiation from the surface. In view of this, the preceding model for the daytime is not applicable to predict the nighttime surface temperature and to determine the surface layer fluxes. To overcome this problem, a formula given theoretically by Brunt (1941) to calculate the nighttime surface temperature is adopted. The Brunt formula relates the temperature deviation from sunset to the half power function of time, the net radiation at sunset and the thermal admittance for the studied surface.

$$\Delta T_{t-s} = -\frac{2}{\pi^{1/2}} \frac{Q^*}{\mu} t^{1/2} \tag{A.43}$$

Where Q^* is from the value at sunset, ΔT_{t-s} is the decrease of temperature in time t from sunset and μ is the thermal admittance. This relation has proved to be very successful in rural areas with an estimated thermal admittance of about 1600 $Wm^{-2}s^{1/2}K^{-1}$ (Oke and Maxwell, 1975). It is not as successful for urban areas, where a linear relation seems to be more appropriate (Oke and Maxwell, 1975). Since the nocturnal stable atmosphere does not respond to the surface as sensitively as in the daytime, it is justified to use this function in urban and suburban cases as an approximation. From studies of the thermal admittance for individual materials (Oke, 1981), thermal admittances as high as 2100 and 1700 $Wm^{-2}s^{1/2}K^{-1}$ are assigned to urban and suburban land-use types respectively in this study, while 1600 $Wm^{-2}s^{1/2}K^{-1}$ is used for other land-use types.

After surface temperature is computed, Louis' flux-profile function is used to calculate the necessary surface fluxes u_*, θ_* and R_* (scaling specific humidity), thus completing the surface heat budget and surface layer parameterization.

A.5 Model Evaluation

The applicability of this daytime prognostic-empirical energy balance model to the present study is evaluated by comparing the predicted surface energy fluxes with observations. On the day of interest, hourly mean net radiation and sensible heat fluxes were measured at a suburban site in Vancouver during daylight hours. Storage heat fluxes and latent heat fluxes were subsequently obtained through parameterization in the objective hysteresis storage model and as a residual, respectively. The same four fluxes have also been extracted from the RAMS model output.

Figures A.2a-d depict the time series of these four fluxes at Sunset on August 23 1985 for both modelled results and observed data. The modelled net radiation in Fig. A.2a overestimates the observed values by up to 75 Wm^{-2}. This consequently results in a

slight overestimation of the other modelled heat fluxes. However the trends of Q^*, ΔQ_S and Q_H are simulated quite successfully. Q_E is predicted well in the morning, before 1000 PST, but the abrupt decrease in the flux in the afternoon is not well-simulated, presumably because of the model's poor representation of the mechanism that gives rise to the observed trend. Comparing Figs. A.2c and d, it can be seen that the continuous increase in the observed sensible heat fluxes Q_H in the afternoon may be responsible for the observed afternoon decrease in Q_E.

One of the major purposes of this energy balance model is to predict the surface temperature. Therefore, it is important to prove that the model does provide a reasonable surface temperature field. Unfortunately there is a paucity of temperature data available for the day of interest. Instead a satellite thermal image [1] covering mainly the Greater Vancouver area at 13.56 Local Standard Time (LST) [2] on August 16 1985 was used to obtain what are likely to be similar surface temperature patterns, which were then compared with modelled results. The area of satellite coverage and the satellite surface temperature picture are shown in Figs. A.3a and b, respectively. August 16 was a cloudless summer day. The satellite picture, from Roth, Oke and Emery (1989), was first scanned and later converted back to temperature data. Figure A.4a is the surface temperature contour map of the satellite image and Fig. A.4b is the contour map of the modelled surface temperature at 1400 PST on August 23 1985. Although a direct comparison of the exact magnitudes between these two fields is not appropriate, similarity of the solar heating makes it possible to compare the respective temperature patterns. The similarity between the modelled and measured fields is quite obvious, although the modelled temperature field has less structure. The model was able to distinguish differences in surface heating between the different land-use types even with only five land-use

[1] Comes from NOAA-7, -8 and -9 which carry an Advanced Very High Resolution Radiometer (AVHRR). The ground resolution is 1.1 km and the swath width is 2700 km.

[2] Local Standard Time in Vancouver is about 10 minutes ahead of Pacific Standard Time in summer

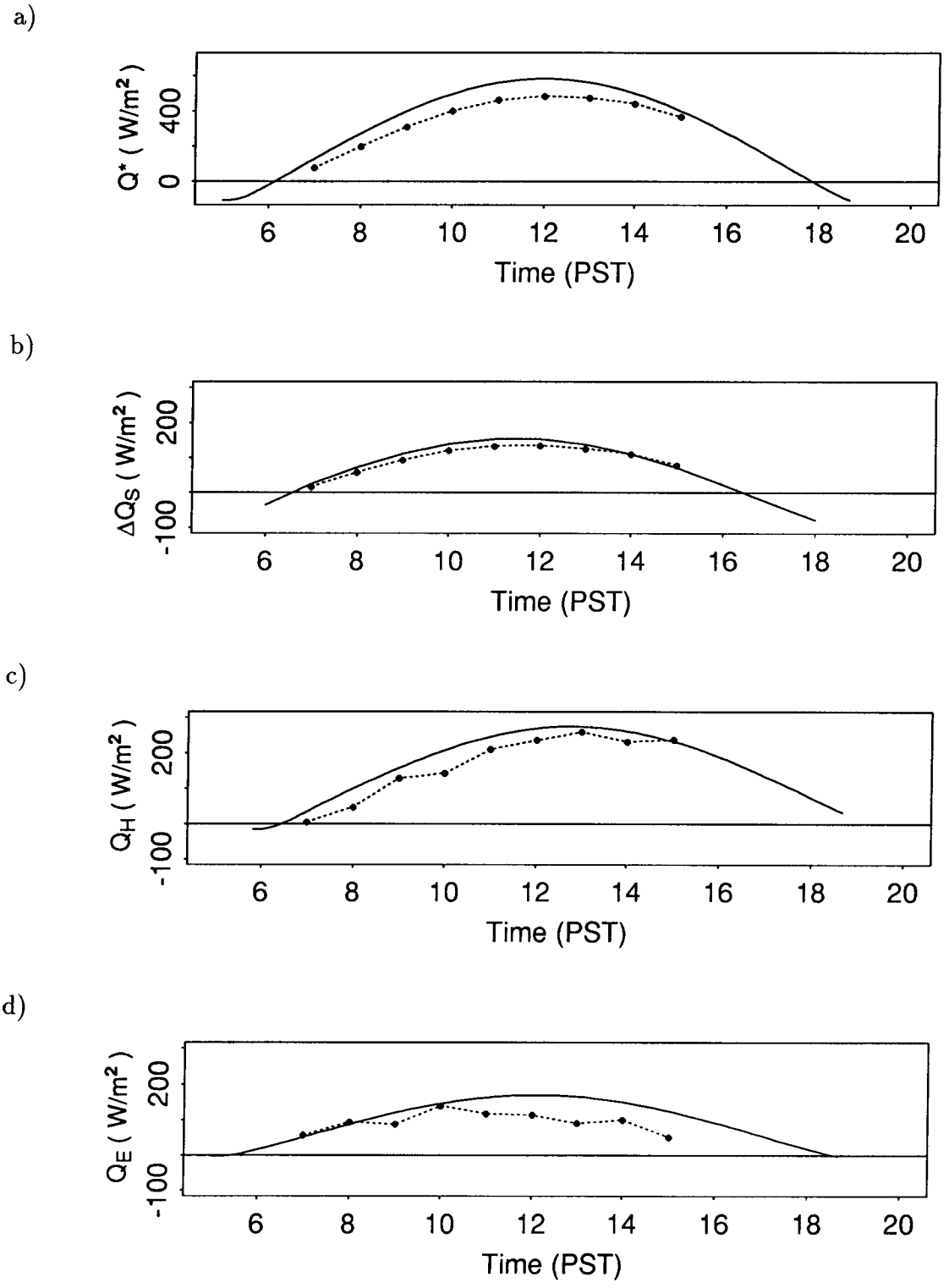

Figure A.2: Time series for surface fluxes at the Sunset suburban site in Vancouver. a) Net radiation, b) Storage heat flux, c) Sensible heat flux, d) Latent heat flux. Solid line - modelled values. Dashed - observed.

classes specified. It can be concluded from the above two comparisons that this surface energy balance scheme is able to simulate the general time-varying patterns of the four heat fluxes, and is able to predict reasonable surface temperature field. Yet the scheme leaves room for improvement in its overestimation of net radiation.

a)

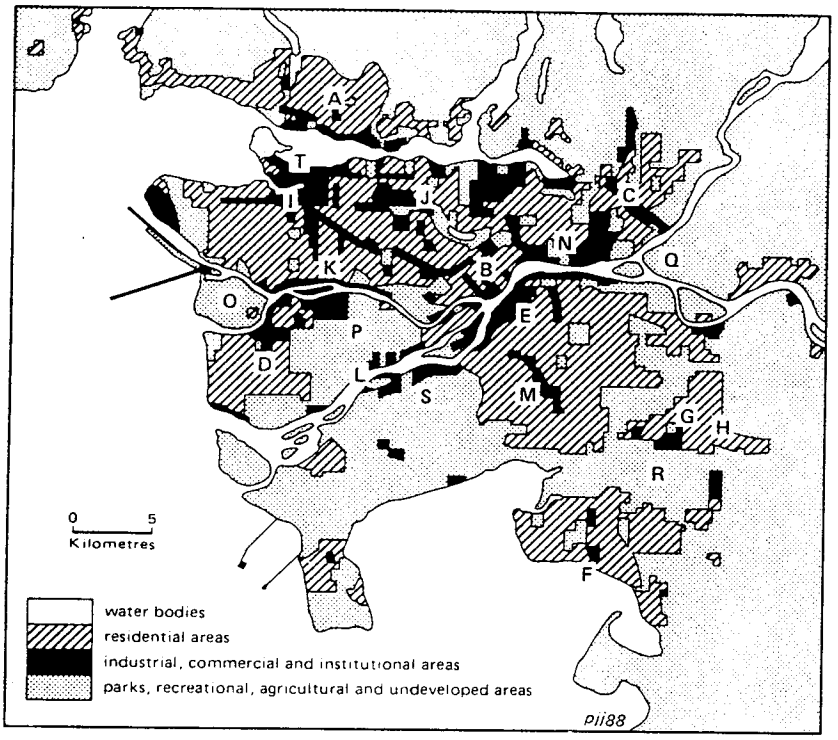

b)

Figure A.3: a) Location and land-use maps of Vancouver. b) The surface radiant temperature distribution for the same area at 13.56 (LST) on 16 August 1985. The rainbow brightness temperatures in b) are in degree Celsius. From Roth et al. (1989), p1705-1707.

a)

b)

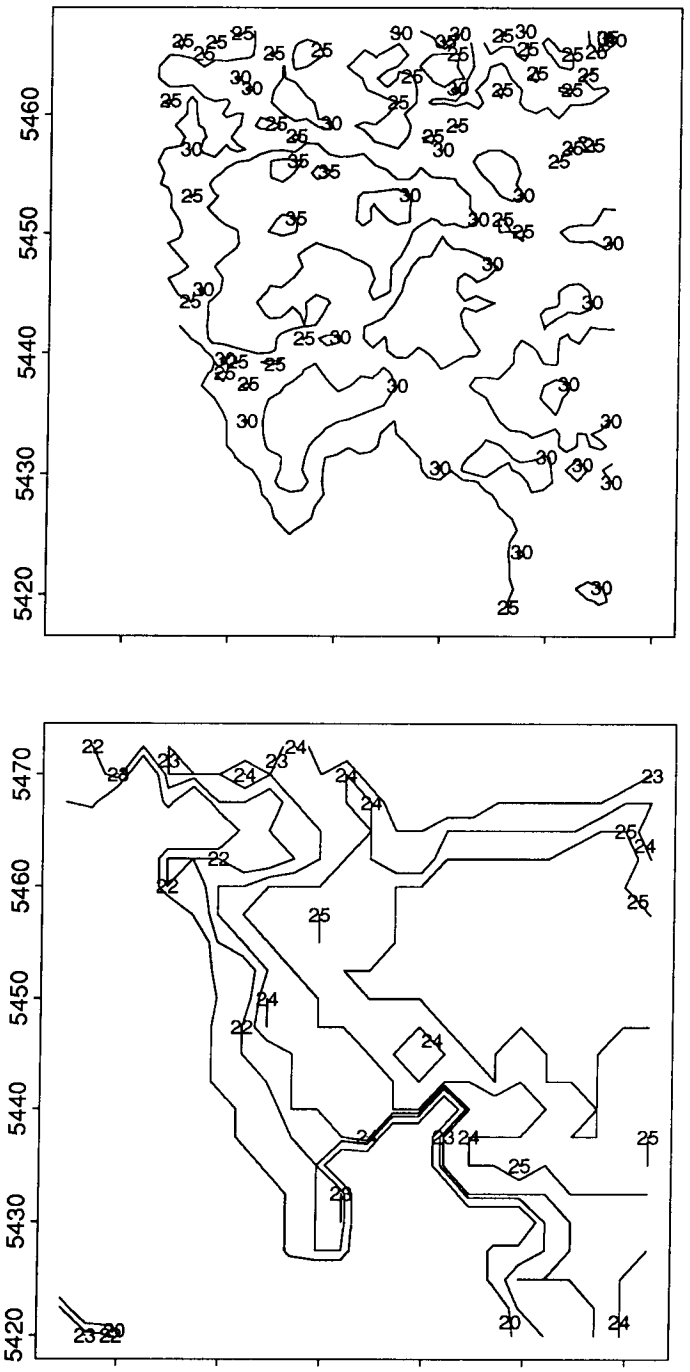

Figure A.4: a) Contour plot of surface temperatures derived from the satellite thermal image in Fig. A.3b, and b) contour plot of surface temperatures derived from the RAMS model output at 1400 PST on August 23, 1985. All plots cover the same area as depicted in Fig. A.3a. Temperatures are in degree Celsius.

Bibliography

Atkinson, B. W., 1981. *Meso-scale Atmospheric Circulations*, Academic Press, Toronto, p. 495.

Atwater, M. A. and P. S. Brown, 1974: Numerical Calculation of the Latitudinal Variation of Solar Radiation for an Atmosphere of Varying Opacity , *Journal of Applied Meteorology*, **13**, 289–297.

Blackadar, A. K., 1976: Modeling the Nocturnal Boundary Layer, Symp. Atmos. Turbul. Diffus. Air Qual. Prepr. 3rd.

de Bruin, H. A. R., 1983: A Model for the Priestley-Taylor Parameter α , *Journal of Climate and Applied Meteorology*, **22**, 572–578.

de Bruin, H. A. R. and A. A. M. Holtslag, 1982: A Simple Parameterization of the Surface Fluxes of Sensible and Latent Heat During Daytime Compared with the Penman-Monteith Concept, *Journal of Applied Meteorology*, **21**, 1610–1621.

de Bruin, H. A. R. and J. Q. Keijamn, 1979: The Priestley-Taylor Evaporation Model Applied to a Large Shallow Lake in the Netherlands, *Journal of Applied Meteorology*, **18**, 898–903.

Brunt, D., 1941. *Physical and Dynamical Meteorology*, Cambridge University Press, London, p. 428.

Businger, J. A., J. C. Wyngaard, Y. Izumi and E. F. Bradley, 1971: Flux Profile Relationships in the Atmospheric Surface Layer, *Journal of Atmospheric Science*, **28**, 181–189.

Camuffo, D. and A. Bernardi, 1982: An observational Study of Heat Fluxes and the Relationship with Net Radiation, *Boundary Layer Meteorology*, **23**, 359–368.

Chang, Y. S., G. R. Carmichael, H. Kurita, T. Kitada and H. Ueda, 1990: Diagnostic Evaluation of the Transport and Gas Chemistry Components of the STEM-II model, *Atmospheric Environment*, **24A**(11), 2715–2737.

Chang, Y. S., G. R. Carmichael, H. Kurita and H. Ueda, 1989: The Transport and Formation of Photochemical Oxidants in Central Japan, *Atmospheric Environment*, **23**(2), 363–393.

Chang, Y. S., W-C. Shin, G. R. Carmichael, H. Kurita and H. Ueda, 1990: Evaluation of the Effect of Emission Reductions on Pollutant Levels in Central Japan, *Environmental Science Technology*, **24**, 1355–1366.

Charney, J. G., R. Fjortoft and J. von Neumann, 1950: Numerical Integration of the Barotropic Vorticity Equation, *Tellus*, **2**, 237–254.

Clarke, R. H., A. J. Dyer, P. R. Brook, D. G. Reid and A. J. Troup, 1971: The Wangara Experiment-Boundary Layer Data, Division of Meteorological Physics, C.S.I.R.O., Australia.

Cleugh, H. A., 1990: *Development and Evaluation of Suburban Evaporation Model: a Study of Surface and Atmospheric Controls on the Suburban Evaporation regime*, The University of British Columbia, Vancouver, Canada, Ph.D. Thesis.

Concord Scientific Corporation(CSC), 1982: *Vancouver Oxidant Study, Air Quality Analyis 1978-1981*, Prepared for Environment Canada, Environmental Protection Service.

———, 1985: *Vancouver Oxidant Study, Air Quality Analyis Update 1982-1984*, Prepared for Environment Canada, Environmental Protection Service.

Deardorff, J. W., 1978: Efficient Prediction of Ground Surface Temperature and Moisture, with Inclusion of a Layer of Vegetation, *Journal of Geophysical Research*, **83(c4)**, 1889–1903.

Doll, D., J. K. S. Ching and J. Kaneshiro, 1985: Parameterisation of Subsurface Heating for Soil and Concrete Using Net Radiation Data , *Boundary Layer Meteorology*, **32**, 351–372.

Gal-Chen, T. and R. C. J. Somerville, 1975: On the Use of a Coordinate Transformation for the Solution of the Navier-Stokes Equations, *J. Comp. Phys.*, **17**, 241–249.

Grimmond, C. S. B., 1992: Personal Communication.

Grimmond, C. S. B., H. A. Cleugh and T. R. Oke, 1991: An Objective Urban Heat Storage Model and Its Comparison with Other Schemes, *Atmospheric Environment*, **25B(3)**, 311–326.

Güsten, H., 1986: Formation, Transport and Control of Photochemical Smog. *Air Pollution*, O. Hutzinger, Ed., The Handbook of Environmental Chemistry, **Volume 4 Part A**, pp. 53–106.

Hay, J. E. and T. R. Oke, 1976. *The Climate of Vancouver*, Tantalus Research Limited, Vancouver, p. 48.

Jackson, P., 1993: *Gap Winds in a Fjord: Howe Sound, British Columbia*, The University of British Columbia, Vancouver, Canada, Ph.D. Thesis.

Jacobs, C. A. and P. S. Brown, 1974: *IFYCL Final Report, Vol. IV Three-dimensional Results*, The Center for the Environment and Man, CEM Rep. No. 4131-509d, Hartford, Connecticut.

Klemp, J. B. and D. K. Lilly, 1978: Numerical Simulation of Hydrostatic Mountain Waves, *Journal of the Atmospheric Sciences*, **35**, 78–107.

Klemp, J. B. and R. B. Wilhelmson, 1978: The Simulation of Three-Dimensional Convective Storm Dynamics, *Journal of the Atmospheric Sciences*, **35**, 1070–1096.

Kondratyev, K. Y., 1969: *Radiation in the Atmosphere*, Academic Press, New York.

Kuhn, P., 1963: Radiometeorsonde Observations of Infrared Flux Emissivity of Water Vapour, *Journal of Applied Meteorology*, **2**, 368–378.

Kurita, H., K. Sasaki, H. Muroga, H. Ueda and S. Wakamatsu, 1985: Long-Range Transport of Air Pollution under Light Gradient Wind Conditions, *Journal of Climate and Applied Meteorology*, **24**, 425–434.

Lalas, D. P., D. N. Asimakopoulos, D. G. Deligiorgi and C. G. Helmis, 1983: Sea Breeze Circulation and Photochemical Pollution in Athens, Greece, *Atmospheric Environment*, **17**, 1621–1632.

Lee, X., 1992: Personal Communication.

Lewis, J. E. and T. N. Carlson, 1989: Spatial Variations in Regional Surface Energy Exchange Patterns for Montreal, Quebec, *The Canadian Geographer*, **33, No. 3**, 194–203.

Louis, J-F., 1979: A Parametric Model of Vertical Eddy Fluxes in the Atmosphere, *Boundary Layer Meteorology*, **17**, 187–202.

Lyons, W. A., 1975: Turbulent Diffusion and Pollutant Transport in Shoreline Environments. *Lectures on Air Pollution and Environmental Impact Analysis*, pp. 136–208.

Mahrer, Y. and R. A. Pielke, 1977a: The Effects of Topography on the Sea and Land Breezes in a Two-Dimensional Numerical Model, *Monthly Weather Review*, **105**, 1151–1162.

———, 1977b: A Numerical Study of the Airflow over Irregular Terrain, *Beiträge zur Physik der Atmosphäre*, **50**, 98–113.

McCaughey, J. H., 1985: Energy Balance Storage Terms in a Mature Mixed Forest at Petawawa, Ontario - A Case Study, *Boundary Layer Meteorology*, **31**, 89–101.

McCumber, M. C., 1980: *A Numerical Simulation of the Influence of Heat and Moisture Fluxes upon Mesoscale Circulations*, University of Virginia, Charlottesville, USA, Ph.D. Thesis.

McDonald, J., 1960: Direct Absorption of Solar Radiation by Atmospheric Water Vapour, *J. Meteorol.*, **17**, 319–328.

McKendry, I. G. and M. Li-Ting-Wai, 1993: *A Synoptic Climatology of Ozone Concentrations at Port Moody, Lower Fraser Valley, B.C.*, Report prepared for Air Resources Branch, British Columbia Ministry of Environment, Lands and Parks, 37 pp..

McNaughton, K. G. and T. W. Spriggs, August, 1987: An Evaluation of the Priestley and Taylor Equation and the Complementary Relationship Using Results from a Mixed-Layer Model of the Convective Boundary Layer, IAHS Publication No. 177 Estimation of Areal Evapotranspiration , Vancouver, B. C., Canada.

McNider, R. T. and R. A. Pielke, 1981: Diurnal Boundary-Layer Development over Sloping Terrain, *Journal of the Atmospheric Sciences*, **38**, 2198–2212.

Monin, A. S. and A. M. Obukhov, 1954: Basic Regularity in Turbulent Mixing in the Surface Layer of the Atmosphere, *Akad. Nauk. S.S.S.R. Trud. Geofiz. Inst., Tr.*, **24**.

Monteith, J. L., 1981: Evaporation and Surface Temperature, *Quarterly Journal Royal Meteorological Society*, **107** , 1–27.

Moore, G. E., S. G. Douglas, R. C. Kessler and J. P. Killus, 1991: Identification and Tracking of Polluted Air Masses in the South-Central Coast Air Basin, *Journal of Applied Meteorology*, **30**, 715–732.

Moran, M., 1992: *Mesoscale Dispersion Modelling*, The Colorado State University, Boulder, U. S. A., Ph.D. Thesis.

Moussiopoulos, N., 1989. *Mathematische Modellierung mesoskaliger Ausbreitung in der Atmosphare*, VDI-Verlag,Dusseldorf, p. 307.

———, 1993. *The Athens Experience*, Monterrey, Mexico, Air Pollution '93 Conference, p. 128.

Moussiopoulos, N., T. Flassak, P. Prahm and D. Berlkowitz, 1993: Simulations of the Wind Field in Athens with the Nonhydrostatic Mesoscale Model MEMO, Environmental Software(submitted).

Moussiopoulos, N. and W. Oehler, 1988: Numerical Simulations of the Photochemical Air Pollution Levels in Athens, Greece, *Environmental Software*, **3**, 105–109.

Narita, K., T. Sekine and T. Tokuoka, 1984: Thermal Properties of Urban Surface Materials-Study on Heat Balance at Asphalt Pavement, *Geog. Rev. Japan*, **57A**, 639–651.

Novak, M. D., 1981: *The Moisture and Thermal Regimes of a Bare Soil in the Lower Fraser Valley during Spring*, The University of British Columbia, Vancouver, Canada, Ph.D. Thesis.

Nunez, M., 1974: *The Energy Balance of an Urban Canyon*, The University of British Columbia, Vancouver, Canada, Ph.D. Thesis.

Oke, T. R., 1981: Canyon Geometry and the Nocturnal Urban Heat Island: Comparison of Scale Model and Field Observations, *Journal of Climatology*, **1**, 237–254.

———, 1989: The Urban Energy Balance, *Progress in Physical Geography*, **12**, 471–508.

Oke, T. R. and H. A. Cleugh, 1987: Urban Heat Storage Derived as Energy Budget Residuals, *Boundary Layer Meteorology*, **39**(3), 233–245.

Oke, T. R. and G. B. Maxwell, 1975: Urban Heat Island Dynamics in Montreal and Vancouver, *Atmospheric Environment*, **9**, 191–200.

Oliger, J. and A. Sundstrom, 1978: Theoretical and Practical Aspects of Some Initial Boundary Value Problems in Fluid Dynamics, *SIAM J. Appl. Math.*, **35**, 419–446.

Orlanski, I., 1976: A Simple Boundary Condition for Unbounded Hyperbolic Flows, *J. Comput. Phys.*, **21**, 251–269.

Persson, C., H. Rodhe and L. -E. D. Geer, 1987: The Chernobyl Accident - a Meteorological Analysis of how Radionuclides Reached and Were Deposited in Sweden, *Ambio*, **16**, 20–31.

Pielke, R. A., 1974a: A Comparison of Three-Dimensional and Two-Dimensional Numerical Predictions of Sea Breezes, *Journal of the Atmospheric Sciences*, **31**, 1577–1585.

———, 1974b: A Three-Dimensional Numerical Model of the Sea Breeze over South Florida, *Monthly Weather Review*, **102**, 115–139.

———, 1984: *Mesoscale Meteorological Modeling*, Academic Press.

Pielke, R. A., W. R. Cotton, R. L. Walko, C. J. Tremback, W. A. Lyons, L. D. Grasso, M. E. Nicholls, M. D. Moran, D. A. Wesley, T. J. Lee and J. H. Copeland, 1992: A Comprehensive Meteorological Modeling System - RAMS, *Meteorol. Atmos. Phys.*, **49**, 69–91.

Platzman, G. W., 1954: The Computational Stability of Boundary Conditions in Numerical Integration of the Vorticity Equation, *Arch. Met. Geophys. Biokl.*, **A7**, 29–40.

———, 1979: The ENIAC Computations of 1950 - Gateway to Numerical Weather Prediction, *Bull. Amer. Meteor. Soc.*, **60**, 302–312.

Priestley, C. H. B. and R. J. Taylor, 1972: On the Assessment of Surface Heat Flux and Evaporation, *Monthly Weather Review*, **106**, 81–92.

Robeson, S. M. and D. G. Steyn, 1990: Evaluation and Comparison of Statistical Forcast Models for Daily Maximum Ozone Concentrations, *Atmospheric Environment*, **24B**(2), 303–312.

Roth, M., 1991: *Turbulent Transfer Characteristics over a Suburban Surface*, The University of British Columbia, Vancouver, Canada, Ph.D. Thesis.

Roth, M. and T. Oke, 1993: Comparison of Modelled and "Measured" Heat Storage in Suburban Terrain, Atmospheric Environment(in press).

Roth, M., T. Oke and W. J. Emery, 1989: Satellite-Derived Urban Heat Islands from Three Coastal Cities and the Utilization of such Data in Urban Climatology, *Int. J. Remote Sensing*, **Vol. 10, NO. 11**, 1699–1720.

Smith, F. B. and M. J. Clark, 1988: Wet and Dry Deposition of Chernobyl Releases, *Nature*, **322**, 245–249.

Stern, A. C., R. W. Boubel, D. B. Turner and D. L. Fox, 1984: *Fundamentals of Air Pollution*, Academic Press.

Steyn, D. G., 1980: *Turbulence, Diffusion and the Daytime Mixed Layer Depth over a Coastal City*, The University of British Columbia, Vancouver, Canada, Ph.D. Thesis.

Steyn, D. G., M. Bovis, M. North and O. Slaymaker, 1992: The Biophysical Environment Today. *Vancouver and Its Region*, G. Wynn and T. R. Oke, Eds., UBC Press, University of British Columbia, Vancouver, BC, Canada.

Steyn, D. G. and D. A. Faulkner, 1986: The Climatology of Sea-Breezes in the Lower Fraser Valley, B.C., *Climatological Bulletin*, **20(3)**, 21–39.

Steyn, D. G. and I. G. McKendry, 1987: Sea Breeze Dynamics in the Lower Fraser Valley, B. C., Geography Department Report of UBC.

———, 1988: Quantitative and Qualitative Evaluation of a Three-Dimens ional Mesoscale Numerical Model Simulation of a Sea Breeze in Complex Terrain, *Monthly Weather Review*, **116**, 1914–1926.

Steyn, D. G. and T. R. Oke, 1982: The Depth of the Daytime Mixed Layer at Two Coastal Sites: A Model and Its Validation, *Boundary-Layer Meteorology*, **24**, 161–180.

Steyn, D. G., A. C. Roberge and C. Jackson, 1990: *The Anatomy of an Extended Air Pollution Episode in British Columbia's Lower Fraser Valley*, Report prepared for Waste Management Branch, British Columbia Ministry of Environment, 55pp. pp..

Stull, R. B., 1989: *An Introduction to Boundary Layer Meteorology*, Atmospheric Sciences Library, Kluwer Academic Publishers, Dordrecht, Holland.

Taesler, R., 1980: Studies of the Development and Thermal Structure of the Urban Boundary Layer in Uppsala, Part I: Experimental Program; and Part II: Data, Analysis and Results, Report 61, Met. Instit., Uppsala University, Uppsala.

Taylor, E., 1991: *Forcasting Ground-Level Ozone in Vancouver and the Lower Fraser Valley of British Columbia*, Scientific Services Division, Atmospheric Environment Service, Pacific Region, Environment Canada, Report PAES-91-3, 8pp pp..

Tremback, C., G. Tripoli, R. Arritt, W. R. Cotton and R. A. Pielke, Nov., 1986: The Regional Atmospheric Modeling System, Proceeding of International Conference on Development and Application of Computer Techniques to Environmental Studies (ENVIROSOFT 86), Los Angeles, U.S.A..

Tremback, C. J. and R. Kessler, June 17-20, 1985: A Surface Temperature and Moisture Parameterization for use in Mesoscale Numerical Models, 7th Conference on Numerical Weather Prediction, AMS, Montreal, Quebec, Canada.

Tripoli, G. J. and W. R. Cotton, 1982: The Colorado State University Three-Dimensional Cloud/Mesoscale Model 1982. Part I: General Theoretical Framework and Sensitivity Experiments , *J. de Rech. Atmos.*, **16**, 185–220.

Ulrickson, B. L. and C. F. Mass, 1990a: Numerical Investigation of Mesoscale Circulations over the Los Angeles Basin. Part II: Synoptic Influence and Pollutant Transport, *Monthly Weather Review*, **118**, 2162–2184.

———, 1990b: Numerical Investigation of Mesoscale Circulations over the Los Angles Basin. Part I: A Verification Study, *Monthly Weather Review*, **118**, 2138–2161.

Walko, R. L. and C. J. Tremback, 1991: The RAMS Model Users's Guide (draft), ASTeR, Inc. Fort Collins.

Wheeler, D. A., 1988: Atmospheric Dispersal and Deposition of Radioactive Material from Chernobyl, *Atmospheric Environment*, **22**, 853–863.

Wieringa, J., July 1991: Updating the Davenport Roughness Classification, 8th International Conf. on Wind Engineering, London, Ontario, Canada.

Willmott, C. J., 1981: On the Validation of Models, *Physical Geography*, **2(2)**, 168–194.

———, 1982: Some Comments on the Evaluation of Model Performance, *Bulletin of American Meteorological Society*, **63(11)**, 1309–1313.

———, 1985: Statistics for the Evaluation and Comparison of Models, *Journal of Geophysical Research*, **90(c5)**, 8995–9005.